ELECTROCHEMICAL GROWTH OF THREE-DIMENSIONALLY ORDERED MACROPOROUS METALS AS PHOTONIC CRYSTALS

by

Rong Zhu

CID No.: 00447592

IMPRIAL COLLEGE LONDON
DEPARTMENT OF MATERIALS

Thesis submitted in fulfilment of the requirement for the degree of Doctor of Philosophy (Ph.D).

AUTHOR'S DECLARATION

I herewith declare that I am the sole author of this thesis. The work was carried out in the Department of Materials, Imperial College London on my own with the exception of the following. The focused ion beam image presented in Figure 5-10(b) was conducted by Dr. Steve Reyntjens (FEI company, Netherlands). The measurement of surface-enhanced Raman spectroscopy in Chapter 5 was conducted by Dr. Robert Maher (Department of Physics, Imperial College London).

The results contained within the thesis have not previously been submitted for a higher degree. However some results have been presented in the following publications:

1. Rong Zhu et al., Electrochemically grown metallic inverse opals, *ECS transactions*, 2008, Vol.13, Issue 18, 1-6.
2. Rong Zhu et al., Controlling electrodeposition of mesoporous metals for nanoplasmonics, *Nanoscale*, 2009, Vol.1, Issue 3, 355-359. (cover article)

Author's name Signature

RONG ZHU

_____ _____

ABSTRACT

Over the last two decades three dimensionally ordered macroporous (3-DOM) materials have turned out to be very promising in many applications ranging from optics, plasmonics, to catalyst scaffolds. The thesis presents a systematic study on formation and characterisation of 3-DOM metals as photonic crystals. Metals are nearly perfect reflectors with low adsorption at microwave or millimetre wavelengths. Meanwhile they generally absorb visible light because of their negative imaginary part of the dielectric constant that could destroy the band gap in the visible though they. Howevers, for noble metals such as gold, silver and copper, considering the Drude-like behaviour, the adsorption will be small enough to achieve a complete photonic band gap for optical or even shorter wavelengths, with silver performing the best.

In order to fabricate the 3-DOM metallic nanostructures, template-directed electrochemical deposition has been employed in which, initially a highly ordered film of submircon sized colloidal spheres is deposited on to electronically conducting substrates, for instance, indium-tin oxide (ITO) coated glass substrate, through evaporation-induced self-assembly; and subsequently it is infiltrated with metallic elements electrochemically reduced from corresponding electrolytes; fiannly removal of the colloidal templating film reveals a metallic film comprised of periodically arranged spherical voids. Field Emission Gun Scanning Electron Microscopy (FEGSEM) was used to examine the surface morphology and periodicity of the 3-DOM metallic films. It revealed that highly ordered structures are homogenous and uniform over a large scale for both the original colloidal templates and

metallic inverse structures. However for silver electroplated from either silver thiosulfate or silver chlorate bath, voids in the template are fully infiltrated, including both the interstitial spaces between the colloidal spheres and any cracks between film domains, forming a complete solid network over large length scales; for copper the filling factors are strongly dependent on the bath chemistry and in copper sulfate bath isolated macroporous domains can be formed due to those in the cracks will be dissolved back to the solution while those reduced from copper glycerol bath resulted in fully infiltrated structures. Moreover, angle-resolved reflectance spectroscopy has further confirmed the three-dimensional periodicity and indicated the inverse structures have stop band properties in the visible wavelength region, consistent with variation in the effective refractive index of the films.

In addition, surface enhanced Raman scattering (SERS) spectroscopy has been used to evaluate applications of the inverse metals as SERS-active substrates. SERS has nearly exclusively been associated with three noble metals copper, silver (by far the most important) and gold. The 3-DOM metallic thin films possess excellent features for SERS detection arising from their long range periodical void geometry, which gives significant enhancement to Raman intensity. Preliminary measurements have demonstrated the 3-DOM metallic structures are well suited for SERS enhancement. Series spectra from different points of each specimen have given reproducible intensities. Variables associated with Raman intensity such as pore size, dye concentration, and film thickness, have been tuned to achieve maximal enhancement for visible and near-IR wavelengths.

ACKNOWLEDGEMENTS

First of all I would like to express my deep appreciation to my two supervisors Dr. Mary Ryan and Prof. David McComb. Their extensive knowledge and expertise in nanotechnology and electrochemistry has provided me invaluable advice and insights to advance my research. I was given a learning environment to grow me personally as well as professionally. All I have learned from them, from the work attitude, planning work, technical writing to interpersonal relationship skills, will be treasures that benefiting my future career. Meanwhile I cannot forget to say thanks to all members, past and present, from Mary's and David's group, especially Martyn McLachlan, Niall Thomason, Catherine Barron, Imran Khan, Virginie Jantou, Chien-Lung (Jack) Teng, Ying An, Benoit Illy, Shima Kadkahodazadeh, Carrina Turner, and Sarah Berhanu, for their constant help and support through the last four years. In recognition of the help over all instruments, I would also like to take this opportunity to thank Mahmoud Ardakani, Richard Chater, Richard Sweeney, and Robert Maher.

I wish to acknowledge the financial support from Hutchison-EPSRC Dorothy Hodgkin Postgraduate scholarship which enabled me to undertake the research on a full-time basis. Special thanks go to departmental postgraduate secretary Miss Norma Hikel for her patient and warm help on every aspects of life in the last four years. Finally I would like to thank Maurizio Tarzia, Ai Leen Koh, Chin (Sunny) Phuah, Eva McGuire, and Robert Maher for their time on proof read, without whom the completion of the thesis would have been very much more difficult.

TABLE OF CONTENTS

Author's declaration ..... **i**

Abstract ..... **ii**

Acknowledgements ..... **iv**

Table of Contents ..... **v**

List of Figures ..... **vii**

List of Tables ..... **xii**

1 INTRODUCTION **1**

1.1 Introduction to 3-DOM materials 1
1.2 Research motivation 3
1.3 Thesis outline 5

2 LITERATURE REVIEW **8**

2.1 Photonic band gap 8
2.1.1 Origins of photonic band gap 8
2.1.2 Photonic band gap in 3-DOM materials 11
2.2 Surface enhanced Raman scattering 14
2.2.1 Brief history of SERS 14
2.2.2 Enhancement theory 17
2.2.3 3-DOM metals as SERS substrates 19
2.3 Fabrication strategies of colloidal crystal templating 20
2.3.1 Self-assembly techniques of colloidal crystals 21
2.3.2 Infiltration techniques 27

3 INSTRUMENTATION **38**

3.1 Optical microscope 38
3.2 Scanning electron microscope 39
3.2.1 Basic principles of SEM 40
3.2.2 Image mechanisms of SEM 41
3.3 Reflectance spectroscopy 46
3.3.1 Instrumental setup 46
3.3.2 Spectral analysis 47
3.4 Surface enhanced Raman spectroscopy 50
3.5 X-ray Diffraction 52

4 SYNTHESIS OF COLLOIDAL TEMPLATES **54**

4.1 Synthesis of colloidal spheres 54
4.2 Experimental 57

4.2.1 Materials 57
4.2.2 Procedure 58
4.3 Results and discussions 59
4.3.1 Crystalline control 59
4.3.2 Microstructural analysis 68
4.4 Chapter summary 75

5 3-DOM METALS VIS TEMPLATE-DIRECTED ELECTROCHEMICAL PLATING 77

5.1 Introduction 77
5.2 Preliminary work 79
5.3 Experiment 81
5.3.1 Bath solution 81
5.3.2 Parameters 82
5.4 Results and discussions 84
5.4.1 Structural characterisation 85
5.4.2 Isolated macroporous domains 92
5.4.3 Chemical composition 98
5.5 Electrochemical plating 101
5.5.1 Electrochemical response 101
5.5.2 Faraday's law 103
5.5.3 Current density 104
5.5.4 Plating time 106
5.6 Optical properties 108
5.6.1 Metal dependence 109
5.6.2 Film thickness dependence 111
5.6.3 Void size dependence 112
5.7 Preliminary SERS measurements 114
5.7.1 Dye dependence 114
5.7.2 Metal dependence 117
5.7.3 Void size dependence 118
5.7.4 Dye concentration dependence 119
5.7.5 Film thickness dependence 121
5.8 Chapter summary 123

6 CONCLUSIONS AND FUTURE WORK 125

6.1 Thesis conclusion 125
6.1.1 Templating film growth 125
6.1.2 3-DOM metal growth 126
6.1.3 Surface morphology 127
6.1.4 Optical properties 128
6.1.5 SERS measurements 129
6.2 Suggestions for future work 129

7 REFERENCES 132

LIST OF FIGURES

Figure 1-1 Photonic crystal structure with three-dimensional periodicity (a) layer by layer of one-dimensional rods with a stacking sequence that repeat itself every four layers [12]; (b) a waveguide carved by introducing linear defect in crystalline array [17]. 2

Figure 1-2 Structural features of 3-DOM materials (a) top surface SEM image of polymer crystalline array and (b) corresponding inverse 3-DOM copper, consisted of highly ordered pores in solid copper matrix (present work). 3

Figure 1-3 Spectral reflectance of silver, gold and copper as a function of the radiation energy at normal incidence [62]. 4

Figure 2-1 Bragg reflection occurs when resonant wavelength matches lattice spacing and incident angle. 9

Figure 2-2 Bragg scattering in crystals (a) each set of planes acts as a mirror in a small range of angle; (b) each set of planes acts as a mirror in a large range of angles which overlap completely. 9

Figure 2-3 Real space schematic representation of (a) one-dimensional; (b) two-dimensional; (c) three-dimensional photonic crystals. 11

Figure 2-4 Real and reciprocal space representation of two-dimensional (a) square lattice and (b) hexagonal lattice [3,98]. The left images are real lattices, the middle ones are corresponding reciprocal lattices, and the right ones are construction of first Brillouin zone (yellow regions). 12

Figure 2-5 Bravais lattices and their corresponding first Brillouin zones (a) simple cubic; (b) face-centred cubic [104]. 13

Figure 2-6 A lattice may present different topographies here take f.c.c for example. (a) isolated dielectric spheres in air and corresponding inverse structure - isolated air spheres in a dielectric solid; (b) interpenetrated dielectric spheres in air and corresponding inverse structure - interpenetrated air spheres in a dielectric solid. 14

Figure 2-7 Diagram of Rayleigh and Raman scattering. The letter *m* represents ground vibration state and *n* is for a higher excitation state. 16

Figure 2-8 Schematic process for colloidal crystal templating. 20

Figure 2-9 Experimental setup of electrophoretic cell [175]. 23

Figure 2-10 Illustration of producing 2D colloidal crystal by spin-coating [182]. 24

Figure 2-11 Sketch of particles and water fluxes in the vicinity during convective self-assembly [92]. 25

Figure 2-12 Schemes of (a) surface-templated infiltration, which will leave voids (marked by arrows) in the middle of each intersections; (b) volume-templated infiltration resulted a complete filled structure. 29

Figure 2-13 SEM images of three-dimensional gold film shown in early work (a) made with a silica template, reveals porous structure with gold flakes between domain boundaries; (b) made with a polystyrene template, demonstrates gold was grown in form of flakes and ordered porous structure within each flake [71].....29
Figure 2-14 SEM images of 3-DOM gold film made with polystyrene templates (a) surface view, reveals ordered spherical voids (b) side view, presents flat smooth surface [70].....30
Figure 2-15 SEM images of 3-DOM nickel films made with polystyrene templates and corresponding current - time curves. (a) 7 layers; (b) 4 layers [198].....31
Figure 2-16 SEM images of 3-DOM thin film made from electrochemical plating. (a) cuprous nickel film [198], showing the porous domains are connected by dense solids; (b) zinc film, showing isolated porous domains [201].....32
Figure 2-17 Schematic process of precipitation/chemical convection [206].....34
Figure 2-18 Schematic process of nanoparticle infiltration.....35
Figure 3-1 Optical microscope images of polystyrene films with increasing film thickness from (a) to (d).....39
Figure 3-2 Schematic diagram of a scanning electron microscope. 41
Figure 3-3 Generalized illustration of interaction volumes. 42
Figure 3-4 Schematic diagram of secondary electron generation.....43
Figure 3-5 SEM surface view of a polystyrene film obtained in present work. 44
Figure 3-6 Classical models showing the production of (a) characteristic X-rays and Auger electrons 46
Figure 3-7 Schematic setup for measuring angle-resolved reflectivity, adapted from BENTHAM 200 series user handbook. 47
Figure 3-8 Angle-resolved reflectance spectra of polystyrene film.....48
Figure 3-9 Linear fit to determine the thickness of the film from Fabry-Perot fringes obtained at 10 °incident angle (inset), in which numbers 1 to 7 are the orders of the fringes. 50
Figure 3-10 Schematic layout of Renishaw 2000 CCD Raman spectrometer with Olympus BH-2 confocal microscope, adapted from the Ranishaw manual. 51
Figure 3-11 Schematic construction of X-ray diffractometer. A. X-ray source; B. focusing slit; C. specimen stage; D. receiving slits; E. monochrometer or filter; and F. X-ray detector.....52
Figure 4-1 Emulsion polymerisation process of styrene using potassium persulfate as initiator to produce polystyrene. 56
Figure 4-2 TEM images of colloidal spheres of mean diameter of 327 ± 6.0 nm. 57
Figure 4-3 Schematic process of growing polystyrene colloidal crystals through evaporation induced self-assembly. 59
Figure 4-4 Optical microscopy images of polystyrene film (a) layered up top area; (b) uniform middle area of high magnification ×50; (c) middle area remain uniform in low magnification ×10; (d) less uniform bottom area.....60

Figure 4-5 (a) high surface tension resulted in 'stripes' on the glass substrate; (c) hydrophilic surface produced continues dense packed colloidal film; (b) and (d) optical microscopy images of corresponding enlarged areas. 61
Figure 4-6 Digital photography images of polystyrene films on ITO glass substrates (a) proper cleaned surface gives uniform growth; (b) - (d) surface suffering contamination and result in delaminated or non-uniform films. Film growth directions are from top to the bottom, as indicated by arrows. 62
Figure 4-7 SEM images of the polystyrene films grown from colloids of comparable sizes but with polydispersities of (a) & (b) 9.4% and (c) & (d) 3.6%. 63
Figure 4-8 SEM surface images of colloidal crystals (sphere diameter of 327 ± 6.0 nm) prepared at evaporation temperatures of (a) 50 ℃, (b) 60 ℃, and (c) 70 ℃. Growth directions are represented by arrows.....64
Figure 4-9 Cracks in the polystyrene films grown at 60 ℃ but with relative humidity of (a) 10% and (b) 30%.....65
Figure 4-10 SEM images of polystyrene films prepared with increasing volume fraction (sphere diameter of 651 ± 23.4 nm) (a) 0.01 vol.%, (b) 0.05 vol.%, (c) 0.10 vol.%, (d) 0.30 vol.%, (e) 0.50 vol.% and (f) 1.00 vol.%.....66
Figure 4-11 Crack pattern of polystyrene films with decreasing volume fraction (sphere diameter D = 327 ± 6.0 nm) (a) 0.01 vol.%, (b) 0.05 vol.%, (c) 0.10 vol.%, (d) 0.30 vol.%, (e) 0.50 vol.% and (f) 1.00 vol.%. 67
Figure 4-12 SEM images of the polystyrene films grown from 327 nm colloidal spheres (a) surface view (the inset is an FFT over a 40×40 μm^2 area) ; (b) a cleaved edge 69
Figure 4-13 Normalised angle resolved reflectance spectra of the polystyrene film (Mean sphere diameter D = 327 ± 6.0 nm) 70
Figure 4-14 Linear fits for the reflection peaks in Figure 4-13 71
Figure 4-15 SEM images of polystyrene films prepared with increasing volume fraction (sphere diameter D = 327 ± 6.0 nm) (a) 0.01 vol.%, (b) 0.05 vol.%, (c) 0.10 vol.%, (d) 0.30 vol.%, (e) 0.50 vol.% and (f) 1.00 vol.%, in which Pa-Pb represents the distance from point a (Pa) on the top to point b (Pb) on the bottom 73
Figure 4-16 Dependence of the film thickness on the volume fraction.....74
Figure 4-17 Linear fit to determine the thickness of the polystyrene film from the Fabry-Perot fringes obtained from the inset reflectance spectrum at incident angle of 10 °.....75
Figure 5-1 SEM images of macroporous silver reduced from various plating solutions (a) silver thiosulfate; (b) silver perchlorate; (c) silver nitrate; and (d) silver sulphate. They all resulted in macroporous structures but surface morphologies are completely different. 80
Figure 5-2 Electrodeposited silver without templating from (a) silver nitrate bath; (b) silver thiosulfate bath. 81
Figure 5-3 Schematic three electrodes setup of copper electroplating using acid $CuSO_4$ bath.....83

Figure 5-4 SEM images of macroporous copper films (a) prepared without 0.10 M copper sulphate solution, showing apparent uneven thickness distribution; (b) prepared 0.10 M copper sulphate solution incorporated with 0.05M chloride ions as additives, showing smooth uniform surface 85
Figure 5-5 SEM images of macroporous copper films prepared using acid Cu^{2+}/Cl^{-} bath with current density i = -5 mA/cm^2 and plating time t = 600 s.....86
Figure 5-6 SEM images of macroporous copper and silver thin films (a) & (c) top surface view, inserts are FFT images obtained from areas of 20 ×20 μm^2; (b) fractured edge of copper film and (d) cross sectional view of silver film, features shaded are from FIB damage.....87
Figure 5-7 Surface features of the thin films (a) colloidal template, (b) corresponding inverted macroporous copper and (c) macroporous silver.....88
Figure 5-8 SEM images of the 3-DOM silver structures (a) high magnification surface view; (b) cross sectional view, revealed by FIB. Both images confirms porous structures are continuous at the bottom but step up to the surface.....89
Figure 5-9 Low magnification SEM top surface view (a) colloidal template and corresponding inverted structures (b) macroporous copper and (c) macroporous silver. The growth directions are indicated by arrows 90
Figure 5-10 Unfilled or filled cracks in macroporous films (a) in copper, drying crack of the polystyrene template is remain; (b) in silver, crack has been completely filled by dense metal 90
Figure 5-11 SEM images of macroporous silver thin film grown from silver perchlorate bath with templating sphere size D = 651 nm and current density i = -2 mA/cm^2, plating time were (a) 600 s; (b) 1800 s; (c) 2400 s and (d) 3600 s.....91
Figure 5-12 Copper reduction and dissolution can be illustrated as reactions in two cells. Total voltage recorded combines potentials of both processes $V_1 = V_2 + V_3$ 94
Figure 5-13 E-T lines of argon degassed and O_2 involved acid Cu^{2+}/Cl^{-} bath, potential difference ΔE is attributed to copper dissolution.....96
Figure 5-14 Top surface view of macorporous copper films plated from oxygen free bath (a) argon degassed solution (b) copper glycerol solution. Red arrows represent crack directions <110>, which were the growth direction of the colloidal templates 97
Figure 5-15 Crack filled films plated from oxygen free copper glycerol bath (a) polystyrene copper composite after plating (b) macroporous structure after toluene dissolving (c) cross sectional view revealed by FIB, the shaded feature is from FIB damage. Filled cracks are marked by arrows 97
Figure 5-16 XRD patterns of electroplated 3-DOM copper and silver thin films.....98
Figure 5-17 XRD patterns of the 3-DOM (a) copper and (b) silver, representing age oxidization.....100
Figure 5-18 EDX analysis of a macroporous films showing presence of oxygen in the one-month old samples 101

Figure 5-19 Voltage-Time responses for cupric ions reduction with various current densities from -3 mA/cm^2 to -12 mA/cm^2. Dashed and solid lines represent the responses for template masked or bare ITO-coated glass substrates respectively 102
Figure 5-20 Linear fit for potential differences with respect to current density of electrochemical reduction of acid Cu^{2+}/Cl^- bath 103
Figure 5-21 Surface view of macorporous copper films plated from various current densities (a) -0.5 mA/cm^2 (b) -2 mA/cm^2 (c) -3 mA/cm^2 (d) -5 mA/cm^2.....105
Figure 5-22 SEM images of macorporous copper films plated from constant current density i = -5 mA/cm^2 but increasing plating time (a) 100 s (b) 300 s (c) 600 s (d) 900 s 107
Figure 5-23 Dependence of number of layers of copper films vs. plating time 108
Figure 5-24 Zygo interferometer images reveal high surface roughness of crack filled films 108
Figure 5-25 Reflectance spectra of a dense copper film prepared with current density i = -5 mA/cm^2 and plating time t = 600 s 109
Figure 5-26 Reflectance spectra of the 3-DOM copper and silver films (templating sphere size D = 327 ± 6.0 nm), showing reflectance peaks correspond to stop bands arising from the periodic modulated structure 110
Figure 5-27 Linear fits for the reflection peaks in Figure 5-26 111
Figure 5-28 Reflectance spectra of the 3-DOM copper films (templating sphere size D = 327 ± 6.0 nm, current density i = -5 mA/cm^2) of plating time (a) 900 s, (b) 600 s, (c) 300 s and (d) 100 s.....112
Figure 5-29 Reflectance spectra of the 3-DOM copper films of templating sphere size (a) 248 ± 5.7 nm, (b) 327 ± 6.0 nm, and (c) 651 ± 23.4 nm 113
Figure 5-30 Chemical formulas of analytes (a) rhodamine 6G and (b) benzotriazole. ...115
Figure 5-31 Reference spectra of (a) R6G and (b) BZT taking using silver colloid using 633 nm laser excitation.....115
Figure 5-32 Background Raman spectrum taking using macroporous silver film grown from silver thiosulfate solution using 633 nm laser excitation 116
Figure 5-33 Raman spectra taking from 3-DOM copper thin film and silver colloids using BZT as target molecule and 633 nm laser excitation 118
Figure 5-34 Raman spectra from benzotriazole taking using macroporous silver using 633 nm laser excitation. 119
Figure 5-35 Raman spectra from increased BZT concentration taking using macroporous silver using 633 nm laser excitation 120
Figure 5-36 Dependence of the Raman intensity on the dye concentration 121
Figure 5-37 Raman spectra from BZT taking using macroporous silver with increasing plating time/film thickness using 633 nm laser excitation 121
Figure 5-38 Dependence of Raman intensity on the macroporous film thickness using 1105 cm^{-1} peak 122

LIST OF TABLES

Table 2-1: Summary of electrodeposited macroporous metals.....32
Table 4-1: Sizes of the polystyrene spheres used in the project 57
Table 4-2: Summary of the information of Figure 4-13 71
Table 4-3: Number of layers and film thickness vs volume fraction.....72
Table 4-4: Fabry-Perot fringes of the spectrum at 10˚ incident angle in Figure 4-17 75
Table 5-1: Stability constants of silver complexes [176].....78
Table 5-2: Macroporous silver from electrochemical growth 80
Table 5-3: Possible reactions in acid Cu^{2+}/Cl^{-} bath 93
Table 5-4: Predicted porous film thickness from Equation 5.32 (μm) 104
Table 5-5: Number of layers of macroporous copper films at current density i = - 5 mA/cm^2 107
Table 5-6: Lattice space and effective refractive index calculated by the reflectance spectra 111

1 INTRODUCTION

This chapter is to introduce fundamental concepts of the three-dimensionally ordered macroporous (3-DOM) materials and the motivation of the research. The outline of the thesis will also be described.

1.1 Introduction to 3-DOM materials

Photons and electrons can be treated analogously as they both simultaneously exhibit particle and wave behaviour. One considerable difference between them is the wavelength scale - the wavelength of electrons is shorter than that of photons. A consequence derived from this feature is that the confinement effect of the photons taken place at larger scales than that of the electrons [1,2]. A crystal lattice of periodic arrangement of atoms or molecules presents a periodic potential to propagate electrons. As for the propagation of photons, the lattice will be replaced by materials with periodic dielectric contrasts varied in micron or sub-micron range, usually termed photonic crystals [3-9]. For example, woodpile stack with micro-scale lattice constant, as illustrated in Figure 1-1(a), can be used as optical filters in infrared or microwave wavelengths [10-14]. The lattice was consisted of one-dimensional rods in ABCDABCD…sequences, in which the orientation of layer A and B are orthogonal while C and D are layers offset to A and B respectively by half of the horizontal spacing. On the other hand, in an artificial crystal made of micron sized column arrays, a linear defect is designed by removing a sequence of nanopillars, as shown in Figure 1-1(b). Light can be guided from one location to another along the defect or be

confined in the defect. The structure can find applications in optical waveguides or other optoelectronic devices [15-18].

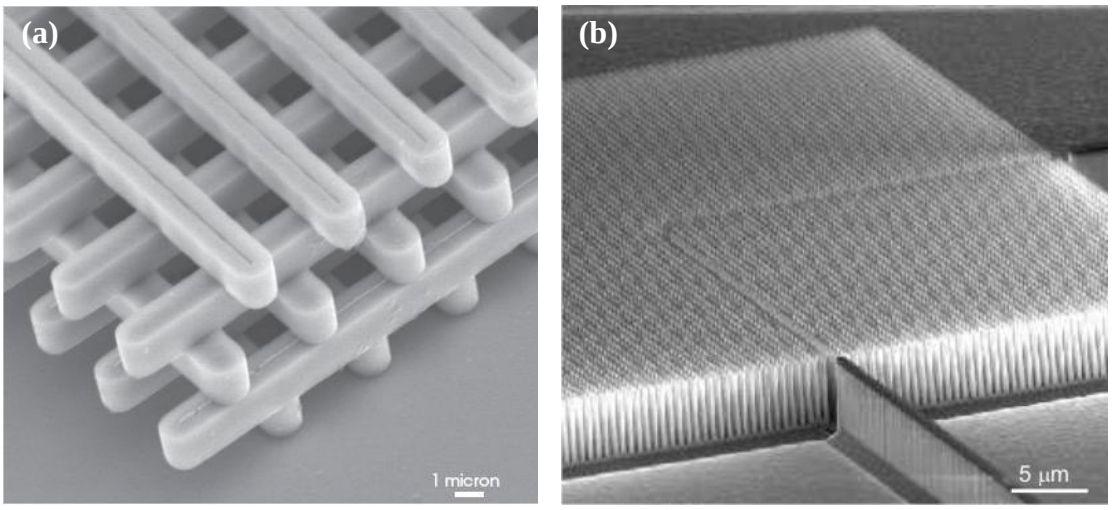

Figure 1-1 Photonic crystal structure with three-dimensional periodicity (a) layer by layer of one-dimensional rods with a stacking sequence that repeat itself every four layers [12]; (b) a waveguide carved by introducing linear defect in crystalline array [17].

The challenge of producing the photonic crystals with lattice constant in microns or below has led nanolithography to be routinely employed [10,19-30]. However, formidable processing difficulties limited the formation of more than a few layers. Templating technique has thus been employed to grow multi-layered photonic crystals [31-37]. It involves firstly the formation of a temporary medium, which is typically made of easily removable liquid droplets [7,36-40] or solid particles [41-46] [32,34,47-50]. The template spheres are monodisperse at the requisite scale and can be assembled into a crystalline array usually face-centred cubic (f.c.c) spontaneously, see Figure 1-2(a). The interstitial spaces of such artificial crystal will be infiltrated with another material. Subsequently the template is removed and leaves behind an inverse replica - close packed spherical voids embedded in a solid matrix. Since the resulting architecture is a three-dimensional arrangement of highly ordered pores, as illustrated in Figure 1-2(b), it is known as three-dimensionally ordered macroporous

(3-DOM) material.

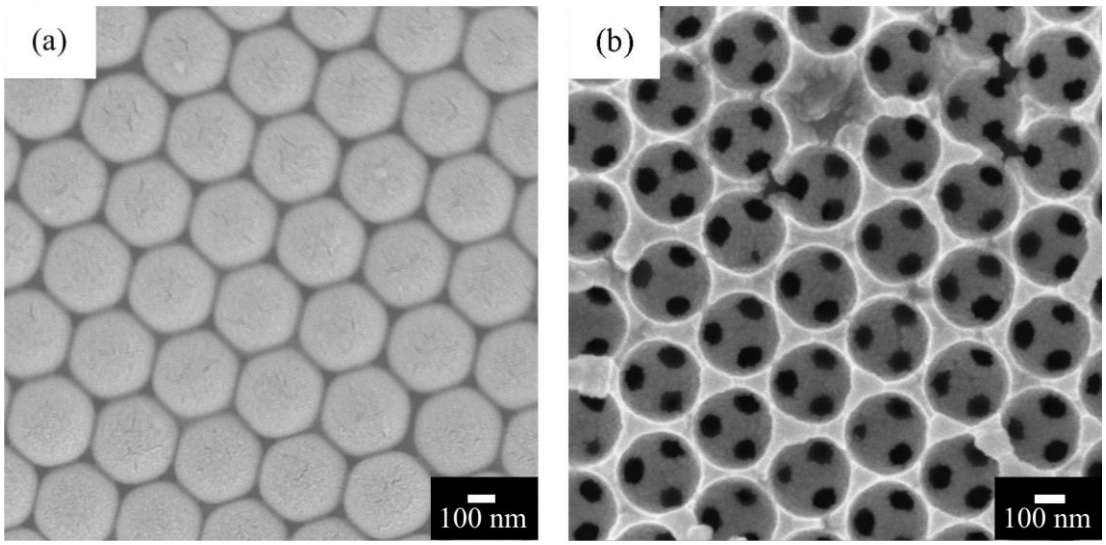

Figure 1-2 Structural features of 3-DOM materials (a) top surface SEM image of polymer crystalline array and (b) corresponding inverse 3-DOM copper, consisted of highly ordered pores in solid copper matrix (present work).

1.2 Research motivation

The dielectric contrast of the 3-DOM materials varies periodically, which enables them manipulate the photons in the same way that semiconductors control the electrons. According to theoretical studies, to exhibit a photonic band gap (PBG) that forbid the propagation of photons from all directions, the threshold value of the dielectric contrast must be over 2.8 [51-53] for close packed f.c.c lattice of air spheres with high index material in the interstitial space. From a practical point of view, this means that the PBG is not achievable other than in semiconductors of high refractive index. Silicon, for example, has a very high refractive index of ~3.50. It is an excellent candidate for the manipulation of photons in the infrared (750 nm to 100 μm) and microwave (1 mm to 1m) ranges [11,54-61].

The dielectric function ε is composed of both real (ε_{re}) and imaginary (ε_{im}) parts:

$$\varepsilon = \varepsilon_{re} + i\varepsilon_{im} \quad \textbf{(1.1)}$$

The real part ε_{re} represents scattering properties of the material while the imaginary part ε_{im} contains adsorption of light. In general metals have high real part of dielectric function, as illustrated in Figure 1-3, silver has the highest reflectance of any metal from 400 nm (3.10 eV) to 50 μm (0.02 eV). The reflectance of silver in the ultraviolet, visible, and infrared portion of the spectrum is approximately 99%, but the reflectance drops off sharply below 400 nm in the ultraviolet. Gold and copper exhibit reflectance as high as 98-99% before drop off below ~520 nm (2.38 eV).

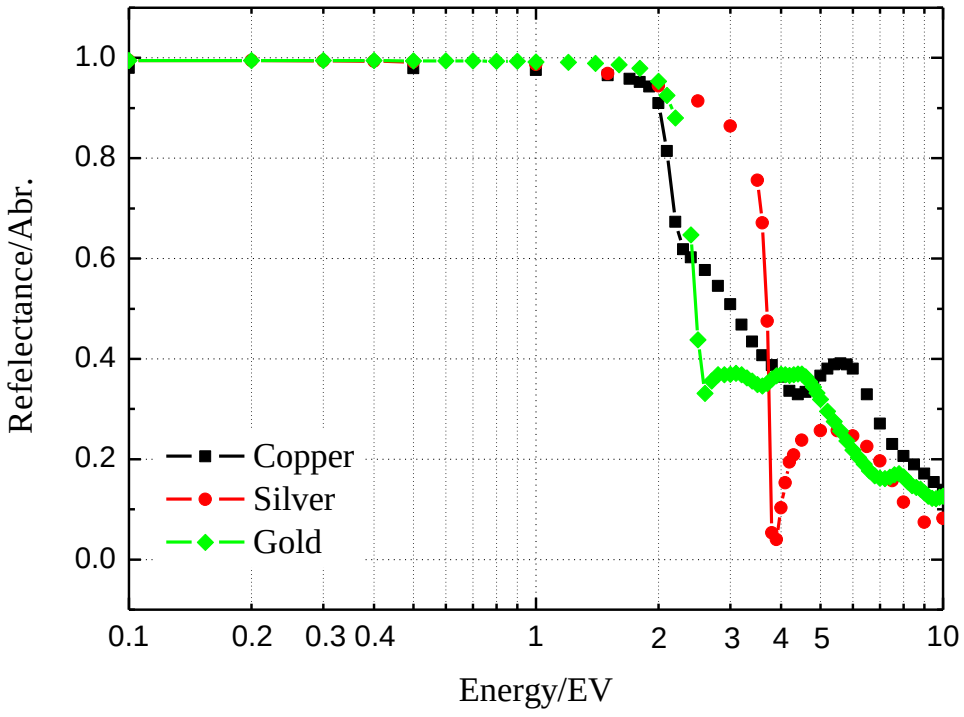

Figure 1-3 Spectral reflectance of silver, gold and copper as a function of the radiation energy at normal incidence [62].

However, both semiconductors and metals strongly absorb visible light due to their negative imaginary part in the visible wavelength range. There seems unlikely to to find an appropriate material in the visible or near-infrared (380 to 750 nm) regime

with f.c.c lattice. It was not until 1999 theorists predicted that in three dimensional metallic artificial crystals, the imaginary part of certain noble metals such as gold, silver and copper could be negligible in a certain frequency window, in which they behave as a conventional dielectric [63-65]. According to a Drude-like dielectric function, the dielectric function of the metallic matrix ε_m is determined by [63]

$$\varepsilon_m(\omega) = 1 - \frac{\omega_p^2}{\omega^2} \qquad \textbf{(1.2)}$$

where ω_p is the Plasma frequency. Since $\varepsilon_m(\omega_p) = 0$, the dielectric contrast of the structure $\varepsilon_\delta = max\ (\varepsilon_m/\varepsilon_{air},\ \varepsilon_{air}/\varepsilon_m)$ becomes extremely large for frequencies around ω_p. And thus 3-DOM materials made of noble metals would be ideal candidates to overcome the limit of manipulating wavelengths, among which silver performs the widest range in the visible frequencies [65]. Additionally surface enhanced Raman scattering (SERS) has almost been found exclusively in the noble metals. Such 3-DOM metallic structures can also be used as robust SERS-active substrates.

We chose to study 3-DOM silver and copper as an attractive alternative to gold which has been the subject of investigation in the past a few years [66-72]. These are cheaper alternatives of the 3-DOM gold in most applications and especially silver is predicted to have higher dielectric contrast. However porous structured silver or copper can only been seen on very limited reports to date [73,74], among which only two-dimensional monolayer film has been presented.

1.3 Thesis outline

As the title states, the thesis is concerned with the preparation and characterisation of 3-DOM metals such as silver and copper through electrochemical deposition. The first chapter gives the basic concepts of the 3-DOM materials and

introduces the motivation of the research.

Chapter 2 reviews the origins of photonic band gap, especially the band gap in the f.c.c arrangement 3-DOM materials. Surface enhanced Raman scattering is reviewed from origination, enhancement mechanism to geometry of the SERS-active substrates. A range of fabrication strategies for the colloidal crystals and subsequent inverse metallic structures – the 3-DOM metals are described and compared, among which evaporation-induced self-assembly and template-directed electrochemical deposition are highlighted respectively.

Chapter 3 reports the main characterisation techniques that have been used in the thesis. The structures were examined using optical microscopy and scanning electron microscopy (SEM); the optical properties were studied using reflectance spectroscopy; the surface oxidation were analysed by X-Ray diffraction (XRD) and Energy dispersive X-rays (EDX); and the application of the prepared structures as plasmonics was evaluated using Raman spectroscopy.

Chapter 4 describes the preparation of monosized polystyrene spheres and thin polystyrene films. Three different sphere sizes in sub-microns were employed and the quality of the films was monitored through controlling the growth parameters such as substrate, sphere polydispersity, incubator temperature and relative humidity. Optical properties of the polystyrene template films were analysed as well.

Chapter 5 demonstrates the electrochemical deposition technique for growing 3-DOM silver and copper films directed by the polystyrene template films. The aim was to form uniform macroporous structure over large length scales. The experiments associated with a range of bath solutions are discussed to develop a greater understanding of the growth process. In addition, preliminary measurements on the 3-

DOM metals used as SERS-active substrates are discussed.

Chapter summaries are presented at the end of each chapter but Chapter 6 concludes the thesis with an overall conclusion and a discussion on possible future work.

2 LITERATURE REVIEW

In this chapter we will review the origins of the photonic band gap and characteristics of the band gap in 3-DOM materials. Surface enhanced Raman scattering (SERS) will be reviewed to demonstrate the mechanism of the 3-DOM materials used as plasmonics. A variety of fabrication strategies assisting colloidal crystal templating are described, among which colloidal convective self-assembly and electrochemical infiltration will be highlighted.

2.1 Photonic band gap

2.1.1 Origins of photonic band gap

Interaction of electromagnetic waves with periodic structures follows Bragg's law, as illustrated in Figure 2-1, in which planes of atoms act as perfect mirrors to beams of electromagnetic waves when Bragg condition is met,

$$\lambda = 2d\sin(\theta \pm \delta) \tag{2.1}$$

where λ is resonant wavelength, governed by the crystal plane spacing d and angle of incidence light θ. In fact, the perfect mirror behaviour holds over a range of angles, $\pm\delta$, determined by how strongly the atoms scatter photons. As a consequence, light is forbidden in certain range of angles. A crystal contains many possible Bragg planes reflecting light from different directions, as shown in Figure 2-2(a); when the scattering is strong enough to overlap different Bragg planes, see Figure 2-2(b), the light will be reflected whatever the incident angle. The certain frequency range in

which Bragg reflection forbids photons propagate through is called a photonic band gap, analogous to the electronic band gap in semiconductors.

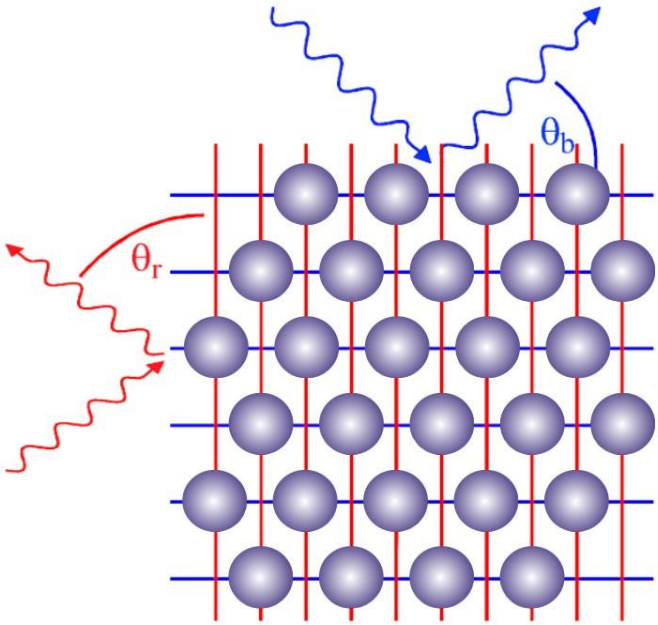

Figure 2-1 Bragg reflection occurs when resonant wavelength matches lattice spacing and incident angle.

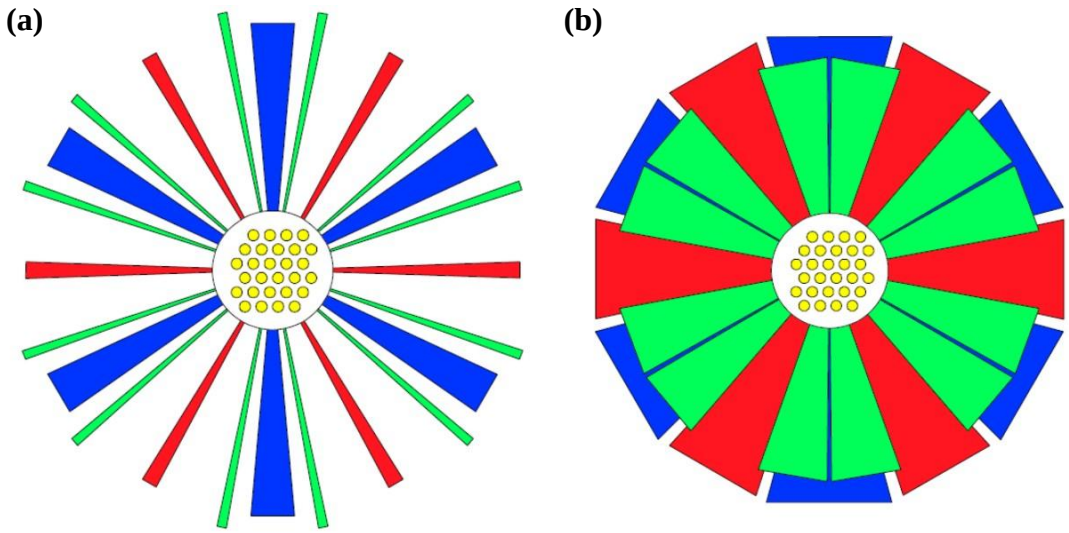

Figure 2-2 Bragg scattering in crystals (a) each set of planes acts as a mirror in a small range of angle; (b) each set of planes acts as a mirror in a large range of angles which overlap completely.

The concept of Bragg's reflection in crystals can be applied equally to

artificial crystals that are periodic on the scale of sub-microns. In 1887 Lord Rayleigh described the propagation of electromagnetic waves in a one dimensional periodic structure, which was later identified as an angle-dependent band gap in his paper 'On the maintenance of vibrations by forces of double frequency, and on the propagation of waves through a medium endowed with periodic structure [75]. Such one dimensional systems continue to be studied extensively, and have found industrial applications from layered optical interference filters reflective coatings to distributed feedback lasers [76-79]. It was not until a century later, in 1987, that two- and three-dimensional (2-D and 3-D) photonic band gaps were proposed by Yalblonovitch [80-85], and independently by John [86-89], each with a different motivation.

Yalblonovitch, then at Bell Communications Research in New Jersey, was looking for an efficient communication laser that suppresses electric current waste as spontaneous light emission and suggested that the photonic band gap in a three dimensionally periodic dielectric structure can inhibit spontaneous emission [82]. A few years later [80], Yablonovitch and co-workers produced the first photonic crystals by mechanically drilling holes a millimetre in diameter into a block of material with a refractive index of 3.6. The structured material, known as 'Yablonovite', prevented microwaves from propagating in any direction – in other words, it exhibited a 3-D photonic band gap. His proposed architecture was an arrangement of dielectric cubes in a face-centred cubic (f.c.c) lattice, producing a 3-D chequerboard structure. In later experiments, the cubes were replaced by spheres [83]. The first experimental structure with a photonic band gap consisted of air spheres on the sites of an f.c.c lattice in a dielectric background. The structure, however, had a pseudo-gap rather than a complete photonic band gap for the range of frequencies examined [85].

John, from a pure theoretical view, hypothesized that the photonic band gap

was able to localize photons [87]. He stated that strong localization of photons may occur in certain disordered super lattice microstructures of sufficiently high dielectric contrast. These materials are the photonic analogue of amorphous semiconductors, in which the interplay between order and disorder leads to the restriction of coherent back-scattering to certain Bragg resonance channels.

2.1.2 Photonic band gap in 3-DOM materials

As described above, a photonic band gap (PBG) is a range of frequencies in which the propagation of light is forbidden. If the width of the band gap is large enough to overlap those of any other directions, then no light will propagate through. It is called a complete PBG [60,63,90]. Strictly speaking a complete PBG only exists in three-dimensional structures. One or two dimensional structures cannot define sets of lattice planes leading to Bragg reflection in directions where it is not periodic, as illustrated in Figure 2-3 [3,26,91-95].

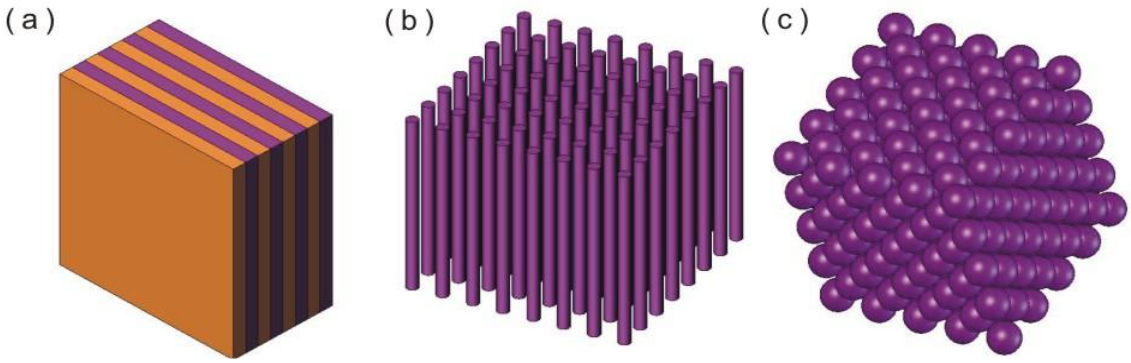

Figure 2-3 Real space schematic representation of (a) one-dimensional; (b) two-dimensional; (c) three-dimensional photonic crystals.

In principle, the existence of a photonic band gap in the 3-DOM materials depends on several parameters of which the most important are lattice symmetry, dielectric contrast and filling fraction [96,97]. The symmetry of a lattice is represented

by its Brillouin zone which is defined in the reciprocal lattice as the fundamental periodic region. In an example illustrated in Figure 2-4, the higher symmetry of the hexagonal lattice is reflected by the fact that the Brillouin zone is closer to circular than the square lattice. When the Brillouin zone becomes as close as possible to a circle, the interference occurs along all directions for the same wavelength.

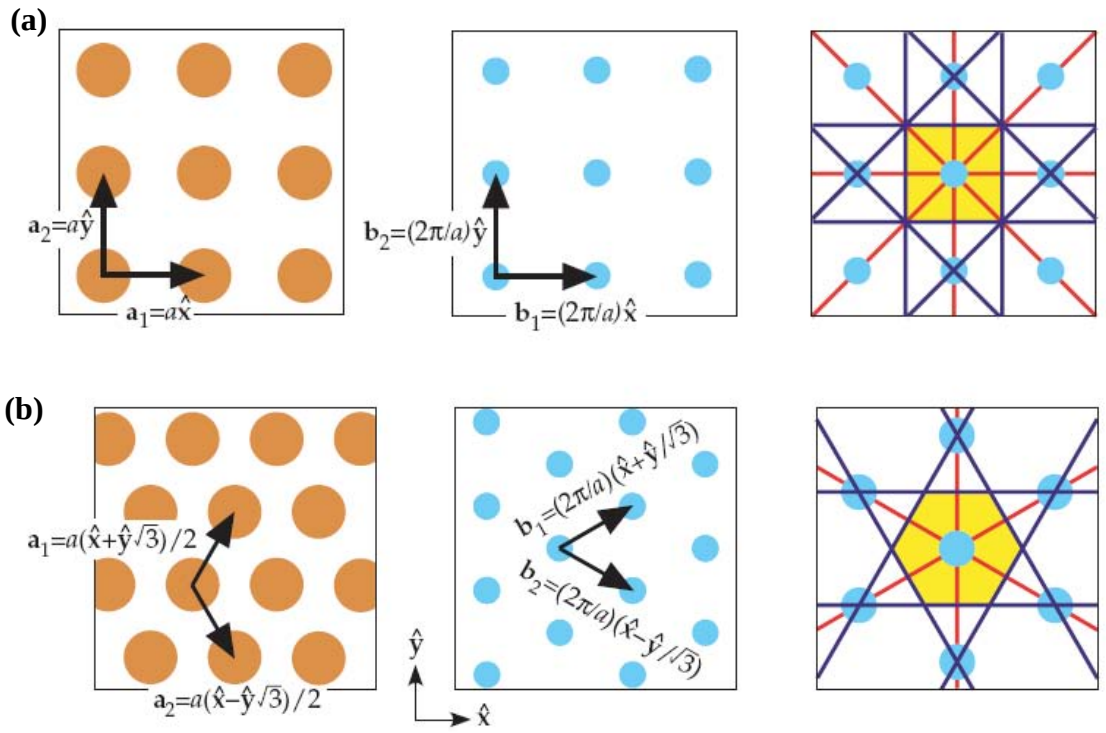

Figure 2-4 Real and reciprocal space representation of two-dimensional (a) square lattice and (b) hexagonal lattice [3,98]. The left images are real lattices, the middle ones are corresponding reciprocal lattices, and the right ones are construction of first Brillouin zone (yellow regions).

3-DOM materials consist of f.c.c arrangement of air spheres in a dielectric matrix while the Brillouin zone of an f.c.c lattice is the most spherical one of all possible 3-D lattices, as shown in Figure 2-5, in which the interference will occur along nearly all spatial directions. The f.c.c lattice is therefore initially favoured to yield a complete photonic band gap [80,81,99,100]. However the farthest symmetry point W is 29% farther from the origin than the closest point, the L point. For a gap to open along every direction, the gaps at W and L must be large enough to overlap

[101]. At the W points, the conduction and valence bands cross each other indicated that an f.c.c lattice geometry only possess a pseudo PBG between the 2nd and 3rd bands even for arbitrarily high dielectric contrast [97,102]. Computational simulations predicted that the complete PBG of the f.c.c structure exist actually between the 8th and 9th bands [99,103].

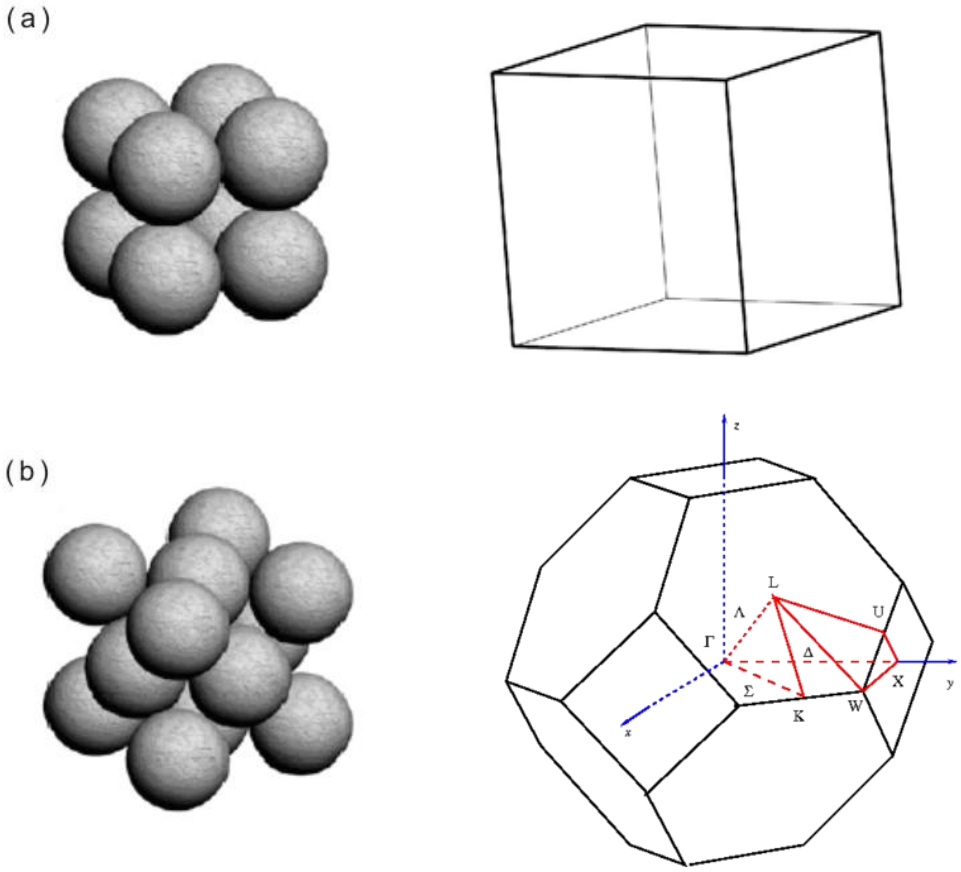

Figure 2-5 Bravais lattices and their corresponding first Brillouin zones (a) simple cubic; (b) face-centred cubic [104].

In addition, filling fraction is another crucial parameter to achieve a complete PBG [105,106]. It is the ratio between the volume occupied for each dielectric material with respect to the total volume of the composite. Theoretically in an inverse opal of f.c.c lattice, the filling fraction is 26%. However, the air voids can be isolated or interpenetrated, and consequently the filling fraction decreases while the contact

area of the templating spheres increases, as illustrated in Figure 2-6. The decrease of the filling fraction will shift the band gap edge to lower frequencies [13,98] and correspondingly the low filling fraction inverse structure (Figure2-6(b)) presents wider band gaps than the inverse replica shown in Figure 2-6(a).

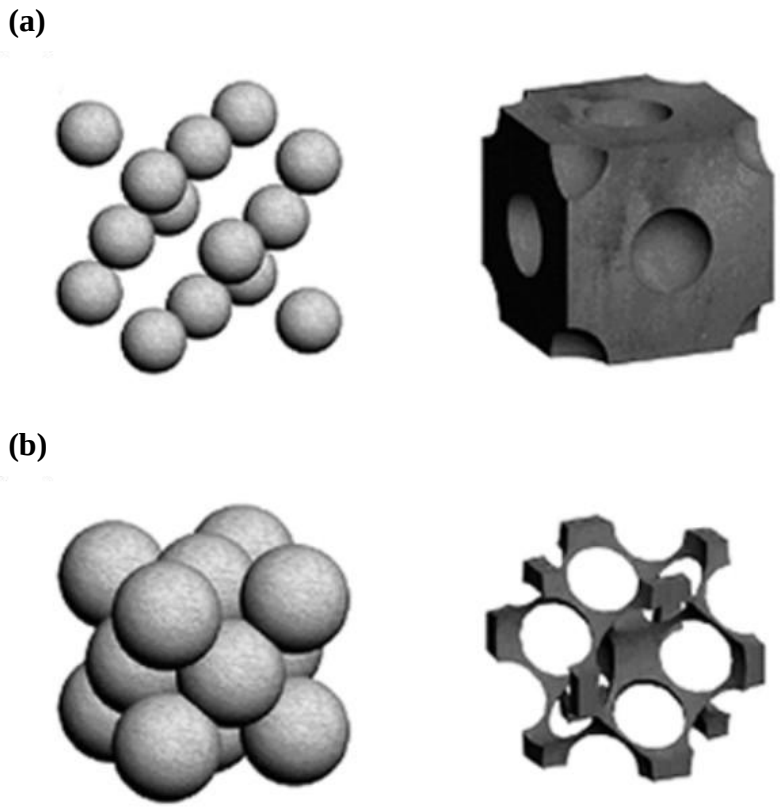

Figure 2-6 A lattice may present different topographies here take f.c.c for example. (a) isolated dielectric spheres in air and corresponding inverse structure - isolated air spheres in a dielectric solid; (b) interpenetrated dielectric spheres in air and corresponding inverse structure - interpenetrated air spheres in a dielectric solid.

2.2 Surface enhanced Raman scattering

2.2.1 Brief history of SERS

When a molecular system is illuminated by a laser beam, the photons may be scattered or adsorbed, or may not interact with the system but pass straight through. If the energy of an incident photon matches an energy gap between the ground and

excited states of a molecular, the photon will be absorbed and the molecule is promoted to an excited state. The adsorption is called infrared adsorption and can be detected by measuring the loss of the radiation energy. However, photons may scatter from the molecule. If only electron cloud distortion is involved in the scattering, the photons will be scattered with little frequency changes. This process is regarded as an elastic scattering and is called Rayleigh scattering. However, a very small fraction (about 1 out of every 10^7) undergoes inelastic scattering, in which the nuclear motion is induced and energy transfers either from the incident photon to the molecular or from the molecule to the scattered photon. This process is inelastic and is called Raman scattering [107,108].

The inelastic scattering was first experimentally observed by Indian physicist C.V. Raman in 1928 [109]. He used a narrow band photographic filter to run sunlight into a monochromatic light. It was then focused by a telescope objective onto a sample which was either a purified liquid or a dust-free vapour. A system of crossed optical filters was used to block the monochromatic light but Raman found that light of changed frequency passed through the crossed filter.

Figure 2-7 shows that the basic scattering process. The photon interacts with the molecule and polarizes the electron cloud around the nuclei. At that instant, the energy is transferred to the molecule but the nuclei do not have time to move appreciably. This results in a high energy form of the molecule without any large nuclear movement. The state is not stable and the photon is released immediately as scattered radiation. Such interaction between the photon and the molecular can be considered as the formation of a short-lived state, which is called virtual state of the molecular. The Rayleigh scattering does not involve any energy change and consequently the molecular returns to the same energy state. If the molecular adsorbs

energy and is promoted from ground vibrational state *m* to a higher excited vibrational state *n*, this is called Stokes scattering. However due to the thermal energy, a few molecules may be present in an excited state *n*. Energy can be transferred to the scattered photon and the molecular returns the ground state *m*. This process is called anti-Stokes scattering.

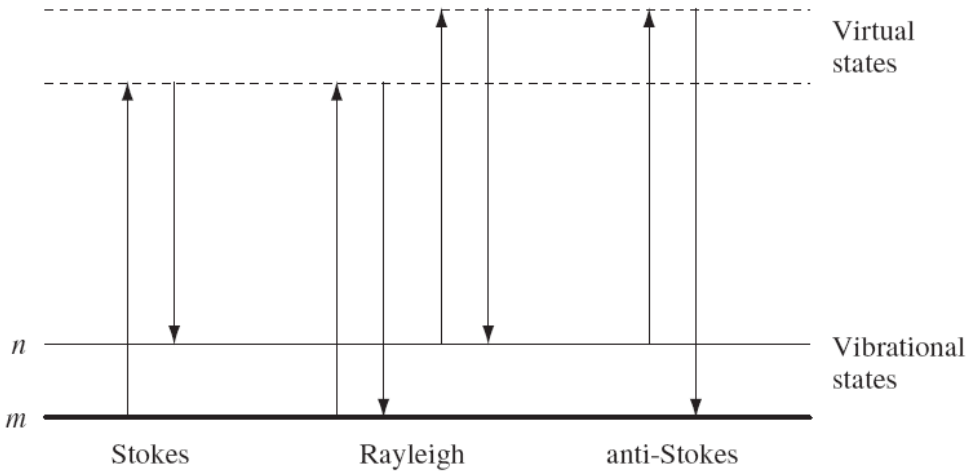

Figure 2-7 Diagram of Rayleigh and Raman scattering. The letter *m* represents ground vibration state and *n* is for a higher excitation state.

In many applications, Raman scattering has very low detection sensitivity. A Raman technique with enhanced sensitivity would be valuable. In 1974 surface enhanced Raman scattering (SERS) was discovered to give an enhancement up to about 10^6 in scattering efficiency over usual Raman scattering [110]. The initial observation was made by Fleischman *et al.* who reported strong Raman scattering from pyridine molecules on a roughened silver electrode. They attributed the effect to an increase in the electrode surface area and therefore a larger amount of pyridine molecules to be absorbed. However in 1977 Van Duyne *et al.* [111] and independently Creighton *et al.* [112] recognized that the enhancement could not be attributed to the high surface area alone. The increase of Raman signal from roughed

surfaces would be less than a factor of 10, whereas the enhancement was of the order of 10^6.

2.2.2 Enhancement theory

Before going to the theory, it is necessary to understand the nature of the metallic surface. The surface is covered by electrons. They are conduction electrons and being hold by positive charges on the metal side. The electron density extends a considerable distance from the surface to the space. When a photon interacts with these electrons, they begin to oscillate as a collective group across the surface. The oscillations are termed surface plasmons. On a perfect smooth surface the oscillation occurs along the surface plane and no photon will be scattered. Therefore the surface is roughened to realize an oscillation perpendicular to the surface.

Many theories have been proposed, particularly in the early days, to interpret the SERS. However, the exact mechanism of the SERS enhancement is still a topic of current debate. It is generally accepted that there are two primary contributions to SERS - a chemical enhancement and an electromagnetic enhancement [4,113-117].

2.2.2.1 Chemical enhancement

The chemical enhancement is arising from charge transfer between the metal and chemisorbed molecules at the surface of the metallic nanostructure. It involves the formation of a molecule-metal complex. The molecular orbitals will be broadened by an interaction with the conduction band of the metallic surface. The new electronic state is believed to be a resonant intermediate in the Raman scattering. In contrast to the radiation being adsorbed or scattered through the plasmons on the surface, the radiation is absorbed into the metal, creating an electron-hole pair inside. The energy

is transferred via the hole to the molecule-metal complex, the Raman process then occurs - excitation is transferred back into the metal and re-radiation occurs from the metal surface. However the chemical enhancement only applies for molecules which have formed a bond with the surface and clearly cannot explain the observed signal enhancement in those cases where the molecular is only physisorbed to the surface. The quantitative estimation of the chemical enhancement factors ranges from 10 to 10^2 [118].

2.2.2.2 Electromagnetic enhancement

The electromagnetic enhancement originates from the strong interactions between the molecules and the surface plasomons. When the molecular is adsorbed onto the metallic surface, it is surrounded by the free surface electrons. The intensity of Raman scattering I is proportional to the square of the magnitude of the electromagnetic field E incident on the molecular,

$$I \propto E^2 \qquad \textbf{(2.2)}$$

As stated above, the collective oscillation of the surface electrons is a surface plasmon while surface roughness or curvature is compulsory for the plasmon excitation. The energy of the surface plasmon is delocalized in the direction parallel to the surface but localized in the perpendicular direction, leading to the magnitude of electromagnetic field E on the surface greatly enhanced. In addition, the surface electrons are loosely held and are free to couple with adjacent curvatures so that the plasmon can be arising from more than one curvature [115,119]. The touch point of the two curvatures will generate enormous electric fields so that it will give particularly effective SERS. The maximum enhancement factors from the electromagnetic effects have been reported to be 10^6 to 10^7 [113,120].

2.2.3 3-DOM metals as SERS substrates

SERS has been observed from a limited number of metallic surfaces. It was primarily from coinage metals such as gold, silver and copper, with excitation wavelength near or in the visible region [121-125]. Other metals, such as palladium, rhodium or platinum, exhibit enhancement of about 10^2 -10^3 for excitation in the near ultraviolet [126-128]. Alkali metals have also been reported to have high enhancements but they are over active in chemistry [129]. It is well known the enhancement is a direct consequence of presence of microscopic metallic domains, which can be developed in a number of ways, such as roughened metallic electrodes [110,111,130,131], metallic nanoparticle arrays [91,132-137], metallic gratings [134,136,138-140], metal colloids or nanoclusters [27,113,119,141-150], and ordered macroporous metallic thin films [67,68,135,151-155].

In the case of the 3-DOM metals, recent reports demonstrated that they possess excellent features - robust, reproducible, and easy to fabricate that are particularly well suited for SERS detection [66-68,72,121,128,153,156-159]. Although the physics of the electromagnetic enhancement effect remains substantially the same when a molecule is adsorbed near a nonspherical metal particle, ordered porous metallic nanostructures possess several advanced features that are particularly well-suited for a SERS signal enhancement. Firstly, a long-range periodicity has been demonstrated to improve their performance as SERS substrates. According to Gaponenko [160,161], the photon density of states redistribution may readily occur in periodic porous metal nanostructures, which leads to an increase of the density of optical modes and thus to a superior enhancement of the Raman intensity of the target molecules. Secondly, SERS is a very local phenomenon occurring inside the pores. The electromagnetic enhancement has been regarded as a direct consequence of

localised surface Plasmon excitation. Importantly, a large electric field enhancement can also occur between these neighboring macropores, allowing for a further increase of SERS signal intensity. Thirdly, porous structures can provide high surface areas that allow more analytes to adsorb and thus an increasing the number of target molecules.

2.3 Fabrication strategies of colloidal crystal templating

Colloidal crystals are crystalline arrays formed spontaneously from monodisperse colloids such as silica or polymer nanoparticles [162-167]. They only possess partial photonic band gaps due to the low dielectric contrast (typically 1.4 - 1.6) between the colloidal spheres and the surrounding medium. Promisingly, there are regular interstitial spaces between the colloidal spheres, for instance, the free space of an f.c.c or h.c.p lattice is 26%, and another material can incorporate into the interstices. The colloidal particles can be removed, either chemically or thermally, resulted in an inverse replica of the colloidal crystals. Colloidal crystal templating has the advantage of being able to create large area crystals at a low cost.

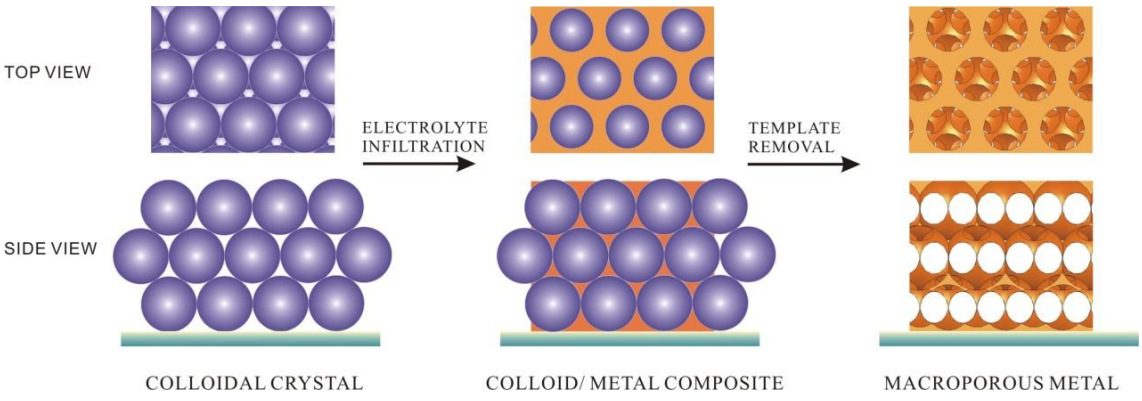

Figure 2-8 Schematic process for colloidal crystal templating.

The 3-DOM metallic photonic crystals are predominantly fabricated through

the colloidal crystal templating approach. The procedure is illustrated in Figure 2-8. Briefly, monodisperse colloidal particles are assembled into a colloidal crystal on a substrate; the free spaces between the particles are subsequently infiltrated with the desired metal elements by an appropriate technique, for instance, electrochemical plating or nanoparticle infiltration; finally the colloidal particles are selectively etched away, leaving behind a periodic arrangement of spherical voids embedded in a solid macroporous matrix.

2.3.1 Self-assembly techniques of colloidal crystals

Several methods have been developed for crystallizing spherical colloids into ordered lattices, including sedimentation, spin-coating, patterned deposition and convective assembly, all of which will be discussed here.

2.3.1.1 Sedimentation

Colloidal crystallization by sedimentation, one of the most common techniques to form self-assembled layers of colloidal spheres, involves natural gravitational settling [168-173] and electrophoretically [174-176] controlled settling.

While sedimentation relies solely on gravity to settle colloidal particles down to a substrate, the procedure is conceptually straightforward and simple. However, it has some inconveniences. Firstly, there is very little control over the morphology of the top surface and the number of layers in the crystalline arrays. Numerous defects such as stacking faults, dislocations, grain boundaries and vacancies may be formed during gravitational sedimentation [170]. Layered sedimentation may occur, which usually leads to the formation of a number of layers of different densities and orders along the direction of the gravitational field [175]. Secondly, the sedimentation time

depends strongly on the sphere size. Particles of small sizes (< 300 nm) require weeks or months to settle because the gravitational forces of the particles are compensated by their thermal agitation according to the Boltzmann's distribution function. About three weeks were needed to form a 10 mm high colloidal crystal for 330 nm and 460 nm spheres and at least six weeks were needed for 200 nm spheres [165,177]. On the other hand, the gravitational energy of large spheres (> 550 nm in diameter) is much larger than the thermal energy so that the sedimentation occurs far from equilibrium and non-crystalline sediment is obtained and it becomes completely impossible to achieve an ordered array if the diameter is further increased. Therefore, the sedimentation growth is practically limited to particles of diameters in the range of 300 to 550 nm.

In the electrophoretic deposition (EPD) vertical electrical fields are applied across a suspension of spheres in which charged colloidal particles are attached to and deposited on to an oppositely charged conducting substrates such as indium tin oxide (ITO) or gold coated glass slides, as shown in Figure 2-9 [175,176]. Depending on field direction, the field guides the growth and accelerates the speed of small particles while inhibiting the large ones. It offers a good solution for the natural sedimentation problem mentioned above. The order in artificial opals can be improved by adjusting the sedimentation rate and the film thickness can be controlled by changing the EPD time. However, care has to be taken to avoid electrolysis, which is a main problem of carrying out the EPD in aqueous suspension is the decomposition of water,

$$6H_2O(l) \rightarrow 4H_3O^+(aq) + O_2(g)\uparrow + 4e^- \qquad \textbf{(2.3)}$$

The bubbles of oxygen formed at the anode may penetrate through the deposited compact, which subsequently prevents the formation of ordered crystalline arrays.

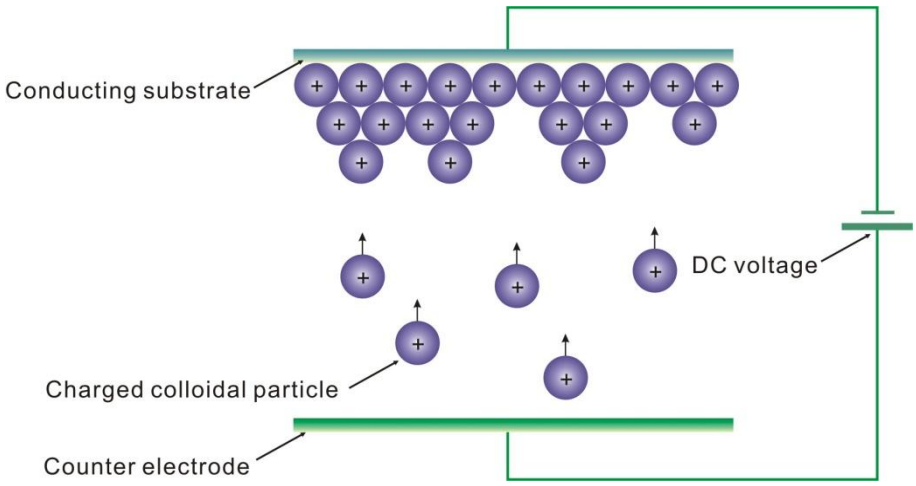

Figure 2-9 Experimental setup of electrophoretic cell [175].

Despite their advantages and disadvantages, both sedimentation methods generally result in polycrystalline lattice domains [178,179], which is caused by simultaneous nucleation in different locations of the sample surface. Subsequent growth of crystalline domains in various directions leads to the formation of random orientation in the crystalline grains. If the process is considerably slow, the colloidal spheres concentrated at the bottom will undergo a hard-sphere disorder-to-order phase transition to form a three-dimensionally ordered lattice [180]. The resulting domains have various sizes but predominantly face-centred cubic (f.c.c) packing or random hexagonally close packed (rh.c.p) planes.

2.3.1.2 Spin-coating

In order to accelerate the crystal manufacturing process, spin-coating of the latex particle suspension has been investigated [181-183]. An excess of colloidal suspension is dispensed on a hydrophilic substrate which is then accelerated to a fixed rotation rate. Initially most of the suspension is cast off the substrate due to centrifugation, leaving behind a film that thins continuously due to radial outflow and

solvent evaporation. As the suspension becomes more concentrated and viscous, the film continues to thin until all the solvent has evaporated thoroughly leaving a "dry" film of the suspended material. A schematic of this procedure is shown below in Figure 2-10. The colloidal particles organize themselves into an ordered array more rapidly compared to sedimentation so that the close-packed arrays can be obtained in hours.

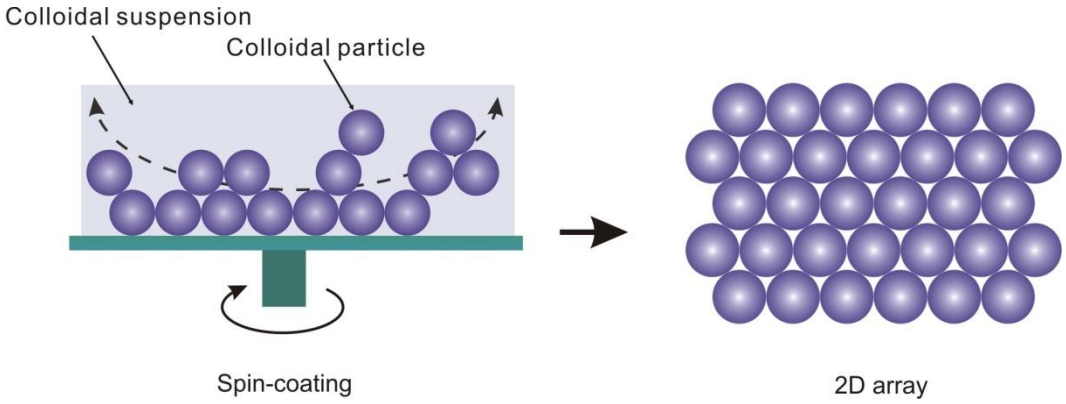

Figure 2-10 Illustration of producing 2D colloidal crystal by spin-coating [182].

Spin-coating is a method to produce thin, uniform films of precise thickness. Several factors known to affect the polymer film thickness include the concentration of the polymer and spinning speed. Spin-coating is the preferred method when multi-layers need to be sequentially deposited. As an example of sequential production, Mohwald *et al.* [182] fabricated a well-ordered binary colloidal crystals by the spin-coating of latex particles with large diameter ratios. The approach is fast and simple while exhibiting tolerance to the polydispersity of the spheres. In addition, the spin speed provides another parameter for controlling over the structures of the resulting binary colloidal crystals.

2.3.1.3 Convective self-assembly

The convective self-assembly technique relies on capillary forces to organize colloidal spheres [92,95,184-187]. Figure 2-11 shows this process whereby a hydrophilic substrate is dipped in a suspension, drawing a wet film upward along the substrate, forming a water-air interface highly inclined toward the substrate. Thus, the induced capillary force arises and pushes particles out of the meniscus. The ordering process starts when the thickness of the liquid layer becomes smaller than the diameter of the particles due to the evaporation of the liquid. Continuous evaporation results in a convective flow of the surrounding suspension. The successive inflow of the colloidal particles is sustained until the liquid has completely evaporated.

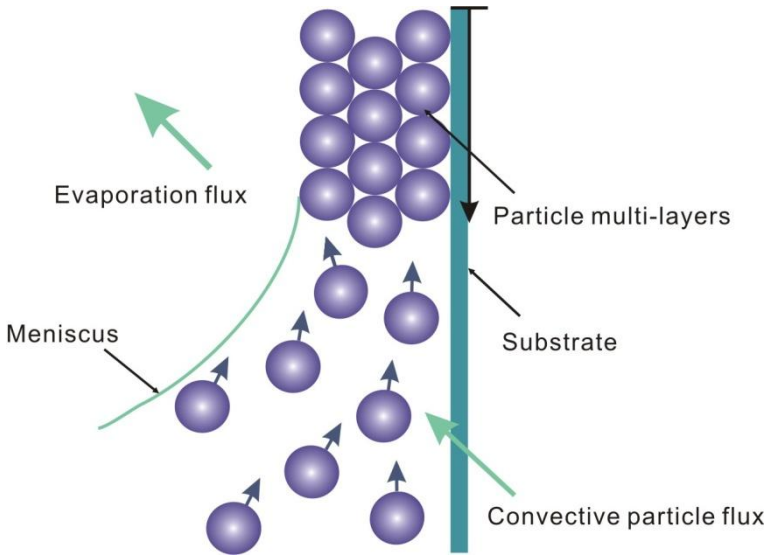

Figure 2-11 Sketch of particles and water fluxes in the vicinity during convective self-assembly [92].

Convective self-assembly has the advantage of producing well-ordered films on planar surfaces quite rapidly. The array has a uniform orientation over centimetre length scales and can be fabricated with thicknesses ranging from two layers to several hundred layers (up to hundreds of microns). The resulting planar colloidal crystals are highly ordered, and evaporation of the solvent leaves a latex-air array with

good optical contrast and mechanical stability. In convective self-assembly the colloidal spheres are brought together by inter-particle capillary forces in the meniscus to form into an ordered close-packed array that is generally a face-centred cubic (f.c.c) lattice [46,188,189].

Moreover, the thickness of the resulting sample can be precisely dictated through control of sphere size and solution concentration. The thickness of the film is given by [92],

$$k = \frac{\beta l}{0.605} \frac{j_e \varphi}{v_c d(1-\varphi)} \qquad \textbf{(2.4)}$$

where k is the number of layers, β is the ratio between the velocity of a particle in solution and the fluid velocity (a constant depending on particle-particle and particle-substrate interactions, taken as a value of 1 for non-absorbing particles and dilute suspensions [186]), l is the height of the meniscus, φ is the colloid volume fraction, j_e and v_c is the particle and colloid velocity, respectively, and d is the diameter of the colloid spheres. From Equation 2.4, when conditions such as the sphere size, the evaporation temperature, and the relative humidity are certain, the number of layers can be precisely adjusted by the volume fraction of colloid suspensions.

2.3.1.4 Patterned deposition

The self-assembly process typically forms close-packed two-dimensional or three-dimensional arrays of colloidal particles but restricts more complex geometries. In order to induce growth along a specific crystal plane, patterned substrates have been used [20,190-194]. In a typical process, a substrate is initially patterned chemically, electrically or physically. The suspension of the colloidal particles is then confined in a purpose-built cell whereby it slowly evaporates and the meniscus moves

across the patterned substrate. Thus the spheres self-assembly and fill the patterns. The ordering quality and stacking sequence can be controlled by changing the ratio of the particle size to the feature size of the patterned geometry. The efficiency of the assembly process is determined by the gravitational force, the substrate-particle electrostatic interaction, and the capillary forces [193].

2.3.2 Infiltration techniques

Uniform deposition of metal into the interstitial spaces of the colloidal spheres is challenging because the interstitials are constricted and not readily accessible. In addition, colloidal spheres are soft and fragile that can withstand neither mechanical disruption nor the vigorous evolution of gases that often accompany reduction of metal ions. However years of hard work have developed a variety of incorporation techniques such as electrochemical plating, electroless plating, nanoparticle infiltration, precipitation/chemical conversion, which have been successfully applied in the fabrication of metallic inverse opals.

2.3.2.1 Electrochemical plating

Among all these infiltration techniques, electrochemical plating is a relatively simple method with significant advantages. It reduces metals from corresponding electrolytes and the reduction starts from the surface of the conductive substrate usually gold or indium tin oxide coated glass. Then the metal grows outwards to the exposed surface of the template thus fills the entire voids of the template and leads to a volume-templated growth, referring to Figure 2-12(b), which ensures a high filling fraction and a high density so that no shrinkage occurs when the template is removed. The resulting structure is therefore a true cast of the original template and the size of

the spherical voids within the metal is directly determined by the size of template spheres used. Moreover, the metals fill the interstices of the spheres, as well as gaps and cracks in the templates, which makes the original domains jointed, hence enhances mechanical strength of the macroporous frameworks, allowing the processing photonic crystals with large areas. On the other hand, in the surface-template growth process, the precursors penetrate interstials by capillary forces, coating the surface of the colloidal spheres but this may cause pore blockage, resulting in small vacancies in the middle of each triangular intersection of the desired solid, as marked by arrows indicated in the arrow in Figure 2-12(a). For example, it has been reported that macroporous carbon prepared by the sol-gel process contains small voids in the triangular intersections of the carbon walls which could not be completely filled although the pyrolysis time was prolonged and infiltration cycles were repeated [195]. Also, when macroporous titania was fabricated by the liquid-phase chemical reaction with dilute ethanolic solutions of titanium tetrapropoxide and cycles of penetration, reaction and drying were repeated, however, small openings were observed in the middle of each intersections of the titania walls [196].

Additionally electrochemical plating allows precise control over the mass and composition of the deposited material by control of the plating parameters such as the potential or current density and there is no limitation to the thickness of the template that can be filled through. Most deposits are grown as thin films adherent to the conductive surfaces under appropriate conditions, facilitating ready handling of the product solids for the film applications. Also, there is no need of critical conditions such as high temperature or high vacuum etc, or complicated facilities. Due to these advantages, electrochemical plating has been recognized as an efficient and inexpensive technique ideal for industrial applications.

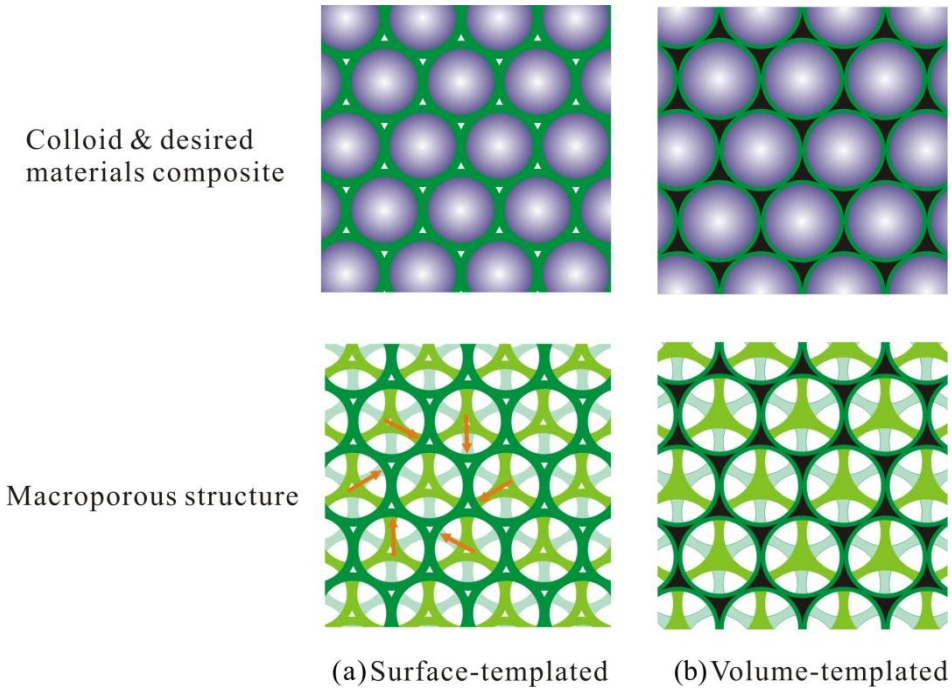

Figure 2-12 Schemes of (a) surface-templated infiltration, which will leave voids (marked by arrows) in the middle of each intersections; (b) volume-templated infiltration resulted a complete filled structure.

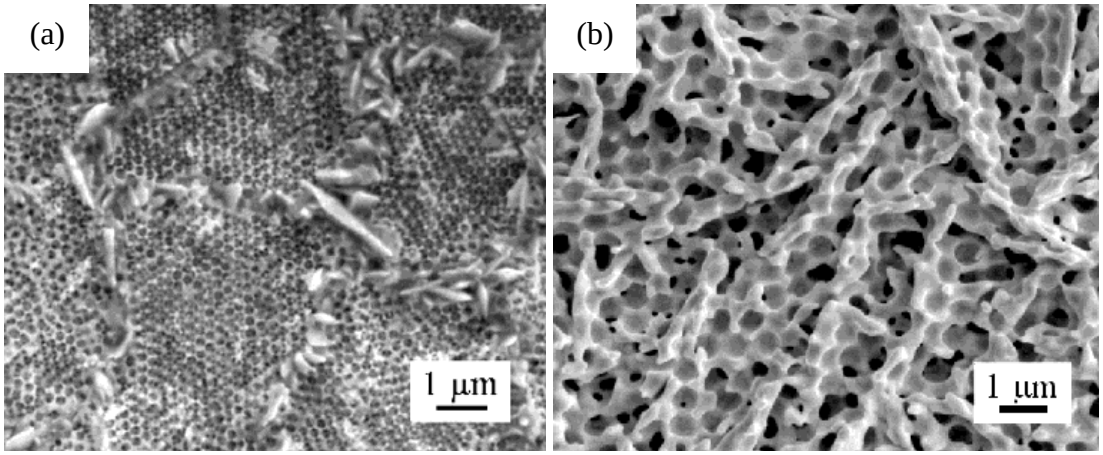

Figure 2-13 SEM images of three-dimensional gold film shown in early work (a) made with a silica template, reveals porous structure with gold flakes between domain boundaries; (b) made with a polystyrene template, demonstrates gold was grown in form of flakes and ordered porous structure within each flake [71].

Noble metals gold, silver and copper are the most interesting candidates for synthesis. In early work, macroporous gold showed uneven nucleation and non-uniform growth with flat flakes growing between domain boundaries and over the top

of the colloidal silica template [71], as shown in Figure 2-13(a). Those templated by polymer spheres showed even worse highly random porous microstructures, as shown in Figure 2-13(b). The authors claimed that dissolving the template in organic solvents led to swelling of the polymer which, in turn, damaged the macroporous metal films. Thus they removed the polystyrene spheres by calcination at 450 ℃.

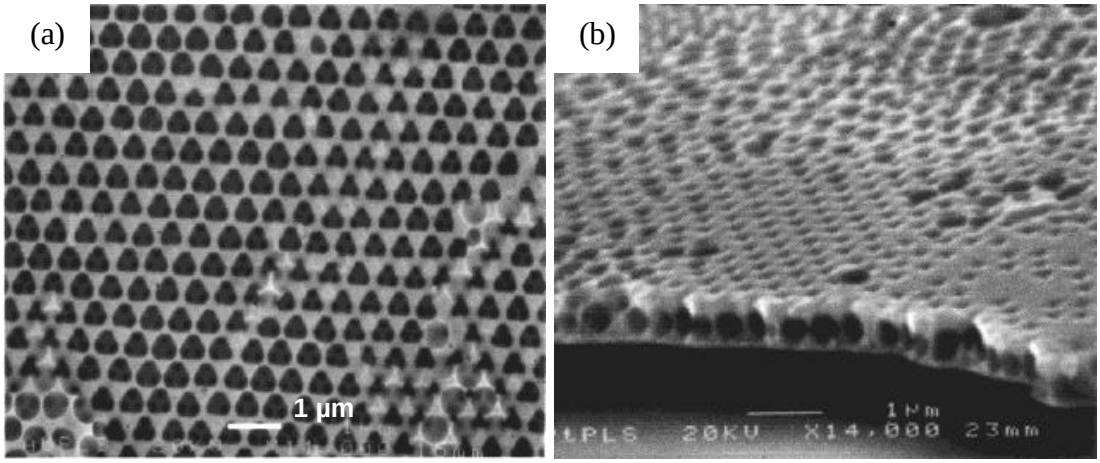

Figure 2-14 SEM images of 3-DOM gold film made with polystyrene templates (a) surface view, reveals ordered spherical voids (b) side view, presents flat smooth surface [70].

It was not until 2002 that well-ordered gold structure consisting of interconnected spherical voids arranged in a metallic framework was first presented, as shown in Figure 2-14 [70]. The interstitial spaces of highly ordered polystyrene spheres were electrochemically infiltrated with gold and subsequently the colloidal template was removed by dissolution in toluene. In contrast to the previous report the authors did not find evidence for disruption of the macroporous metal film caused by polymer swelling in organic solvents. As for 3-DOM silver and copper, there are few reports other than a couple on monolayer structures [73,74] Meanwhile monolayer macroporous platinum and palladium have also been electrochemically prepared [70,73,197]. The metallic frameworks were dense and free from defects, consisting of spherical voids arranged in a highly ordered f.c.c lattice. The void sizes were reported

comparable to the diameter of latex template spheres and the film thickness could be adjusted from tens to hundreds of nanometers. Magnetic metals nickel and cobalt have presented well-ordered macroporous structures [69,197-200]. In addition, it was hypothesized that the current oscillation was related to the changing cross-sectional area of the interstitial voids as the nickel metals grew from the bottom to the top of the template, as shown in Figure 2-15, the coincidence of the total number of the valleys equaled to the average number of the layers of the macroporous nickel.

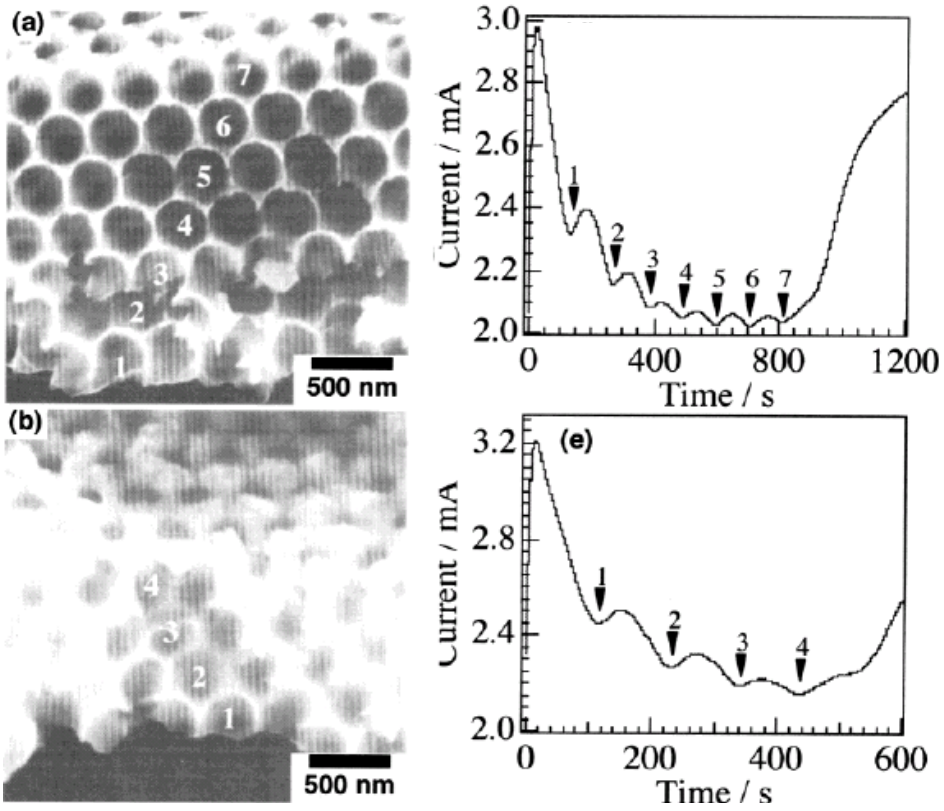

Figure 2-15 SEM images of 3-DOM nickel films made with polystyrene templates and corresponding current - time curves. (a) 7 layers; (b) 4 layers [198].

Other metals including zinc [201], iron [202], ruthenium [203], rhenium [203], osmium [203], have also been reported, as summarized in Table 2-1. In all cases, the spherical voids within the metal films are not isolated, but rather are interconnect by a network of smaller pores. The surface topography of these films is determined by the

blocking effect of template spheres on the growing metal film. However, while the quality of these macroporous films appears reasonable, it should be noted that they are typically only a few sphere layers thick.

Table 2-1: Summary of electrodeposited macroporous metals

Metal	Metal source	Inversion procedure	References
Zn	$Zn(O_2CCH_3)_2$	Oxygen Plasma etching	[201]
Cu	n/a	Ch_2Cl_2 dissolution	[74]
Ag	AgCN	Tetrahydrofunan (THF) dissolution	[73]
Au	$[AuCl_4]^-$	THF or toluene dissolution	[70,73,157]
Ni	Ni^{2+}	Calcination or toluene dissolution	[33,69,198,199]
Pd	$[PdCl_4]^{2-}$	THF or toluene dissolution	[128,197]
Pt	$[PtCl_6]^{2-}$	THF or toluene dissolution	[70,73,128,197]
Co	Co^{2+}/ $Co(O_2CCH_3)_2$	Toluene dissolution	[197,200]
Fe	Fe^{2+}	Toluene dissolution	[202]
Ru	$[Ru(NO)]^{3+}$	n/a	[203]
Os	$[OsCl_6]^{2-}$	n/a	[203]
Re	$[ReO_4]^-$	n/a	[203]

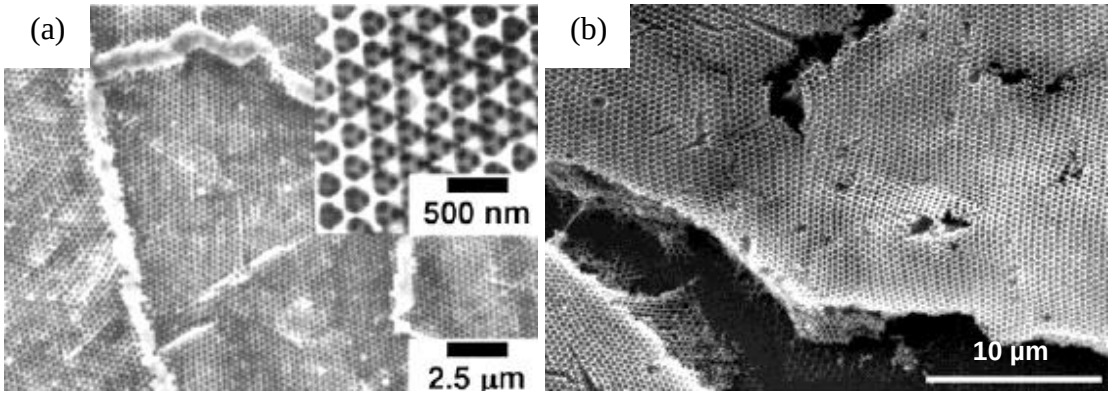

Figure 2-16 SEM images of 3-DOM thin film made from electrochemical plating. (a) cuprous nickel film [198], showing the porous domains are connected by dense solids; (b) zinc film, showing isolated porous domains [201].

One of the main features of the electrochemical plating is that all the interstitial spaces of the template are completely filled, including both the interstices

between the colloidal spheres and cracks between the domains. The surface morphology of the 3-DOM structures will be porous-structured domains connected by a dense metallic network [198,204], as shown in Figure 2-16(a). In contrary, a couple of reports have shown isolated porous domains [201,205], as an example given in Figure 2-16(b), but the authors didn't comment on such a surprising surface morphology.

2.3.2.2 Precipitation/chemical convection

A precipitation/chemical convection process is illustrated in Figure 2-17: a solution of metal acetate in either acetic acid or an ethanol/water mix impregnates the colloidal crystal through capillary forces; subsequently the metal acetate/polystyrene composite is soaked in a solution of oxalic acid for a second impregnation step to precipitate a metal oxalate salt into the voids, building up a pre-arranged inorganic precursor skeleton, which is then chemically converted to the three-dimensional macroporous metal by calcination in flowing nitrogen or hydrogen to prevent oxidation.

Stein *et al.* [206] exploited the preparation of macroporous nickel through the precipitation/chemical convection process. Polystyrene colloidal crystals were soaked in a solution of nickel acetate followed by a saturated solution of oxalic acid to precipitate an insoluble nickel oxalate salt in the interstitial spaces between the latex spheres with diameters ranging from 420 ± 50 nm to 660 ± 30 nm. Subsequent calcinations at 300 ℃ in flowing nitrogen decomposed the nickel oxalate to nickel and carbon dioxide and removed the polystyrene spheres, leaving a nickel macroporous structure with a monodisperse void size ranging from 250 nm to 500 nm. Later they successfully extended this method in fabrications of macroporous

magnetic alloys of Ni_xCo_{1-x} and Mn_3Co_7. For instance, to prepare macroporous Ni_xCo_{1-x} alloy, they impregnated a poly (methyl methacrylate) (PMMA) colloidal crystal with a mixture solution of nickel acetate and cobalt acetate followed by an oxalic acid solution. The metal oxalates were then hydrogen reduced to a macroporous alloy after thermal decomposition of the PMMA template.

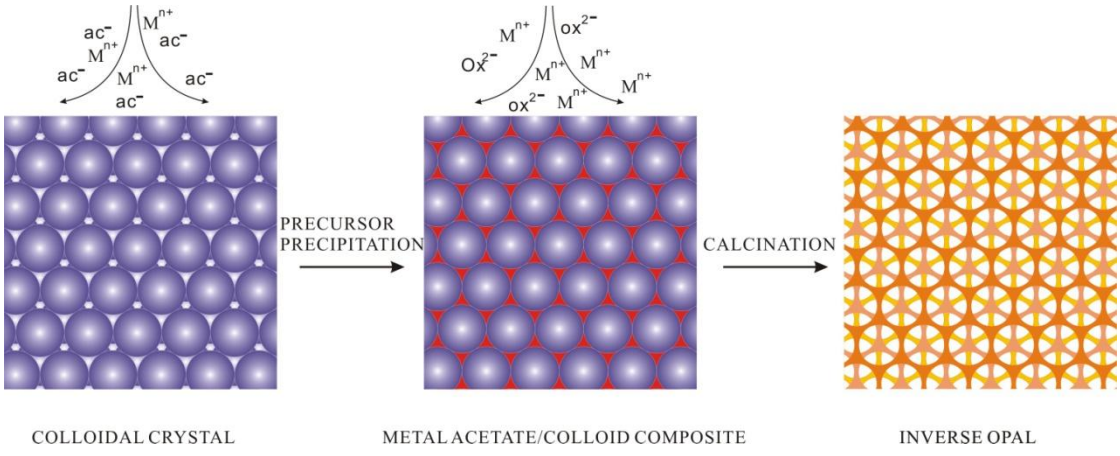

Figure 2-17 Schematic process of precipitation/chemical convection [206].

Although the precipitation/chemical convection method is effective in the fabrication of macroporous metals there are several disadvantages to be noted. Firstly, there is significant shrinkage (up to 50% or even more) and cracking of the structure because the metal precursor salts occupy a greater volume than the final metals. Stein *et al.* reported that an average pore size of 200 nm was obtained with 410 nm PMMA spheres [206]. Secondly, it is limited to metals whose precursor salts are easily reducible and whose melting points exceed the decomposition temperature of the template. Thirdly, it is not suitable to prepare films of controlled thickness.

2.3.2.3 Nanoparticle infiltration

Nanoparticle infiltration is simple one-step deposition process. As illustrated

in Figure 2-18, a glass substrate is placed in a suspension of colloidal metal nanoparticles mixed with sub-micron sized latex spheres. The latex spheres are packed into a crystalline array on the glass substrate through convective self-assembly. Meanwhile the metal nanoparticles aggregate around each polymer sphere. As a result, all void spaces between the latex spheres are filled with the metal nanoparticles, forming a metallic skeleton in the colloidal crystal, which is preserved as a porous nanostructure when the polymer is removed.

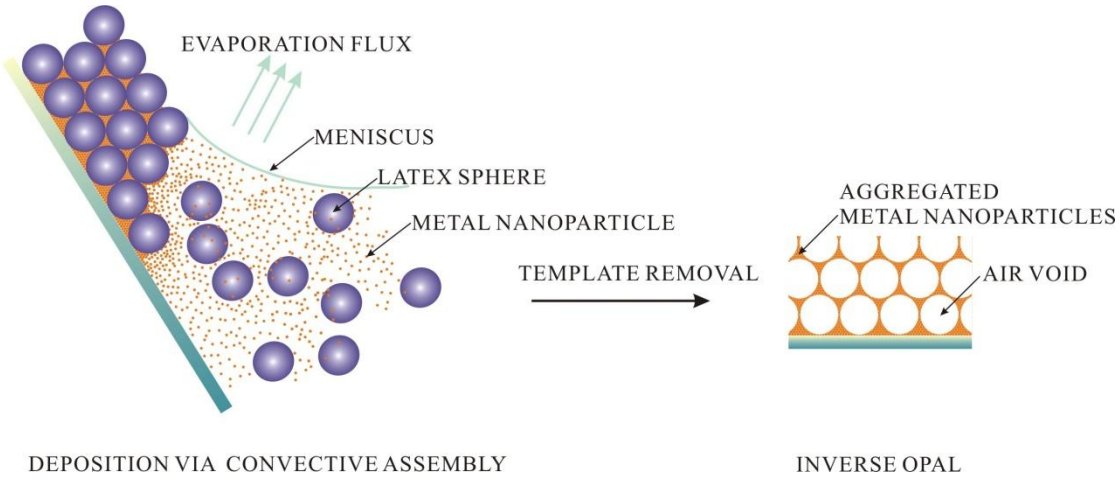

Figure 2-18 Schematic process of nanoparticle infiltration.

Velev *et al.* reported the fabrication of macroporous gold through the nanoparticle infiltration process [121,207]. They created the colloidal crystal from polystyrene spheres with diameters from 200 to 1000 nm and gold nanocrystal (15-25 nm in size) in the interstices of the colloidal spheres. Removal of the polystyrene spheres was accomplished by calcination or chemical means, such as oxidation by concentrated sulphuric acid or dissolution in trichloromethane, yielding macroporous gold. Pore size can be controlled by varying either the size of the nanogold particles (smaller particles yield thicker walls and smaller pores) or the chosen method of template removal (oxidation produces thicker walls than dissolution). This technique

may be adaptable to other nanocrystalline metals.

Though the nanoparticle infiltration method is simple and straightforward, the metal wall exhibited textural mesoporosity. The wall structure depended on the template removal technique. If latex spheres were removed by oxidation with acid or dissolution in chloroform, colloidal gold particles were still discernable in the walls. Calcination could produce a smoother gold structure but resulted in significant shrinkage (up to 30%) [207].

2.3.2.4 Electroless plating

Electroless plating is a simultaneous reduction process in an aqueous solution without external electrical energy supplies. The reaction is driven internally by a chemical reducing agent in solution and is essentially constant at all points of the surface, provided agitation is sufficient to ensure a uniform concentration of metal ions and reducing agents. Electroless deposits are therefore very uniform in thickness all over the part's shape and size.

Many metals including nickel [194,208,209], cobalt [210,211], copper [212], silver [212,213], gold [214] and platinum [215,216] have been produced through this approach. Typically the colloidal spheres modified with thiol surface groups were deposited as close-packed arrays on glass substrates. The colloidal crystal was immersed into a colloidal gold solution. The gold particles were attached to thiol groups and could act as catalysts for the electroless deposition. The composite material was calcined at 575 ℃ for 8 h to strengthen the colloidal crystal and to remove organic residues. It was then immersed in electroless deposition baths to deposit the metal film. Finally the colloidal spheres were removed by dissolution to reveal the porous structure.

In contrast to those samples prepared by precipitation/chemical convection or nanoparticle infiltration, little shrinkage occurred with the deposited metals and the pores were similar in size to the templating spheres. Moreover, electroless plating doesn’t require a continuous conductive path for plating onto - plating can be done straight onto plastics and other substrates regardless the surface of the substrate is conductive or not. However the reduction process is simultaneous but not controllable. Its application is limited by the short lifespan: initial deposition is rapid, process does however slow down after a certain thickness is reached for example, a few hundreds of nanometres for silver, a few microns for copper [212].

3 INSTRUMENTATION

In this chapter, the main experimental techniques used in the project are described. Optical microscope, scanning electron microscope (SEM), optical spectroscopy, surface enhanced Raman spectroscopy (SERS), and X-ray diffraction (XRD) are employed to understand the structural and optical properties of the prepared the 3-DOM thin films.

3.1 Optical microscope

In 1873 German optician Abbe stated that the minimum distance, *d*, that can be distinguished in a specimen was given by [217]

$$d = \frac{0.61\lambda}{n\sin\theta} \qquad \textbf{(3.1)}$$

where λ is the wavelength of the illumination, θ is the half angle subtended by the objective lens at the specimen and *n* is the refractive index of the space between the objective lens and the specimen. The minimum distance, *d*, is the theoretical resolution limit of microscopes.

Usually, the refractive index is well below 2 and the maximum value for $sin\theta = 1$, consequently the resolution that can be achieved by a microscope using visible light (λ = 550 nm is assumed, corresponding to green light) is limited to 200 nm.

The optical microscope is used in this work to characterize the surface topography of samples, providing an initial evaluation of the quality of the samples. As examples given in Figure 3-1, polystyrene films were prepared with increasing

colloidal volume fractions from (a) to (d), but with all other conditions the same. When the concentration of the colloidal suspension was very low, the resultant film was quite non-uniform, as illustrated in Figure 3-1(a), in which the different color represents the different film thickness. With the increasing of the colloidal concentration, the surface of the films has become more uniform, and the domain size was enlarging as well. However, when the concentration was too high (in practice, thick films are normally fabricated by successive coatings [186] instead of simply increasing the volume fraction to get higher thickness), the film started to delaminate, referring to Figure 3-1(d).

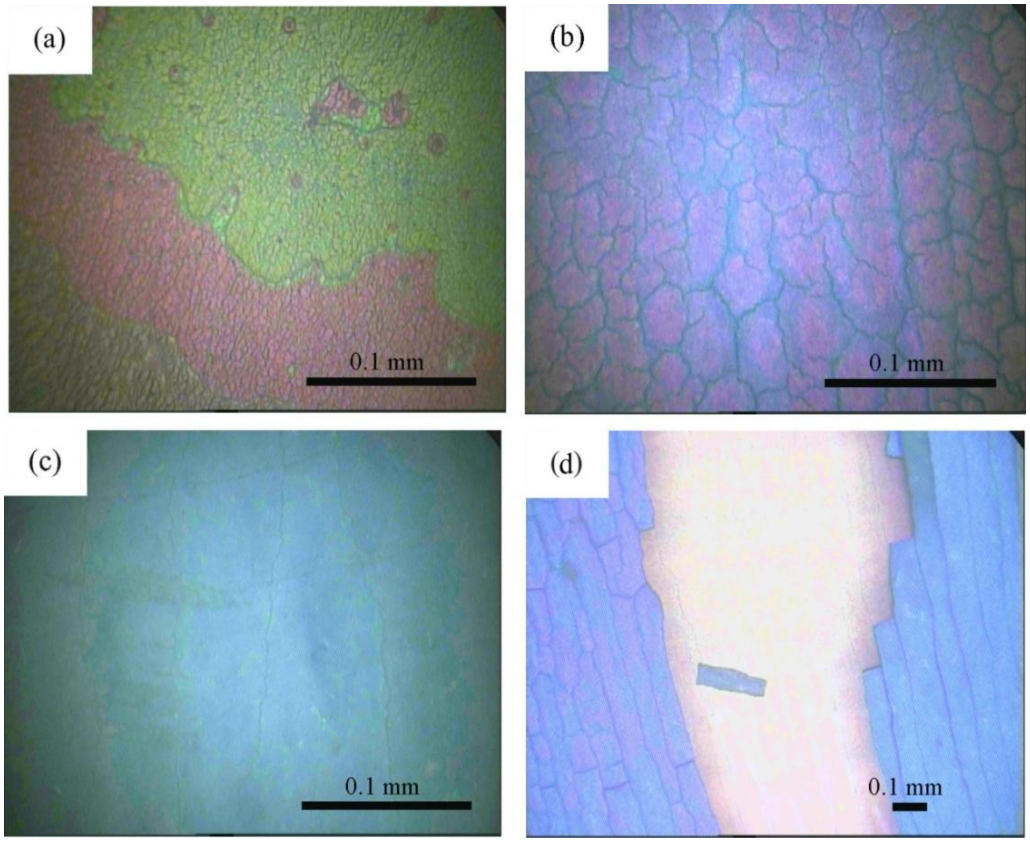

Figure 3-1 Optical microscope images of polystyrene films with increasing film thickness from (a) to (d).

3.2 Scanning electron microscope

3.2.1 Basic principles of SEM

As stated in Equation 3.1, the resolution of a microscope, *d*, is restricted by the wavelength of illustration of microscopes. While de Broglie related that the wavelength of an electron, λ, is inversely proportional to the momentum, *p*, by the following equation [218]:

$$\lambda = \frac{h}{p} \tag{3.2}$$

where *h* is the Planck's constant and the value is $6.6 \times 10^{-34}\ J\ Hz^{-1}$.

In the electron microscope, the electrons of charge *e*, are accelerated by potential *U*, the kinetic energy of the electrons can be found as,

$$eU = \frac{1}{2}mv^2 \tag{3.3}$$

where *m* is the rest mass and the value is $9.1 \times 10^{-28}\ g$. and *v* is the velocity of the electron respectively.

Hence

$$\lambda = \frac{h}{\sqrt{2meU}} \tag{3.4}$$

For instance, the wavelength of the electron is 0.0049 nm when the accelerating voltage is 60 kV. Consequently the scanning electron microscope (SEM) has been developed and uses accelerated electrons that have much shorter de Broglie wavelength than that of photons to form an image, resulting in a high spatial resolution. According to Equation 3.1, SEM is capable of examining features down to nanometre scales whilst optical microscopes can only reach ~ 0.2 mm in practice.

The essential components of an SEM are schematically illustrated in Figure 3-

2. The electrons are emitted by either a thermionic cathode made of a tungsten filament or Lanthanum Hexaboride (LaB_6) single crystal or a field emission gun made of a pointed tungsten tip. The beam of electrons is accelerated by an anode at a voltage up to 100 keV with respect to the cathode and condensed to a fine electron probe by using a set of magnetic lenses, scanning over a specimen in a two-dimensional raster. Interaction between the incident beam of electrons and electrons in the specimen generates various signals, most commonly are secondary electrons, backscattered electrons, or characteristic x-rays. The signals are detected, amplified, and mapped onto a cathode-ray-tube (CRT) display for observation.

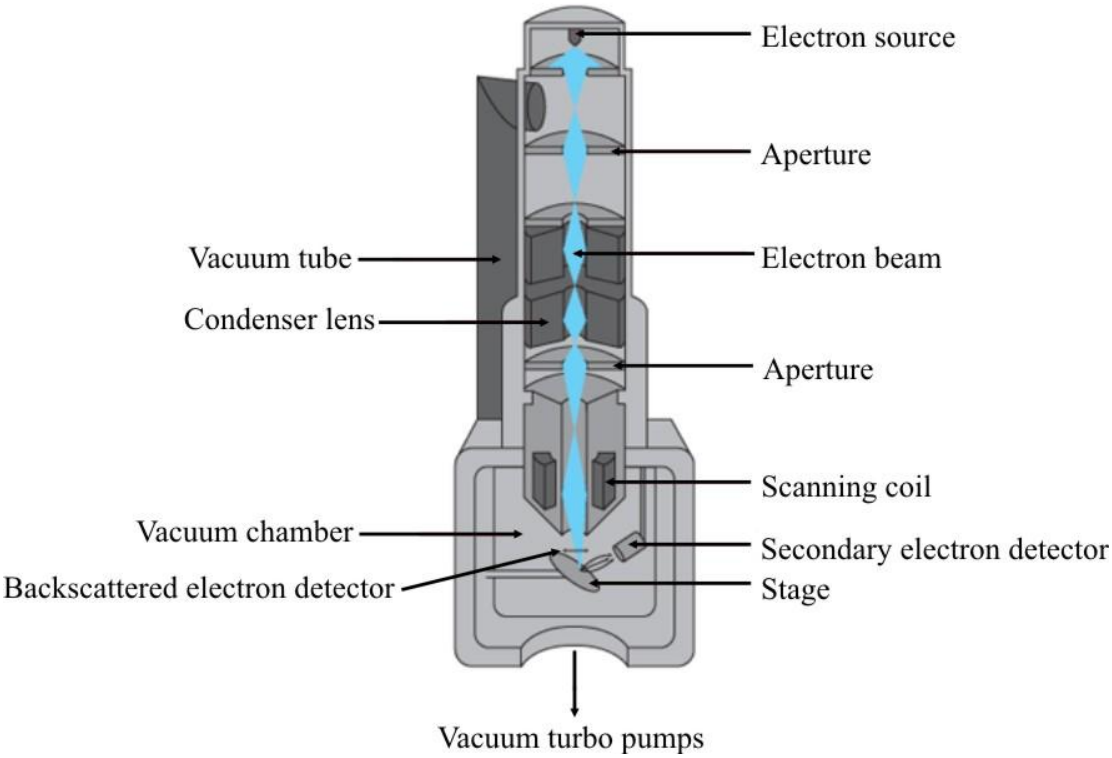

Figure 3-2 Schematic diagram of a scanning electron microscope.

3.2.2 Image mechanisms of SEM

Elastic and inelastic scattering are the elemental interactions between atoms. Figure 3-3 shows the most important interaction processes and their information

volumes. Secondary electrons arise due to inelastic collisions between the incident electrons and electrons bound in the specimen. If energy transferred to the specimen electrons is sufficient to overcome the work function that binds them to the solid, they are ejected as secondary electrons. Incident electrons may interact with the nucleus of atoms in the specimen and be reflected back out of the specimen as backscattered electrons. The rate for energy loss is very low so that most of the secondary electrons typically have energy between 5 to 10 eV [219]. 50 eV is a conventional cut-off value, below which they are said to be secondary electrons and all of the escaped electrons with energy above 50 eV are called backscattered electrons. Auger electron production is an alternative to characteristic X-ray emission after ionization of an inner shell. The de-excitation energy released when an electron from an upper shell fills the vacancy in the ionized shell can be converted to an X-ray quantum of energy $h\upsilon = E_2 - E_1$ or the energy may be transferred to another atomic electron, which leaves the specimen as an Auger electron.

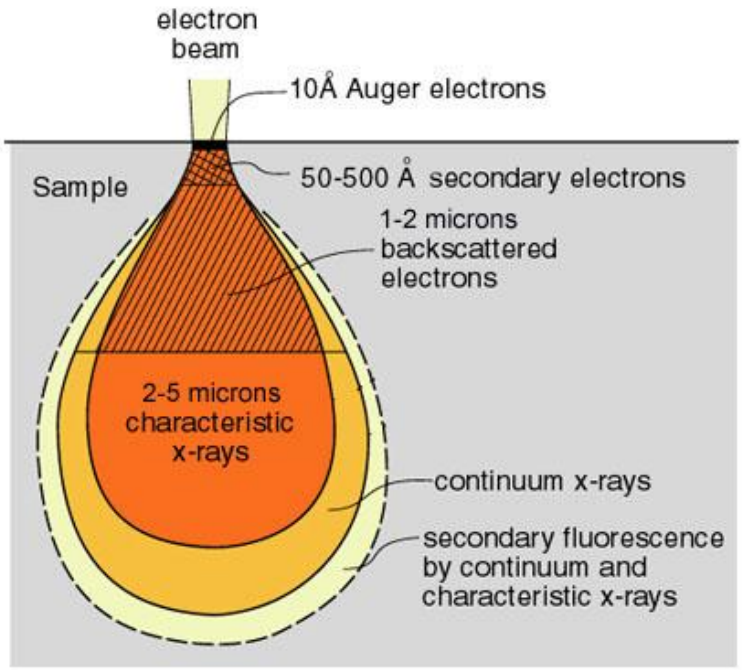

Figure 3-3 Generalized illustration of interaction volumes.

3.2.2.1 Secondary electrons (SE)

Due to the low energy of the secondary electrons, only those excited a few nanometres in depth to the surface can be detected [220], as illustrated in Figure 3-3. This allows a resolution as high as 1-10 nm. The secondary electrons are used to image the surface topography. In general, areas that have more secondary electrons collected by the detector will appear brighter than those have fewer electrons detected. For example, certain areas are not reachable for the incident beam and no secondary electrons will be generated. They thus appear dark in the images. Some areas such as area A in Figure 3-4 are able to generate secondary electrons, however, they face away to the detector and fewer electrons will be collected and then they will appear less bright. The dependence of the secondary electrons generation on the tilt angle of a surface element, the enhanced emission at edges and small particles and the shadow contrast that results from incomplete collection can all contribute to the image contrast.

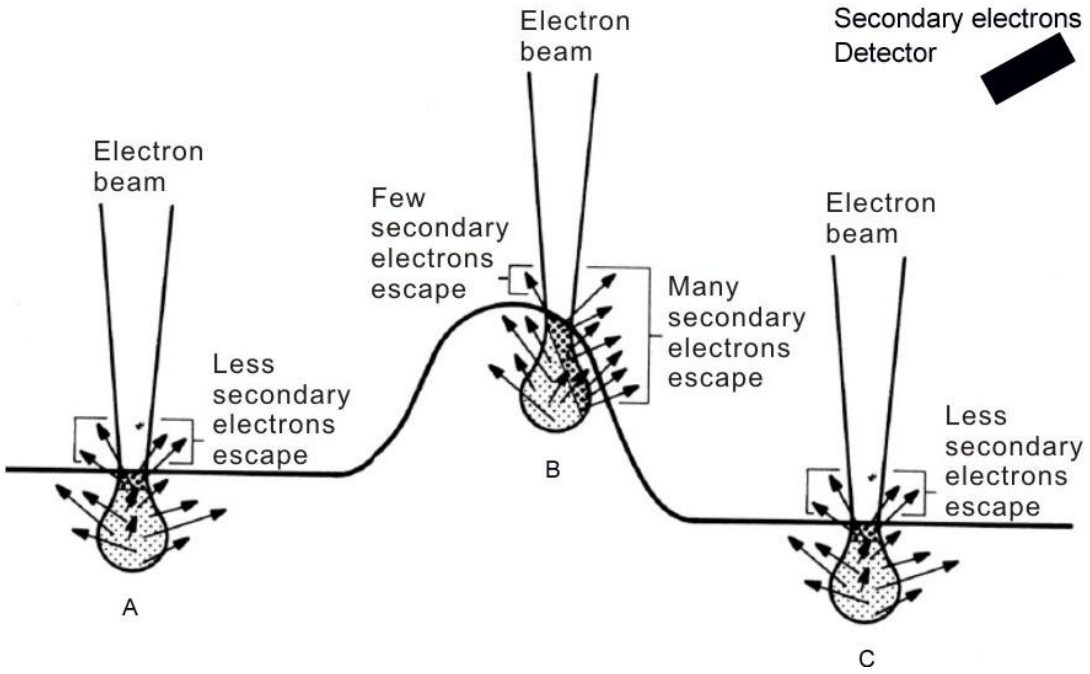

Figure 3-4 Schematic diagram of secondary electron generation.

In this thesis, microstructural features of interest include sphere or pore size, domain size/shape, volume fractions, and defects such as cracks or stacking faults. The information is obtained primarily from secondary electron images. An example of a polystyrene film is shown in Figure 3-5. The top surface is close packed polystyrene spheres with each sphere having six neighbour spheres, corresponding to either a (111) plane of a face centred cubic or a (0001) plane of a hexagonal close packed structure. The dark area is a drying crack where the secondary electrons are not detectable. Defects such as voids are randomly distributed and stacking faults are running perpendicular to the drying crack.

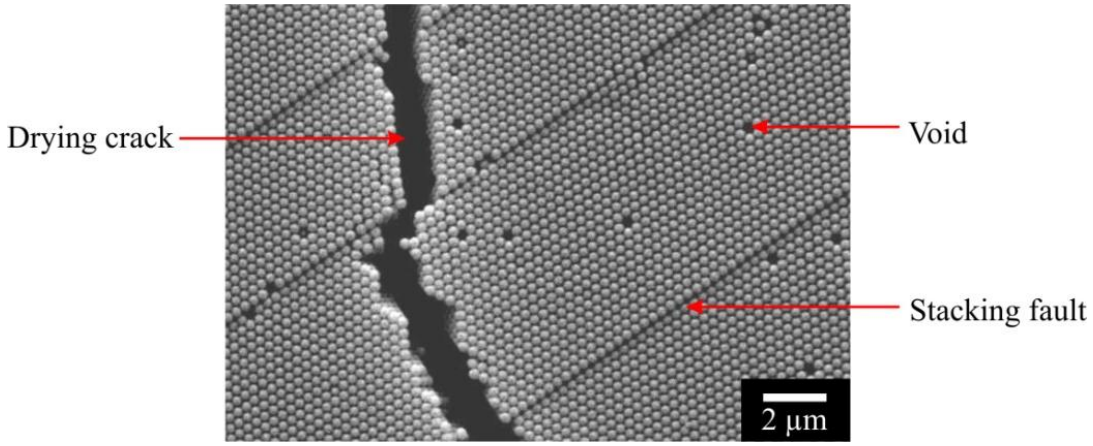

Figure 3-5 SEM surface view of a polystyrene film obtained in present work.

3.2.2.2 Backscattered electrons (BSE)

Backscattered electrons, as mentioned earlier, are elastic scattered electrons that have nearly the same energy levels as the incident beam electrons. Unlike secondary electrons, the backscattered electrons would not be affected by electrostatic collection field and travel in a straight path that is almost the same direction as the one they come from so that the backscattered electron detector is placed below the objective. Since the quantity of electrons backscattered is proportional to the atomic

number, the backscattered electrons are to illustrate chemical contrast of the specimen - the higher atomic number area, the brighter it appears. However, the resolution of backscattered electron images is not as good as that of the secondary electron images because the signals come from a depth of up to half of the electron penetration depth, referring to Figure 3-3. The backscattered electron is also angle dependent and a weak topographical contrast is superimposed on the chemical contrast. Generally the backscattered electron images are better suited for smooth specimen surfaces to avoid excessive surface roughness interfering with the discrimination of the specimen.

3.2.2.3 Characteristic X-rays

When electrons of the specimen atom are ejected as the secondary electrons, electrons from outer shells drop into the inner shells to replace the vacancies. As illustrated in Figure 3-6(a), a K shell electron is kicked out by the incident electron. This leaves a vacancy in the K shell. To keep the energy of the atom the lowest, an electron from outer shell e.g. L shell falls into the vacancy. The difference of the energy between the K and L shells will be emitted as x-rays. The wavelength of the x-rays is characteristic of, not only the elements, but also the element shells that have lost and gained electrons. However, the energy difference can be absorbed by a outer shell electron, as illustrated in Figure 3-6(b), an electron in the M shell accepts the energy and leaves the atomic orbit. Such an electron is called Auger electron and this process is competitive to X-ray emission.

An SEM may be equipped with an energy dispersive X-ray (EDX) analysis system in which a detector collects the characteristic x-rays and separates them according to the energy. The window of the detector is usually made of beryllium so that X-rays from all elements in the periodic table above beryllium (atomic number =

4), if present sufficient quantity, can be presented in spectral forms. The main advantages of EDX are its speed of data collection and the ease of use. In this thesis, EDX analysis is distinctive in identifying the elements of the specimen or contaminants, as well as estimating their relative concentrations.

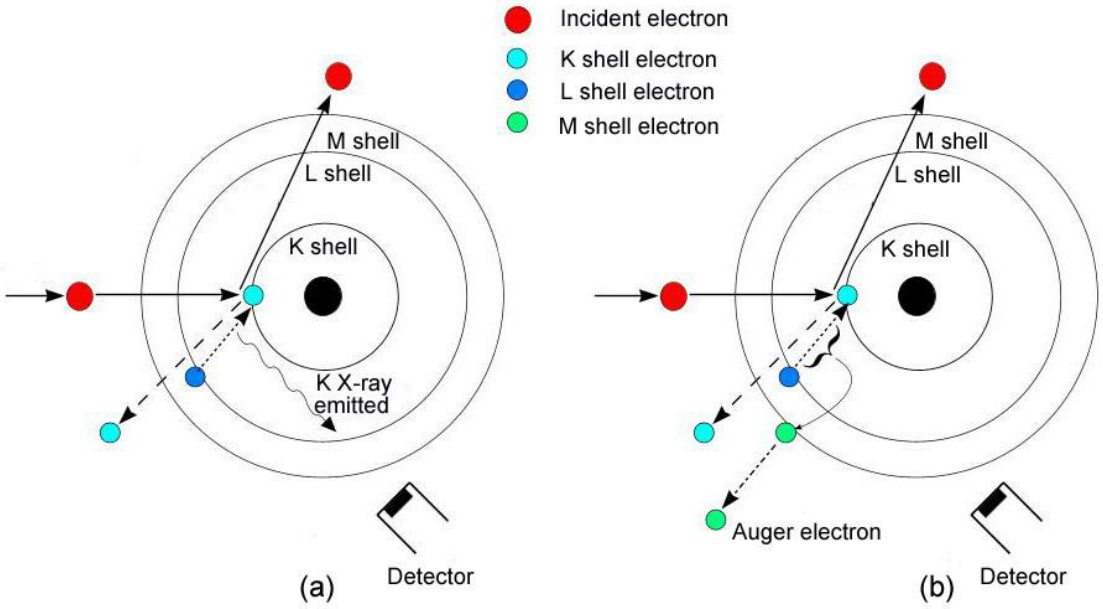

Figure 3-6 Classical models showing the production of (a) characteristic X-rays and Auger electrons

3.3 Reflectance spectroscopy

In this thesis, reflectance spectroscopy was employed to investigate the stop band properties of photonic crystals. As stated in Section 2.1.1, when the incident radiation satisfies the Bragg condition, it will not able to propagate through the sample and the radiation is detected as a peak in the reflectance spectra.

3.3.1 Instrumental setup

The experimental setup for measuring angle resolved reflectivity spectra was a Bentham 200 Series optical bench which consists of a white light source - 100W

quartz halogen lamp, a triple grating monochromator (TM 300V series) and a set of focusing lenses, a goniometer and a silicon photodiode detector, schematically shown in Figure 3-7. The light passes through the monochromator to obtain a beam with a fixed wavelength in the range between 300 and 1100 nm. The monochromic light is focused on a sample in a spot with 1.0 mm in diameter. The sample is mounted on a goniometer, which is capable of moving from $0\,^{\circ}$ to $75\,^{\circ}$ so that incident light at various angles can be measured. The reflected light is collected by a detector and amplified and finally the intensity is recorded as a function of incident wavelength by the computer.

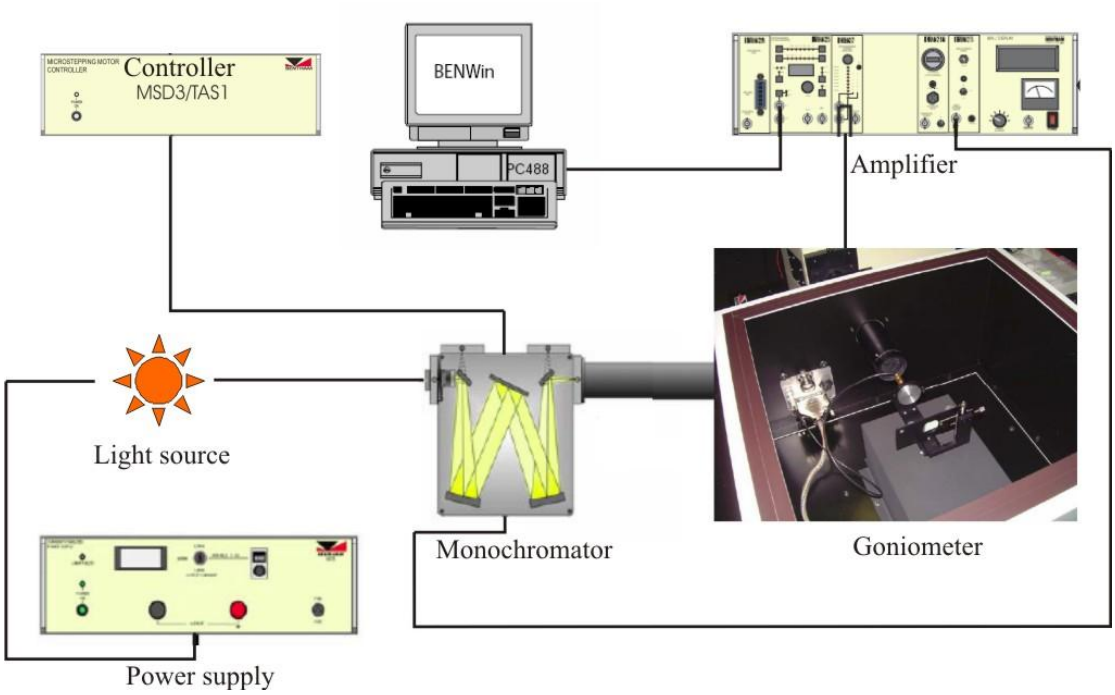

Figure 3-7 Schematic setup for measuring angle-resolved reflectivity, adapted from BENTHAM 200 series user handbook.

3.3.2 Spectral analysis

A typical series of angle resolved reflectance spectra of the polystyrene thin film is shown in Figure 3-8. The reflection peaks are Bragg refraction from

consecutive (111) planes [173] and they shift to higher frequency with increasing angle of incidence.

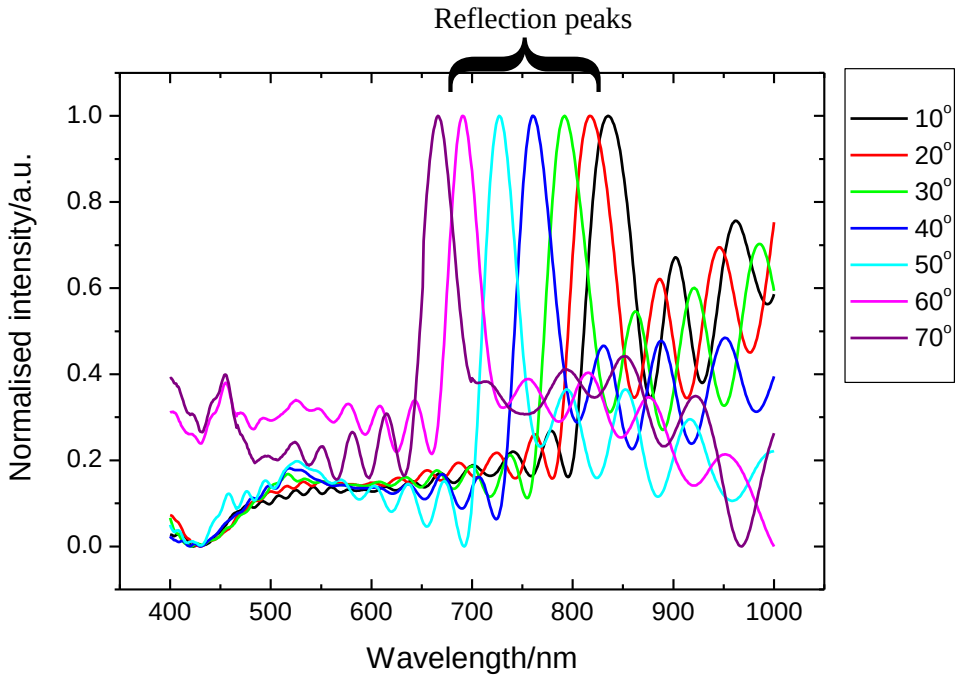

Figure 3-8 Angle-resolved reflectance spectra of polystyrene film.

An approximate calculation for the diameter of the polystyrene spheres can be obtained from the combining Bragg's law and Snell's law to obtain [221,222]

$$\lambda = 2d_{hkl}\sqrt{n_{eff}^2 - \sin^2\theta} \tag{3.5}$$

where d_{hkl} is the lattice constant or the distance between two diffracting (hkl) planes for the sample, θ is the angle of the incident to the normal surface, λ is the peak wavelength, and n_{eff} is the effective refractive index of the structure.

Ploting $sin^2\theta$ vs λ^2 gives a straight line with intercept (b) and gradient (m),

$$b = n_{eff}^2 ; m = -\frac{1}{4d_{hkl}^2} \tag{3.6}$$

Therefore n_{eff} and d_{111} can be obtained with

$$n_{eff} = \sqrt{b}; d_{hkl} = \sqrt{-\frac{1}{4m}} \quad \textbf{(3.7)}$$

As for a face-centered cubic structure

$$D = \sqrt{\frac{3}{2}} d_{hkl} \quad \textbf{(3.8)}$$

where D is the diameter of polystyrene spheres. In the case of the reflectance spectra shown in Figure 3-8, the fitting value of for n_{eff} and sphere diameter D were determined to be 1.54 and 334 nm respectively.

Thin films display some characteristics that cannot be observed on thick opals. The interference of light reflected by the top and bottom surfaces causes the well-known Fabry-Perot fringes. Though such interferences exist in all films, the interferences of thick opals form a continuous background and only in thin films can the oscillations be clearly observed. As shown in Figure 3-9, the Fabry-Perot fringes can be seen on both sides of the Bragg peak and they can therefore be used as a non-destructive measure for the film thickness (t). According to [223]

$$t = \frac{r}{2\sqrt{n_{eff}^2 - \sin^2\theta}} \left(\frac{1}{\lambda_{r+1}} - \frac{1}{\lambda_1}\right)^{-1} + \delta \quad \textbf{(3.9)}$$

where n_{eff} is the effective refractive index of the structure, θ is the angle of the incident to the normal surface, r is the Fabry-Perot fringe order ($r = 1,2\ 3,4,\ ....$), λ_r is the wavelength of the r^{th} fringe, δ is the phase change upon reflection (a constant that can be ignored in most cases).

Plotting r vs. $2\sqrt{n_{eff}^2 - \sin^2\theta}\left(\frac{\lambda_1 - \lambda_{r+1}}{\lambda_1 \lambda_{r+1}}\right)$ produces a straight line of film thickness as gradient. An example is given in Figure 3-9. From the information of FP fringes (marked with red arrows in the inserted picture in Figure 3-9) of the reflectance spectrum obtained from the incident angle of 10 °, the thickness of the film

is calculated to be 4.68 ±0.35 μm, corresponds to 14 sphere layers.

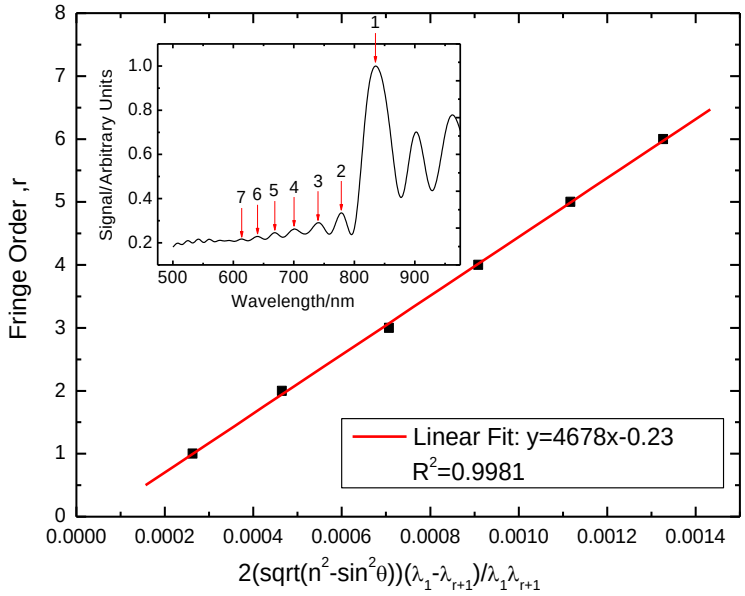

Figure 3-9 Linear fit to determine the thickness of the film from Fabry-Perot fringes obtained at 10 °incident angle (inset), in which numbers 1 to 7 are the orders of the fringes.

3.4 Surface enhanced Raman spectroscopy

Metallic macroporous structures have been used as stable surface enhanced Raman spectroscopy (SERS) substrates whilst the void geometry and uniform surface are proposed to give reliable Plasmon signals. In the project SERS was measured using a Renishaw 2000 CCD Raman spectrometer equipped with Olympus BH-2 confocal microscope, as schematically illustrated in Figure 3-10. The system is equipped with a 633 nm Helium-Neon (HeNe) and a 514 nm Argon ion (Ar^+) lasers with a maximum power of 2.8 mW. The specimen surfaces were found to be highly sensitive to the intensity of the incident laser. As a result, low power levels (i.e. 0.5 mW at the focal point) were used for all measurements to avoid laser damage to the surface. Spectra were collected using the extended scanning mode from 200 to 3200 cm^{-1} and 10 s accumulation time, with the single scan over the desired range taking

one minute to collect from recording normal SERS spectra.

The lasers are aligned along the same optical path, allowing different lasers to focus on the same point with ease. Light is focused on the specimen with the confocal microscope. There is a selection of objective lenses available, including 5×, 20×, and 50× long working distance objectives and 20×, 50× and 100× high numerical aperture short working distance objectives, and a 60× immersion objective index matched to water. Most commonly we used either 50× (providing a spot of < 1 μm in diameter) near working distance or the immersion objective lens for dry or aqueous samples, respectively

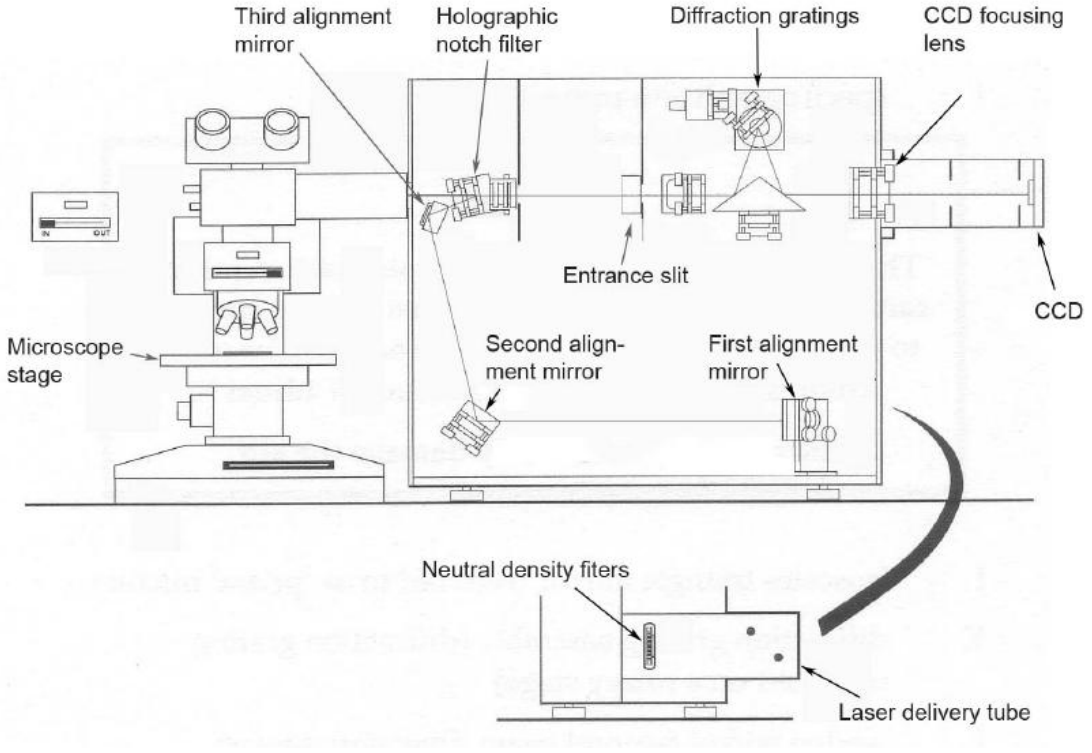

Figure 3-10 Schematic layout of Renishaw 2000 CCD Raman spectrometer with Olympus BH-2 confocal microscope, adapted from the Ranishaw manual.

SERS active molecules are provided by dyes rhodamine 6G (R6G) and benzotriazole (BZT). R6G adsorbs to the surface through physical adsorption, which

results in a weak binding. Hence if there is something strongly bound to the surface then little or no adsorption will occur. The benzotriazole dye has been designed to bind through strong covalent binding to metal surfaces specifically for use for SERS applications. The binding is essentially irreversible and the dye should displace any surface species bound to the surface ensuring a good Raman signal.

3.5 X-ray Diffraction

X-ray diffraction (XRD) has been in use for the fingerprint characterization of crystalline materials and the determination of their structure. According to Bragg's law stated in Section 2.1.1, when a monochromatic beam of X-rays with wavelength λ strike a sample at an angle θ, diffraction occurs only when the distance d traveled by the rays reflected from successive planes differs by a complete number n of wavelengths: $2dsin\theta = n\lambda$.

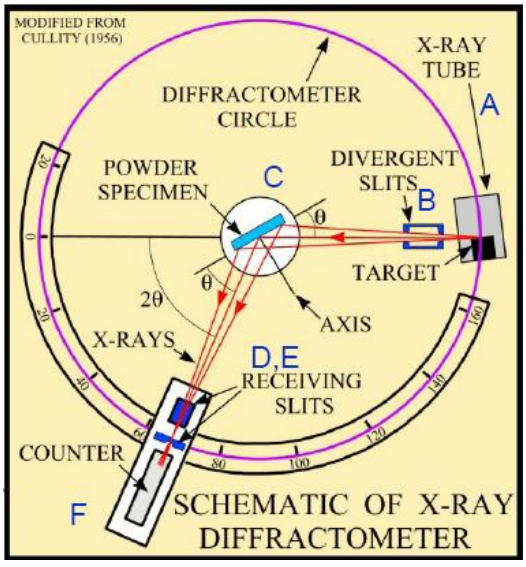

Figure 3-11 Schematic construction of X-ray diffractometer. A. X-ray source; B. focusing slit; C. specimen stage; D. receiving slits; E. monochrometer or filter; and F. X-ray detector.

The construction of an X-ray diffractometer is shown in Figure 3-11. It

basically consists of three parts – an X-ray source, a specimen, and an X-ray detector. The angle between the plan of the specimen and the X-ray source is θ, the Bragg angle. The angle between the projection of the x-ray source and the detector is 2θ. The detector moves through a range of angles, typically from 0 ° to about 160 °. By rotating the specimen around a central axis, a diffraction beam can be generated if the sample is correctly oriented at the Bragg diffraction angle. The diffracted beam is then passed through a set of collimation slits to remove X-ray scattering and then counted by the detector. Both the positional and intensity data are collected, which enables the phase composition of the sample to be determined when the recorded pattern is matched with standard patterns.

4 SYNTHESIS OF COLLOIDAL TEMPLATES

This chapter is to demonstrate the synthesis of large area colloidal crystals on conductive substrates. Either silica or polymer spheres can be used to make the colloidal crystals. Both of them are both highly wettable by the precursors of the framework and available with less than 5% variability in monodispersity. However, polymer spheres were chosen for the project because they are readily removable at room temperature by toluene or tetrahydrofuran (THF) without affecting the deposited metallic replica.

4.1 Synthesis of colloidal spheres

Sub-micron sized polystyrene spheres with a narrow size distribution (polydispersity < 5% being desirable [224,225]) were synthesized by emulsion polymerization of monomers, in which hydrophobic monomers are dispersed in a continuous phase and polymerised to form large molecules [226-229]. Styrene ($C_6H_5CH=CH_2$, 99%, Aldrich) was used as the monomer and potassium persulfate (($K_2S_2O_8$, 99%, reagent grade, Aldrich) was the reaction initiator, which is a molecule capable of forming reactive free radicals. The styrene was washed thoroughly with deionised water before use to remove traces of reaction inhibitor 4-tert-butylcatechol ($C_{10}H_{14}O_2$).

The polymerisation procedure consists of three steps: initiation, propagation, and termination, as illustrated in Figure 4-1. During the initiation phase, the potassium persulfate was thermally decomposed at 70 - 80 ℃ to generate two free radicals to be

added to the double bond of the styrene monomer. Once initiated, successive additions of styrene monomer to the free radical end of the polymer chain causes the chain to grow. The consumption of a free radical is accompanied by the formation of a new, large free radical. The polymerisation is terminated by steps that consume, but do not form, free radicals, such as the combination of two free radicals [228].

(a) Initiation

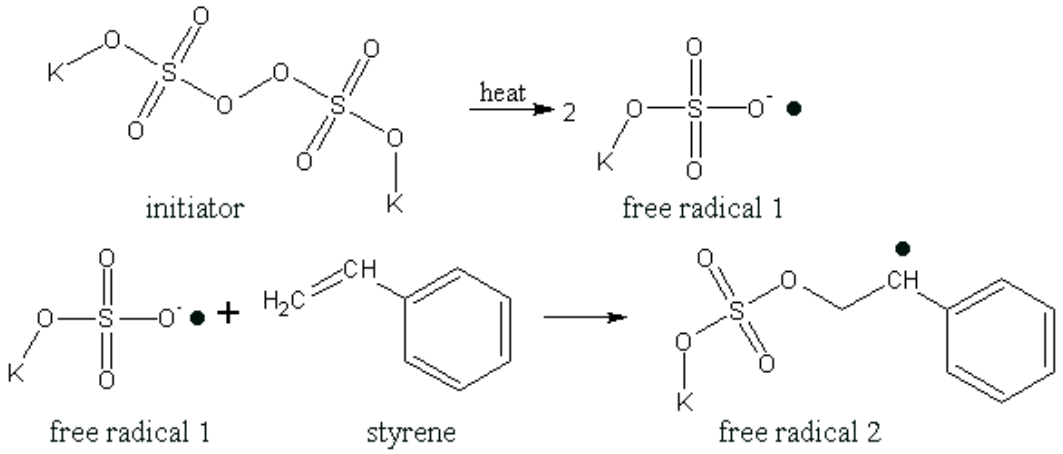

(b) Propagation

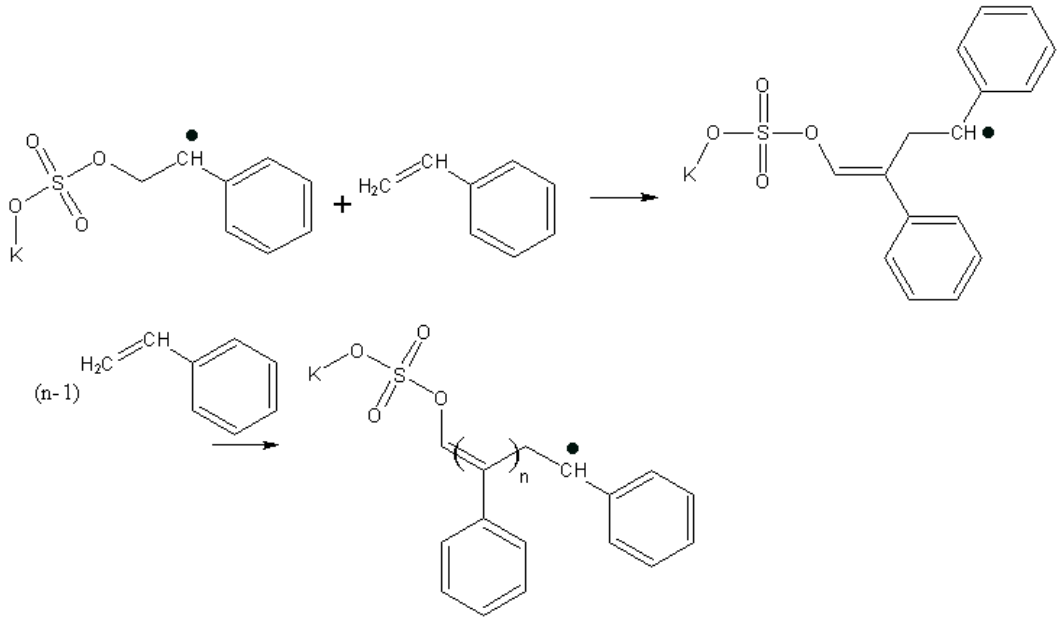

(c) Termination

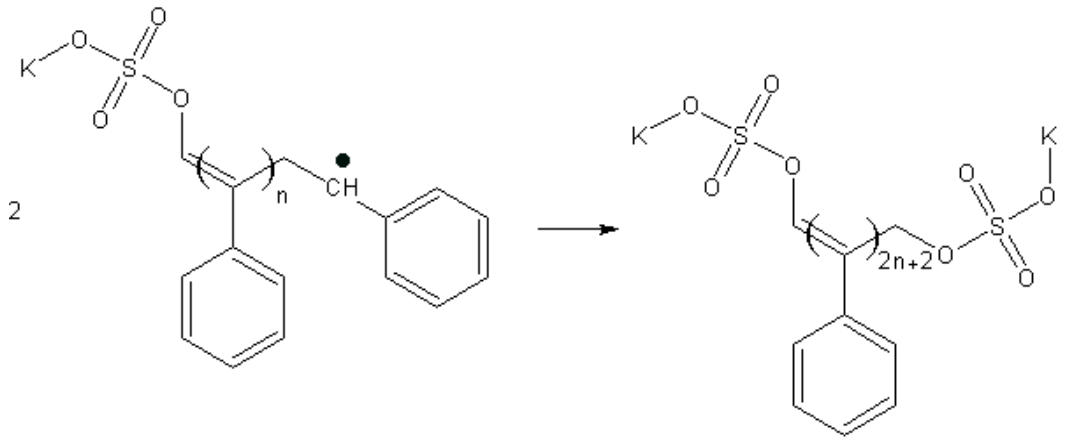

Figure 4-1 Emulsion polymerisation process of styrene using potassium persulfate as initiator to produce polystyrene.

Variations in the mean diameter of the spheres can be achieved in several ways which include, alternating the reagent concentration, varying the stirrer speed, and increasing the reaction temperature and time of the reaction [6,227]. To obtain a monodisperse size distribution, the stirrer speed and the temperature should be kept constant throughout the synthesis process to maintain a uniform rate of reaction. The polystyrene dispersion should also be filtered through glass fibre and filter paper to remove large aggregates and stabilised in an aqueous suspension.

The particle size decreases proportionally with initiator concentration, stirring speed and reaction temperature but increases with monomer concentration. A large number of radicals will be formed at the early stage of the reaction, producing surface active oligomers which colloidally stabilize the particles and thus provide numerous nuclei. In our work, the concentration of the styrene was varied while other conditions, including the synthesis temperature, stirrer speed and concentration of the potassium persulfate, were kept constant and the emulsion solution was agitated at 70 ℃ at 350 r/min for 24 hours under nitrogen atmosphere to obtain various mean particle

diameters ranging between 200 nm and 700 nm.

The particle sizes were measured using a transmission electron microscope (TEM), with 200 the minimum number of spheres measured. Table 4-1 shows three representative sizes of the polystyrene spheres used in the thesis. They are 651 ± 23.4 nm, 327 ± 6.0 nm, and 248 ± 5.7 nm, all corresponding to polydispersity of less than 4%. Typical TEM images of the polystyrene spheres of mean diameter of 327 ± 6.0 nm are shown in Figure 4-2.

Table 4-1: Sizes of the polystyrene spheres used in the project

Sphere diameter/nm	Standard deviation/nm	Polydispersity/%
651	23.4	3.6
327	6.0	1.8
248	5.7	2.3

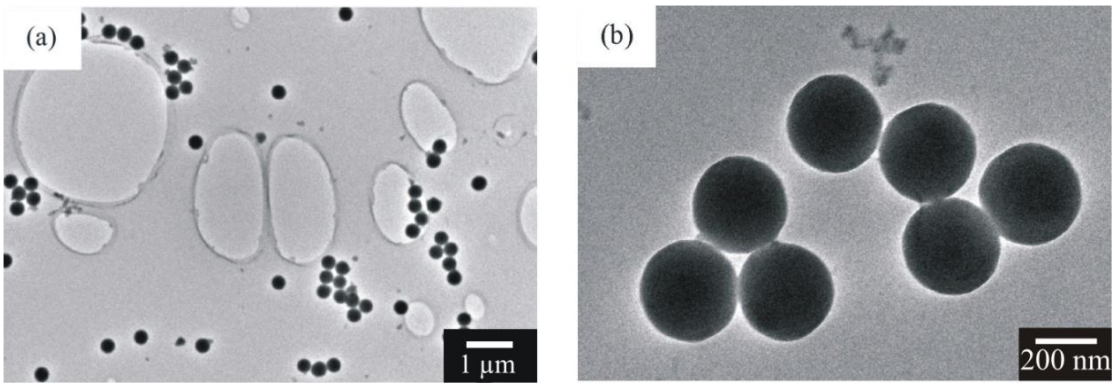

Figure 4-2 TEM images of colloidal spheres of mean diameter of 327 ± 6.0 nm.

4.2 Experimental

4.2.1 Materials

Substrate cleaning: Indium Tin oxide (ITO) coated glass slides (Delta Technologies, Resistances = 8-12 ohms/cm) of dimensions 50 mm × 12.5 mm × 0.7

mm were used as substrates for the polystyrene (PS) template growth. The substrates were washed sequentially with OptiClear detergent (National Diagnostics), acetone (BDH AnalaR©, 99%), methanol (BDH AnalaR©, 99.8%), and deionised water. All solvents were of reagent quality and used as received. In each solvent, slides were placed in an ultrasonic bath for 15 minutes. When the clean cycle was completed, the substrates were blow-dried with nitrogen.

Suspension preparation: monodisperse polystyrene colloids of diameters 248 ± 5.7 nm, 327 ± 6.0 nm, and 651 ± 23.4 nm were sonicated for at least 10 minutes before use to break all aggregates and diluted to volume fractions of 0.01%, 0.05%, 0.10%, 0.30%, 0.50%, or 1.00% with deionised water. A small amount (0.02%) of detergent Tween-20 was added to the diluted suspension to reduce the surface tension on ITO glass slides.

4.2.2 Procedure

The polystyrene templates were grown through evaporation induced convective self-assembly, which produces highly ordered particle arrays with smooth surfaces as well as controllable film thickness, as stated in Section 4.2.3. The procedure is schematically shown in Figure 4-6. A clean and flat ITO glass substrate is placed in an aqueous suspension of polystyrene spheres, with a certain volume fraction. The key parameters that affect the quality of polystyrene crystals are the evaporation temperature and relative humidity (RH). Based on the experience in our group the polystyrene films assembled on bare microslides have the best quality when they were grown using colloid suspensions with volume fractions in the range of 0.07 - 1.4% at the evaporation temperature of 65 ℃ and a relative humidity not more than 20% [6,230]. As it was ITO coated glass substrates used in the thesis, from trial and

error, the conditions have been modified to the evaporation temperature of 60 ℃ and a relative humidity of 20 - 30%. The vials were kept in an incubator where the temperature is controlled with a precision of ±0.2 ℃ for 48 hours until all the liquid has been evaporated.

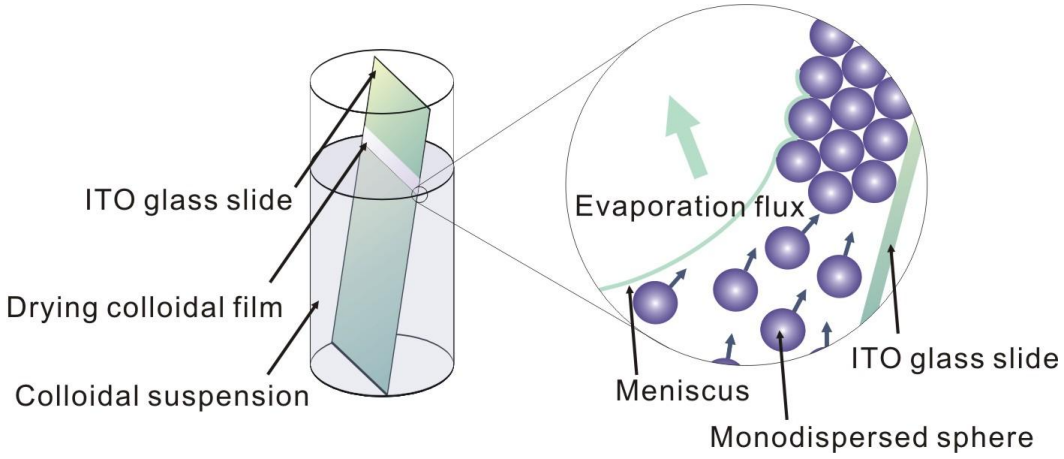

Figure 4-3 Schematic process of growing polystyrene colloidal crystals through evaporation induced self-assembly.

4.3 Results and discussions

4.3.1 Crystalline control

As soon as the vial is placed into the incubator, liquid evaporates and particle assembly starts. However it may take a while before the growth reaches an equilibrium. In the initial growth stage, monolayer has been formed but the number of layers is increasing for the time being, as shown in Figure 4-4(a), in which various colours are attribute to thickness difference. Within a very short period, the evaporation flux has become constant and the film grows continuously and uniformly. Figure 4-4(b) and (c) give the uniform middle area in a large scale. However, since the evaporation is competitive with the gravity, the suspension is concentrated when the growth reaches the bottom of the substrate slide. More particles settle down at the

bottom area, especially when the slide is titled. Once again the decrease of the uniformity is revealed by the non-uniform colours in Figure 4-4(d). Hereafter only the middle area where the film growth is balanced and suffer less gravity interruption, is used for the further investigation.

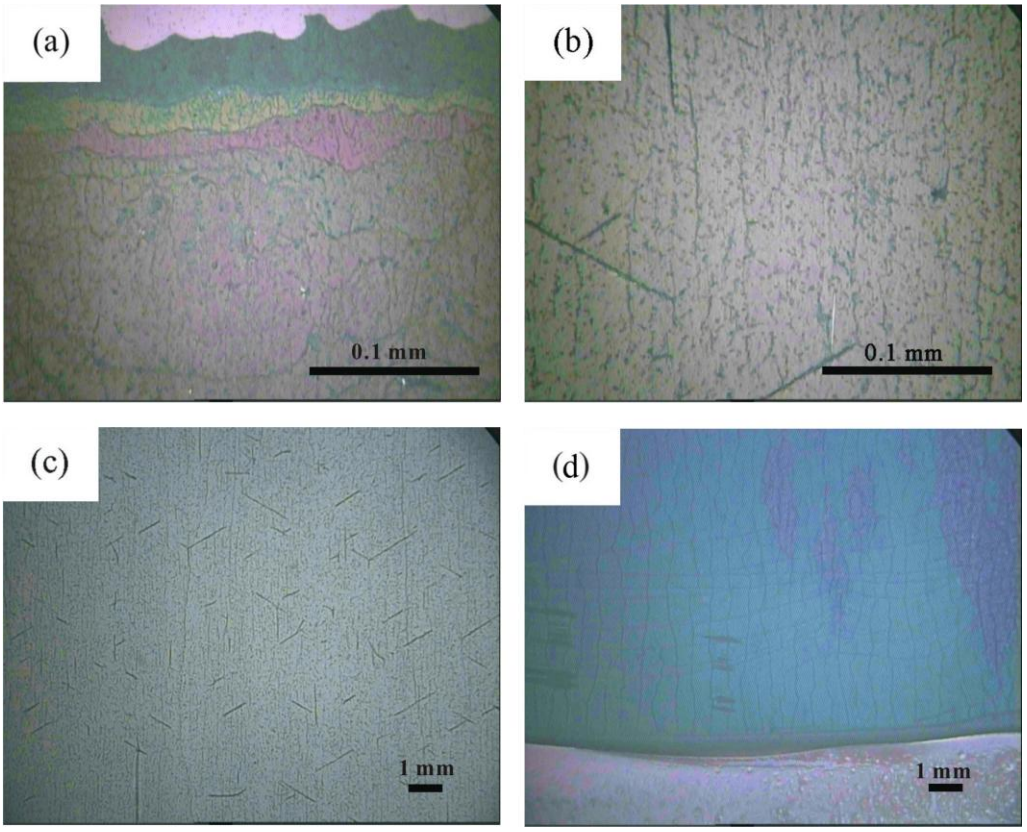

Figure 4-4 Optical microscopy images of polystyrene film (a) layered up top area; (b) uniform middle area of high magnification ×50; (c) middle area remain uniform in low magnification ×10; (d) less uniform bottom area.

Crystallinity is one of the most important parameters in determining the performance of colloidal crystals. The crystallinity can be modified by changing the substrate, polydispersity, temperature, and relative humidity.

4.3.1.1 Substrate materials

To produce dense-packed latex particle arrays through convective self-

assembly, the substrate must be hydrophilic so that the suspension and particles are able to slide on the substrate before the film dries. Otherwise the array growth may form a discontinuous film with stripes. For instance the surface tension of ITO coated glass slides is higher than that of clear microslides and stripes of polystyrene crystals thus formed on the ITO slide, as shown in Figure 4-5(a) & (b), if the same conditions are used. To solve this problem and obtain continuous film, a small amount (0.02%) of detergent Tween 20 was added to wet the surface of ITO glass slides, as illustrated in Figure 4-5(c) & (d).

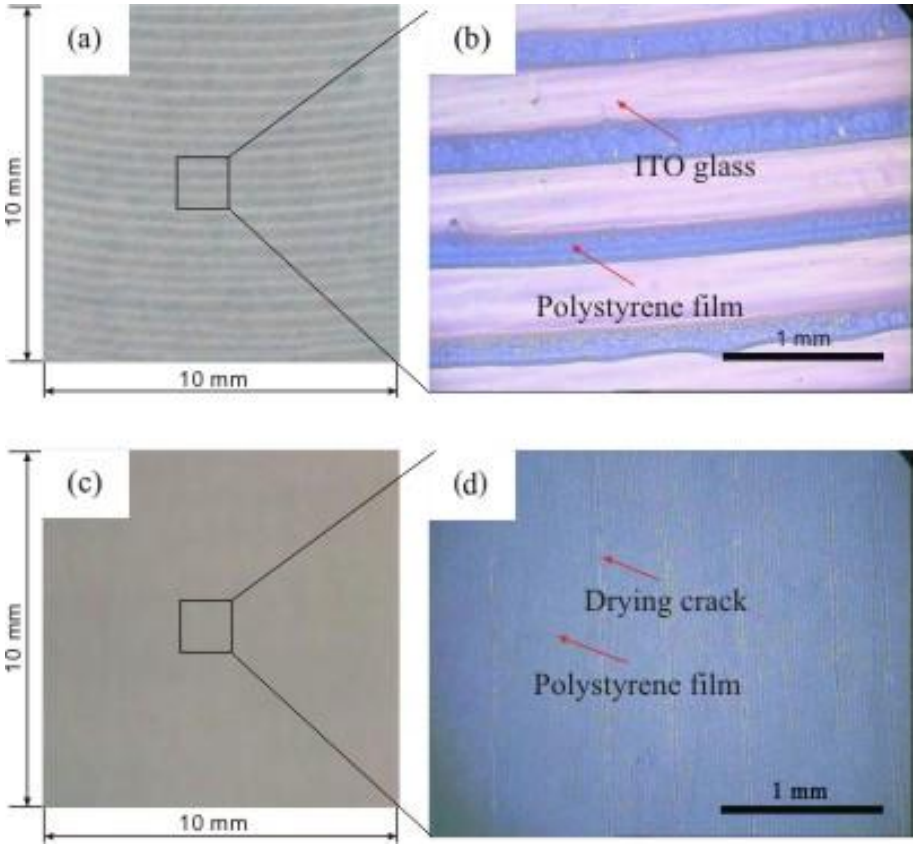

Figure 4-5 (a) high surface tension resulted in 'stripes' on the glass substrate; (c) hydrophilic surface produced continues dense packed colloidal film; (b) and (d) optical microscopy images of corresponding enlarged areas.

In addition, substrate surface cleaning would affect the film quality as well. The organic contaminations or other foreign substances might disturb surface

properties such as surface tension, orientation, or surface charge, which in return degrade the adhesion between the polystyrene particle and the substrate. Figure 4-6 clearly indicates that the film quality is significantly affected by cleaning treatment of the surface substrate.

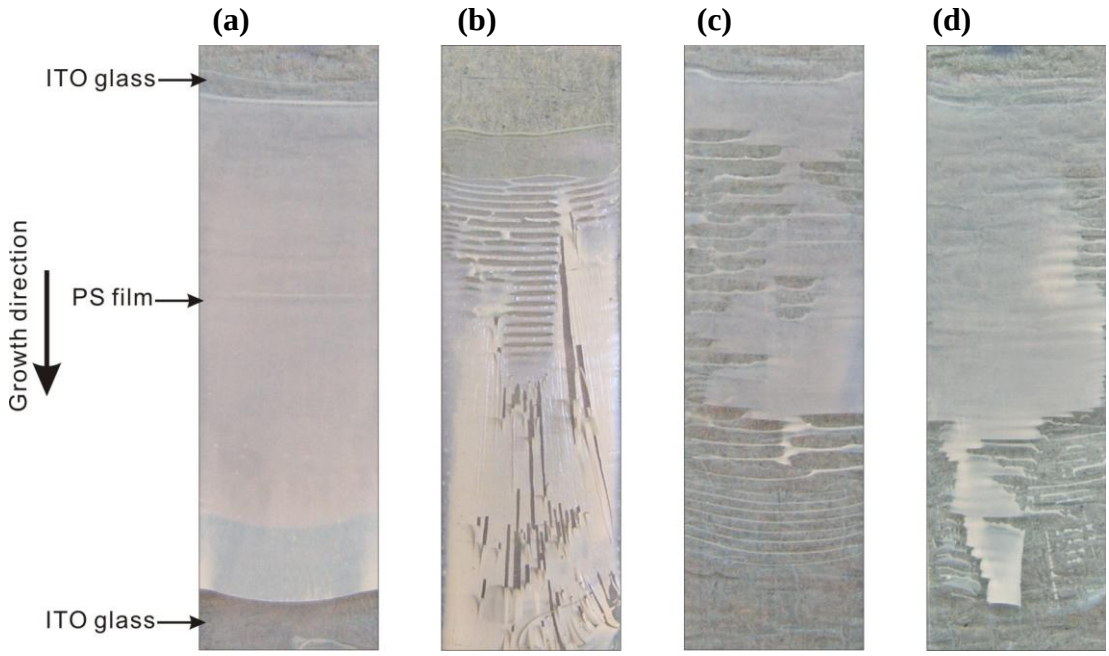

Figure 4-6 Digital photography images of polystyrene films on ITO glass substrates (a) proper cleaned surface gives uniform growth; (b) - (d) surface suffering contamination and result in delaminated or non-uniform films. Film growth directions are from top to the bottom, as indicated by arrows.

4.3.1.2 Polydispersity of colloidal spheres

Another crucial parameter affecting the crystallinity is the polydispersity (size distribution) of the colloidal spheres. Figure 4-7 shows SEM images of two polystyrene films grown from colloidal spheres of sphere comparable diameters 651 nm and 565 nm with polydispersity of 9.4% and 3.6% respectively spontaneously in the same incubator. Fast Fourier transforms (FFTs) are two-dimensional spatial frequency diagrams that can be considered as surface diffraction patterns. The FFT images shown in the insets of Figure 4-7(b) and (d) were obtained from low

magnification images of 40 × 40 μm^2 in area of the two films with the polydispersity of 9.4% and 3.6%, respectively. The inset of Figure 4-7(d) obtained from narrower size distribution exhibits sharp spots in the FFTs, showing a high degree of regularity over a large length scale. While the polydisperse sample has only short-range order and the Fourier transforms will therefore look like the diffraction pattern of a polycrystal - a series of concentric rings resulting from many spots very close together at various orientations around the centre beam spot [128,186], as shown in the inset of Figure 4-7(b).

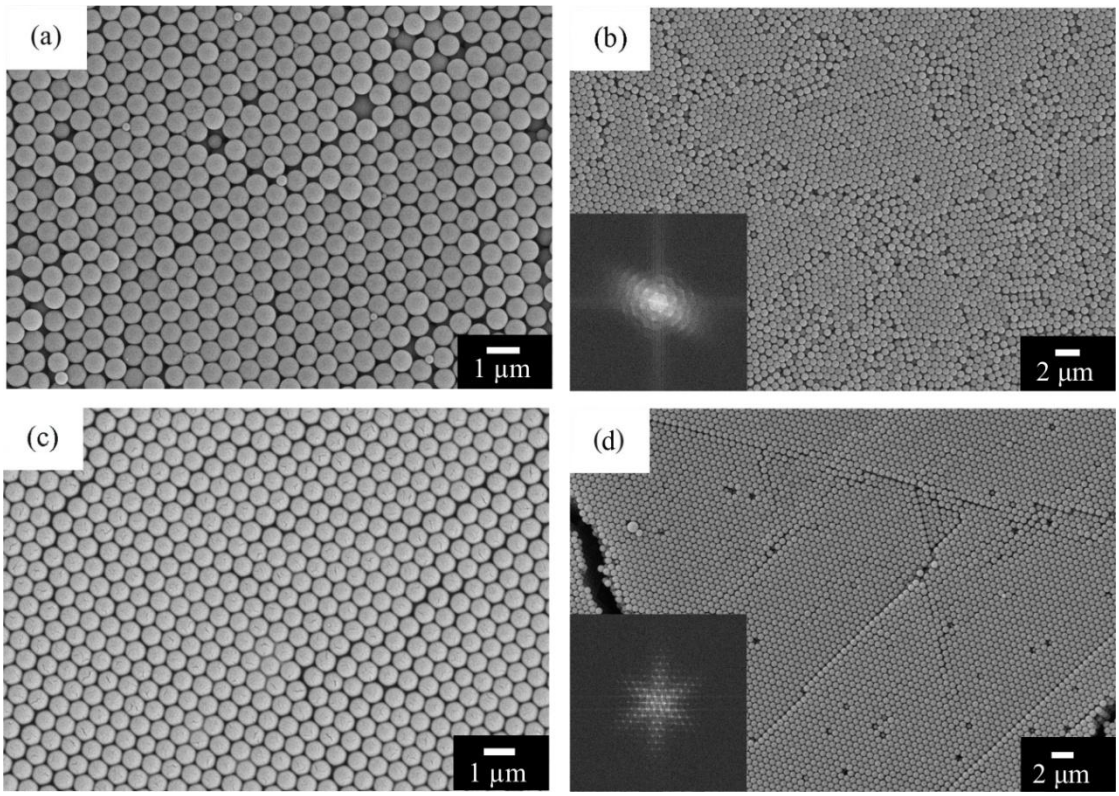

Figure 4-7 SEM images of the polystyrene films grown from colloids of comparable sizes but with polydispersities of (a) & (b) 9.4% and (c) & (d) 3.6%.

4.3.1.3 Growth temperature and relative humidity

The Gibbs free energy difference between f.c.c and h.c.p phases is only 0.005 RT/mol [231,232]. The energy difference increases with the evaporation temperature.

Thus an increase of the evaporation temperature leads the colloidal crystal an increased tendency towards equilibrium f.c.c phase [46]. Figure 4-8 shows a few SEM surface images of colloidal crystals prepared at evaporation temperatures of 50 ℃, 60 ℃ and 70 ℃ respectively. All samples exhibit ordered close-packed arrangement of polystyrene spheres, but the crystalline quality strongly depends on the evaporation temperature. As the convective self-assembly must compete with sedimentation, when using a low temperature, the growth rate is low and the spheres settle down to where before the meniscus arrive, which leads to more defects. Sample (a) grown at 50 ℃ have more defects such as vacancies and plane stacking faults than sample (b) grown at 60 ℃. Since at 60 ℃ the polystyrene spheres have more kinetic energy to explore possible lattice sites and the resulting film shows fewer defects. For sample (c) grown at even higher temperature 70 ℃ the most visible types of cracks and plane staking faults as the water evaporation rate exceeds the crystal growth rate, the meniscus moves more quickly and the liquid dries before the spheres organize themselves into close-packed arrangements. In addition, faster evaporation rate also increases drying tension in thin films and results in more drying cracks [233,234].

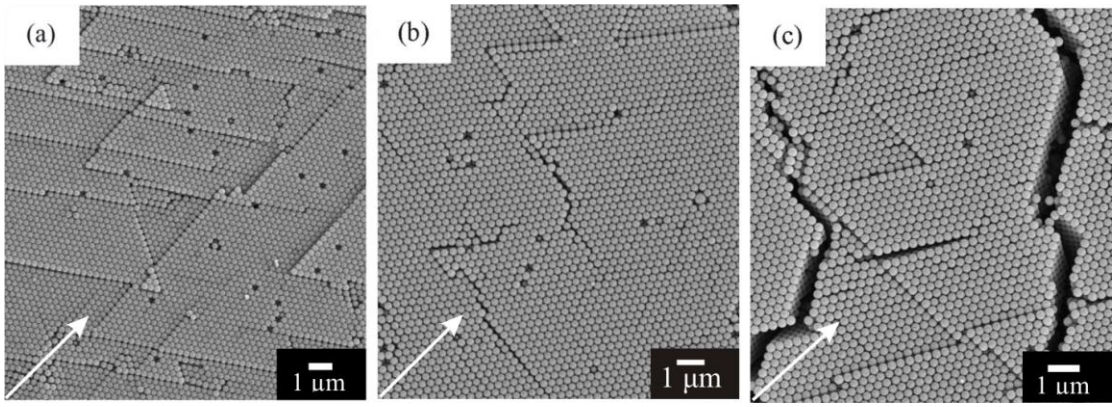

Figure 4-8 SEM surface images of colloidal crystals (sphere diameter of 327 ± 6.0 nm) prepared at evaporation temperatures of (a) 50 ℃, (b) 60 ℃, and (c) 70 ℃. Growth directions are represented by arrows.

Figure 4-8 demonstrates that for the growth of colloidal crystals of good crystalline quality, the compromise between a higher evaporation temperature and a slower crystal growth rate is important, the sample fabricated at a higher temperature has the tendency to have fewer defects, but will lead to a disordered state if the rate of particle transport is higher than that for crystallization or nucleus formation

Relative humidity plays a similar role in crystalline quality. A lower relative humidity corresponds to a larger lateral capillary force, which leads to the presence of more inner cracks in the colloidal crystal. Again, a lower relative humidity promotes a higher array growth rate, bringing additional internal stress and results in more drying cracks. Figure 4-9(a) shows an image of cracks of the polystyrene films grown at 60 ℃ but with a relative humidity around only 10%. Such cracks were largely reduced when the relative humidity increased to 30%, as shown in Figure 4-9(b). However, if the relative humidity is over high, the array growth rate will be too slow and the formed array may suffer more defects. For the colloidal particle sizes used in the thesis, the relative humidity was controlled between 20 - 30%.

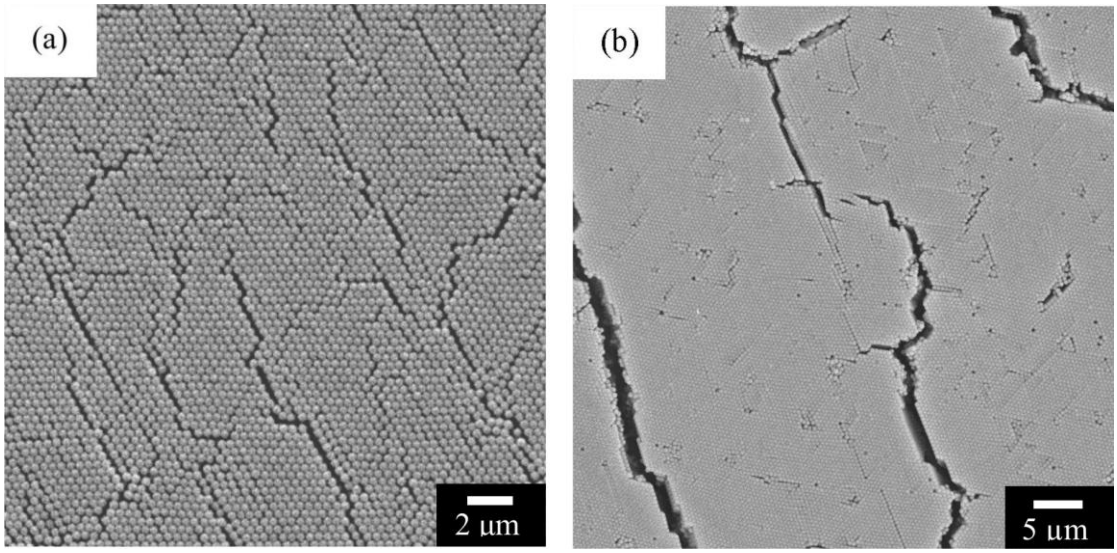

Figure 4-9 Cracks in the polystyrene films grown at 60 ℃ but with relative humidity of (a) 10% and (b) 30%.

4.3.1.4 Volume fraction of the suspension

The volume fraction controls the particle flux and therefore the film thickness. As examples given in Figure 4-10(a) to (f), polystyrene films were prepared from spheres of 651 ± 23.4 nm in diameter and with increasing colloidal volume fractions from 0.01%, 0.05%, 0.10%, 0.30%, 0.50%, to 1.00% respectively, but with all other conditions the same.

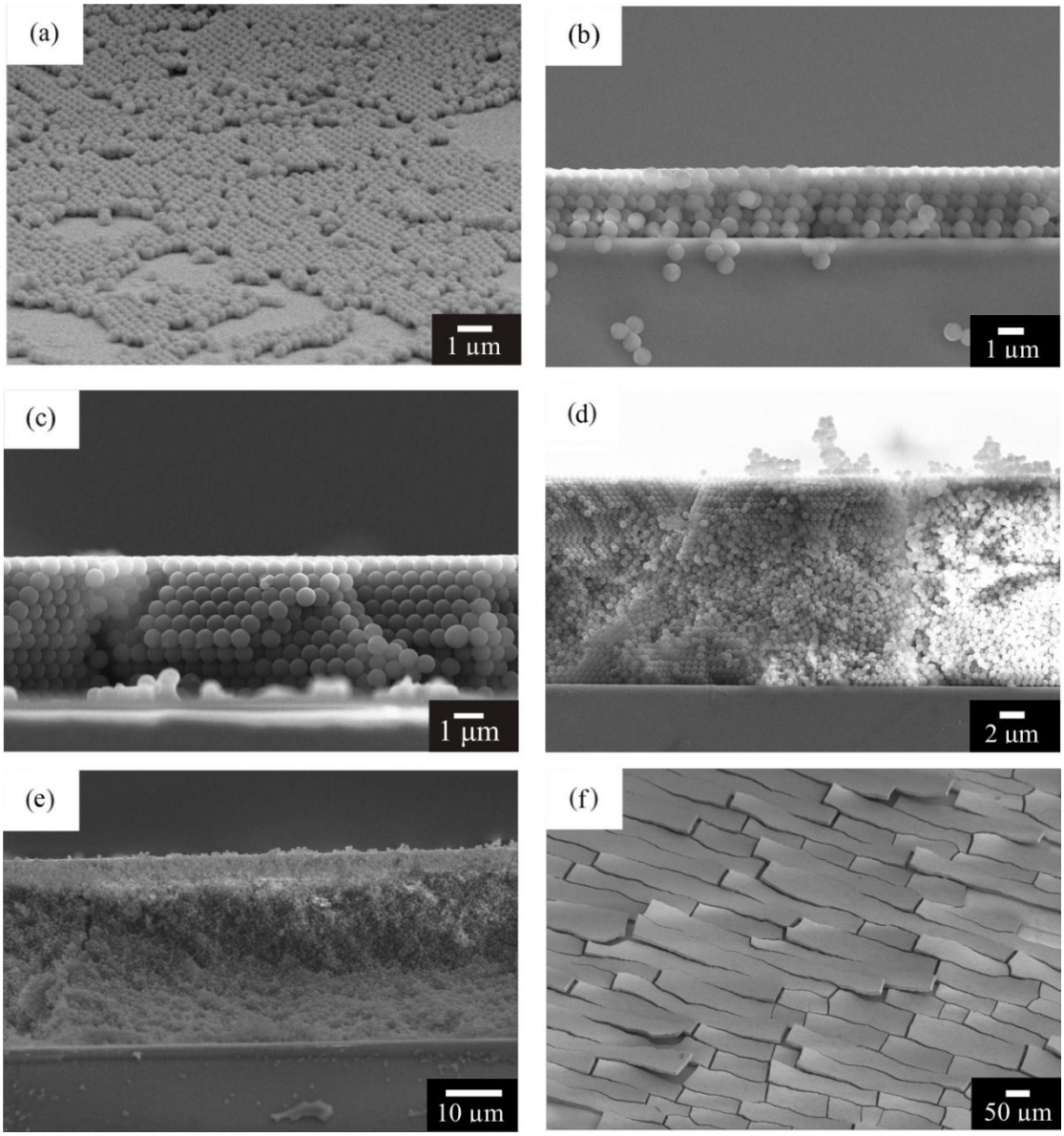

Figure 4-10 SEM images of polystyrene films prepared with increasing volume fraction (sphere diameter of 651 ± 23.4 nm) (a) 0.01 vol.%, (b) 0.05 vol.%, (c) 0.10 vol.%, (d) 0.30 vol.%, (e) 0.50 vol.% and (f) 1.00 vol.%.

When the concentration of the colloidal suspension was very low, the substrate was not fully covered and resulting film was non-uniform, as illustrated in Figure 4-10(a). With increasing colloidal concentration, the spheres become more ordered. However, when the concentration exceeds 0.50 vol.%, the order will be destroyed, as shown in Figure 4-10(e) and further increase in the volume fraction leads to delamination of the film, as shown in Figure 4-10(f).

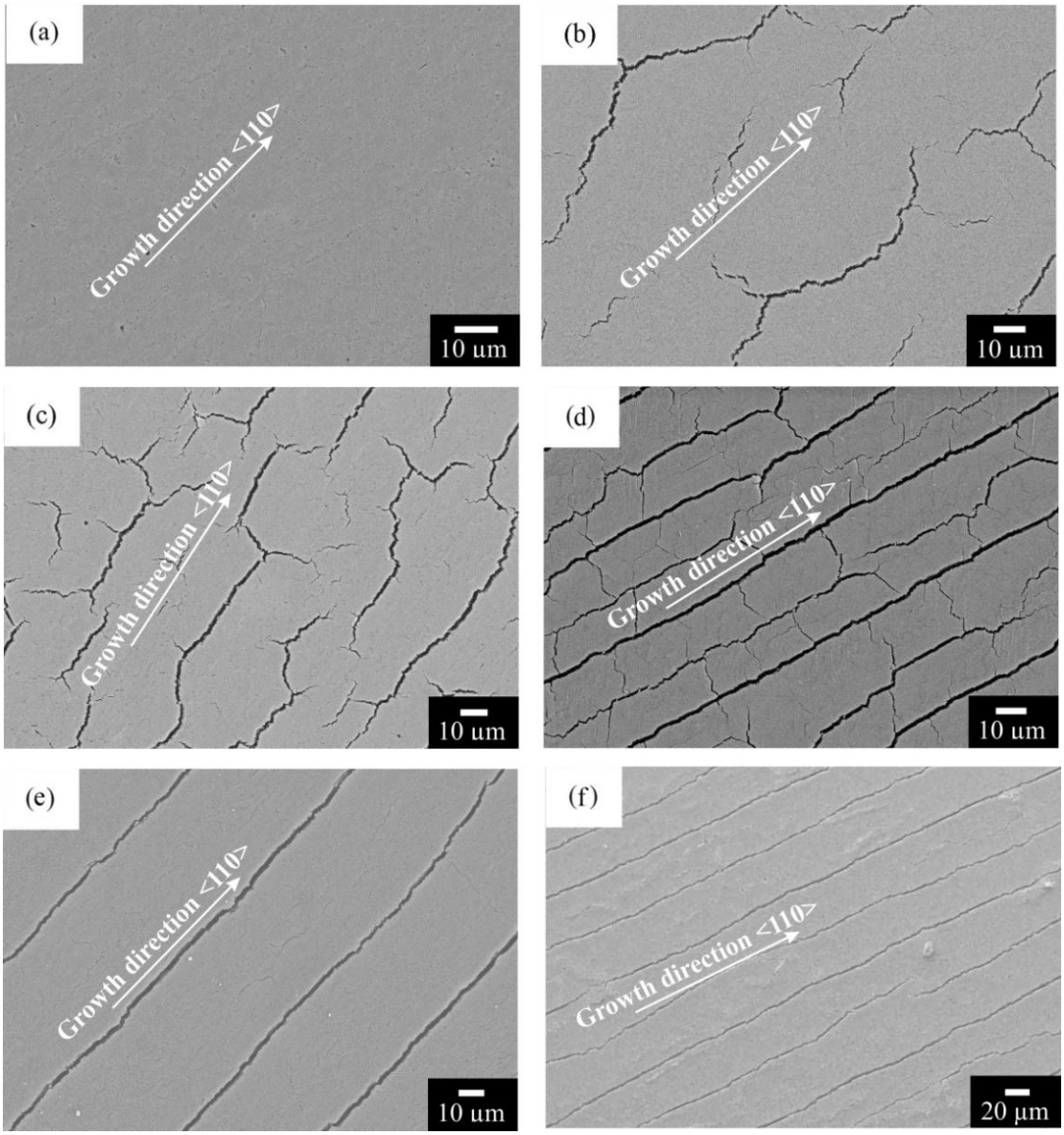

Figure 4-11 Crack pattern of polystyrene films with decreasing volume fraction (sphere diameter D = 327 ±6.0 nm) (a) 0.01 vol.%, (b) 0.05 vol.%, (c) 0.10 vol.%, (d) 0.30 vol.%, (e) 0.50 vol.% and (f) 1.00 vol.%.

Drying cracks are formed when the stresses that build up in the film are released during solvent removal. Low magnification SEM images in Figure 4-11 reveal the pattern of the drying cracks of the colloidal film made of the mean diameter of 327 nm spheres, which are similar to mud-cracks found at the bottom of dried riverbeds. Unlike classical grain boundaries, the order of spheres is preserved across the cracks. For all volume fractions investigated, the drying cracks are aligned exclusively along the growth direction as the stress associated with drying are released perpendicular to the meniscus. While the volume fraction decreases, the density of drying cracks increase but when the volume fraction is less than 0.10%, it decreases since the drying stress in thinner films is easier to be released in all spatial directions.

4.3.2 Microstructural analysis

4.3.2.1 Periodicity

All samples appear opalescent with colours from violet to red, depending on the angle of observation, clearly visible when illuminated from above with white light. The colour is uniform for the whole area of the film, suggesting that the lattice planes are aligned. The SEM image in Figure 4-12 confirms that polystyrene spheres are organized into a close-packed arrangement with long-range order both parallel and perpendicular to the glass substrate. It is apparent that the polystyrene spheres are closed packed with each spheres having six neighbouring spheres, corresponding to either a (111) surface of an f.c.c (ABCABCABC...) or a (100) surface of a hcp structure (ABABAB...). Though it is clear that the samples are also ordered in the cross-sectional view, it should noted that top surface views such as these cannot distinguish between the h.c.p and the f.c.c structure. According to previous published

reports, convective self-assembly results in the f.c.c lattice [185,186,235,236].

While SEM provides a good picture of the sample quality on the micron scale, the assessment of order over a larger range is best determined using fast Fourier transforms (FFTs) analysis of low magnification SEM (40×40 μm^2). The data is shown in the inset of Figure 4-12(a), in which the sharp spots indicate a high long-rang periodicity. Defects such as vacancies are randomly distributed on the top surface, as shown in Figure 4-12.

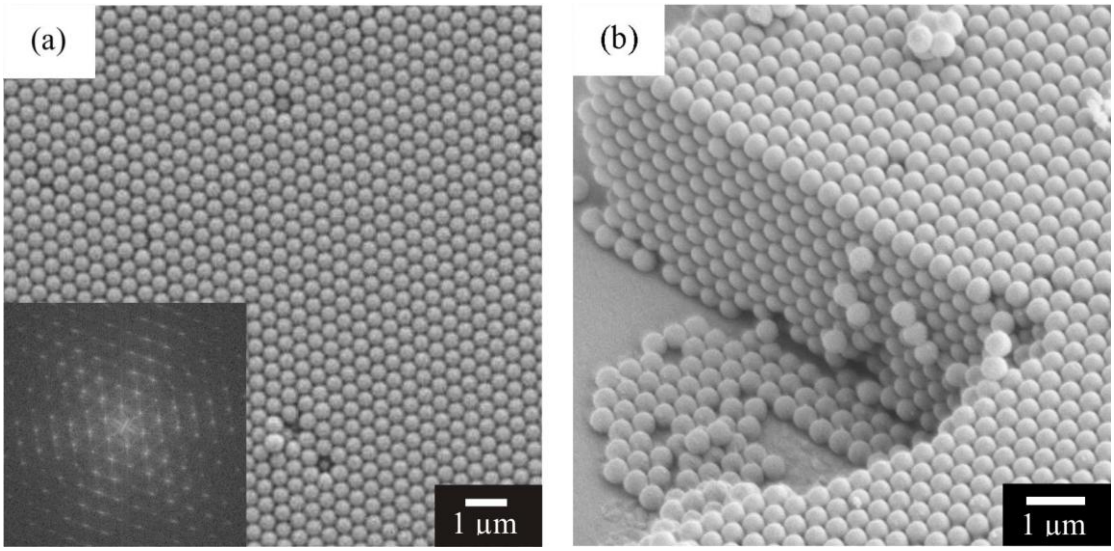

Figure 4-12 SEM images of the polystyrene films grown from 327 nm colloidal spheres (a) surface view (the inset is an FFT over a 40×40 μm^2 area) ; (b) a cleaved edge.

The three dimensional periodicity was further evaluated by reflectance spectroscopy. Figure 4-13 shows a series of angle resolved reflectance spectra obtained from the polystyrene films shown above with incident angle ranging from 10° to 50°. The reflection spectra of the film were recorded as a function of wavelength. All spectra have been background-subtracted and all the reflectance peaks have been normalised to a single value 1. The peaks in the reflectance spectra correspond to multiple Bragg reflections arising from the ordered structures [101,237].

The reflectance peaks are observed to shift progressively shorter wavelength region as the incident angle increases, as discussed in Section 3.3.2. Each spectrum exhibits apparent oscillations on both sides of the main peaks. The oscillations are Fabry-Perot fringes that stem from the interference of reflection from the top surface and bottom of the polystyrene films, indicating the high crystalline quality of the sample [185,238].

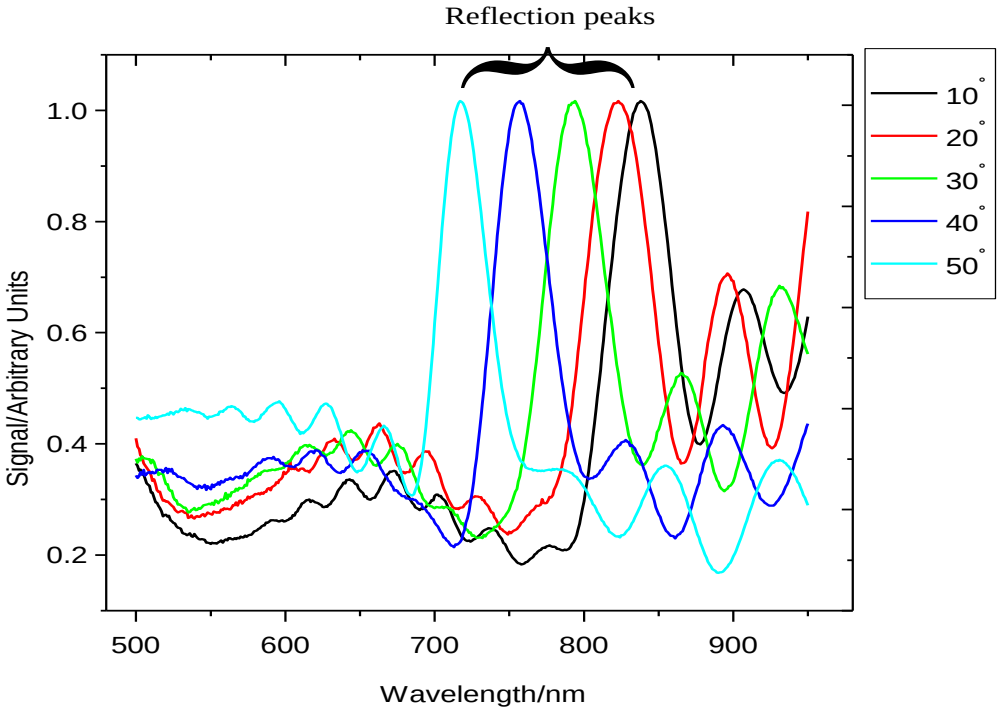

Figure 4-13 Normalised angle resolved reflectance spectra of the polystyrene film (Mean sphere diameter D = 327 ± 6.0 nm).

According to the combining Bragg's law and Snell's law (Equation 3.5), the lattice parameter and effective refractive index can be calculated. The peak wavelengths and corresponding incident angle are giving in the following table. The data in Table 4-2 were obtained from Figure 4-13. An error in λ of ± 7nm was taken into account for the peak wavelengths due to the surface roughness of the polystyrene

films [230]. Using Table 4-2, we can plot $sin^2\theta$ vs λ^2, as shown in Figure 4-14, and obtained the effective refractive index n_{eff} and sphere diameter D using Equation 3.7 and 3.8.

Table 4-2: Summary of the information of Figure 4-13

Diffraction Angle θ/°	$Sin^2\theta$	Peak Wavelength λ / nm	$\lambda^2/\mu m^2$
10	0.03	838 ±7	0.70 ±0.01
20	0.12	823 ±7	0.68 ±0.01
30	0.25	794 ±7	0.63 ±0.01
40	0.41	757 ±7	0.57 ±0.01
50	0.59	717 ±7	0.51 ±0.01

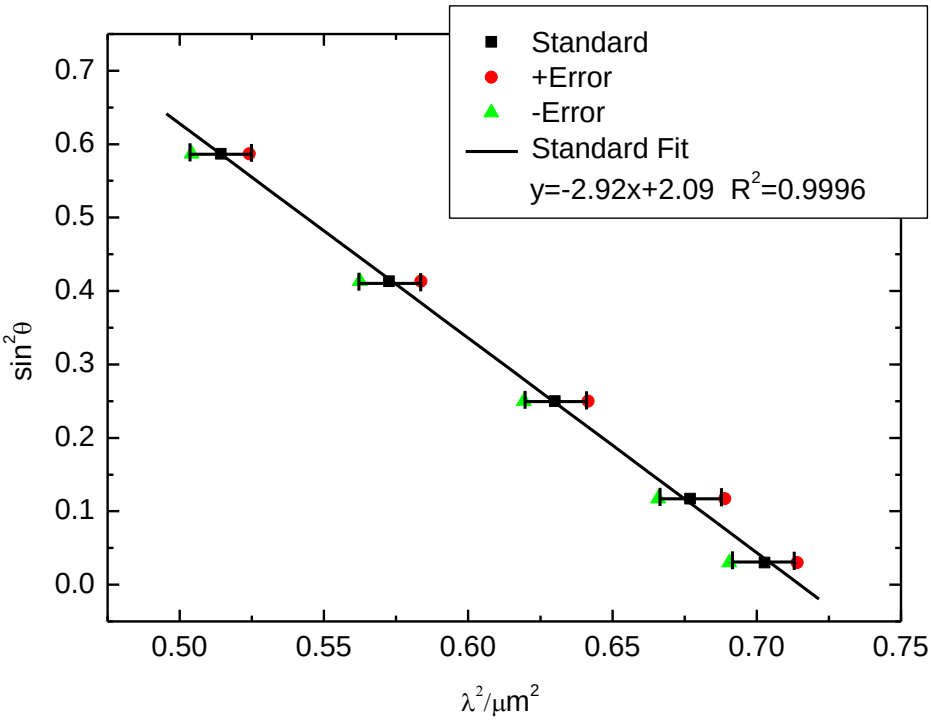

Figure 4-14 Linear fits for the reflection peaks in Figure 4-13.

The diameter of polystyrene spheres was determined to be 358 ± 2 nm. This value is slightly larger than the result obtained from TEM (327 ± 6.0 nm) as it was averaged from the diameters of the polystyrene spheres over a 1 mm^2 area while TEM

measurement was taken with only around 200 spheres. The effective refractive index of the structure n_{eff} can be theoretically determined by

$$n_{eff} = n_{PS} f_{PS} + n_{air}(1 - f_{PS}) \quad \textbf{(4.4)}$$

where n_{PS} and n_{air} are the refractive indices of the polystyrene spheres and the air voids, respectively, and f_{PS} is the volume fraction of the polystyrene spheres and is 74% for an f.c.c structure. Assuming n_{PS} is 1.54, n_{eff} will be 1.40, according to Equation 4.4. However the fitting value obtained from Figure 4-14 for n_{eff} is 1.44 ± 0.06, which is comparable to the theoretical calculation results.

4.3.2.2 Film thickness

As stated in Section 2.3.1.3, in convective self-assembly, the film thickness was determined by volume fraction of suspensions. Polystyrene films were grown with increasing volume fractions of 0.01%, 0.05%, 0.10%, 0.30%, 0.50%, to 1.00% from colloidal spheres of three different diameters 245 nm, 327 nm, and 651 nm respectively. To measure the film thickness with SEM, glass substrates were cleaved in the middle to reveal fracture sections. Figure 4-15 shows typical SEM images of polystyrene films grown from colloidal spheres of 327 nm in diameter.

Table 4-3: Number of layers and film thickness vs volume fraction

Volume fraction/vol%	Film thickness/μm		
	651 nm	327 nm	245 nm
0.01	/	/	/
0.05	2.51 ±0.02	1.37 ±0.03	1.22 ±0.05
0.10	5.01 ±0.16	5.06 ±0.74	4.15 ±0.06
0.30	19.59 ±0.98	18.95 ±0.22	17.20 ±0.23
0.50	28.95 ±0.33	22.53 ±1.17	28.68 ±0.82
1.00	Delaminated	53.90 ±0.22	37.15 ±0.83

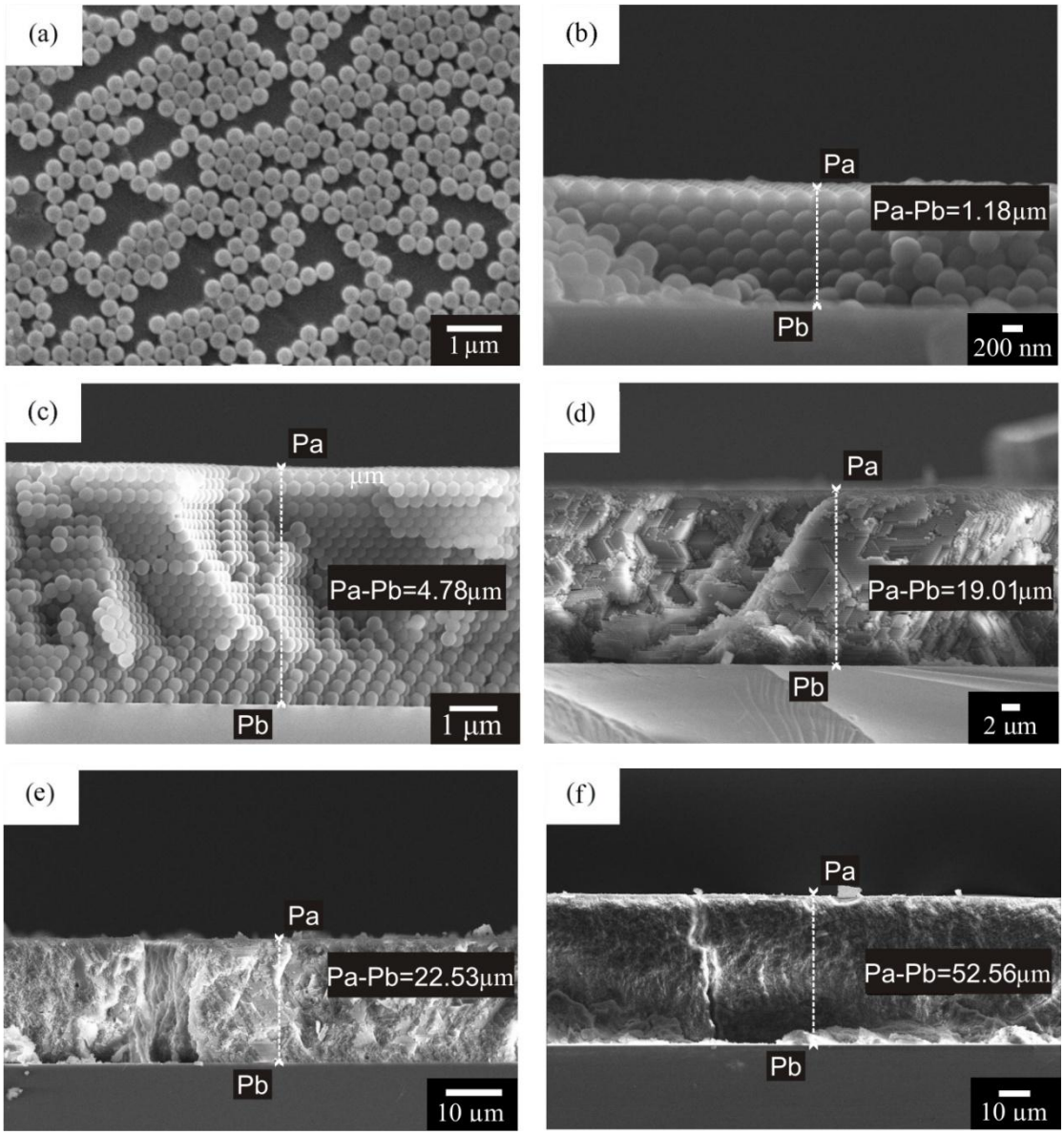

Figure 4-15 SEM images of polystyrene films prepared with increasing volume fraction (sphere diameter D = 327 ± 6.0 nm) (a) 0.01 vol.%, (b) 0.05 vol.%, (c) 0.10 vol.%, (d) 0.30 vol.%, (e) 0.50 vol.% and (f) 1.00 vol.%, in which Pa-Pb represents the distance from point a (Pa) on the top to point b (Pb) on the bottom.

The results of all films grown from the three different diameters are summarized in Table 4-3. Plotting film thickness versus volume fraction and the lines are the best-fit results using a linear function when volume fraction is over 0.05 vol%, as shown in Figure 4-16. The film thickness increases linearly with increasing the volume fraction, which is in agreement with Equation 2.4 and Colvin's work [186].

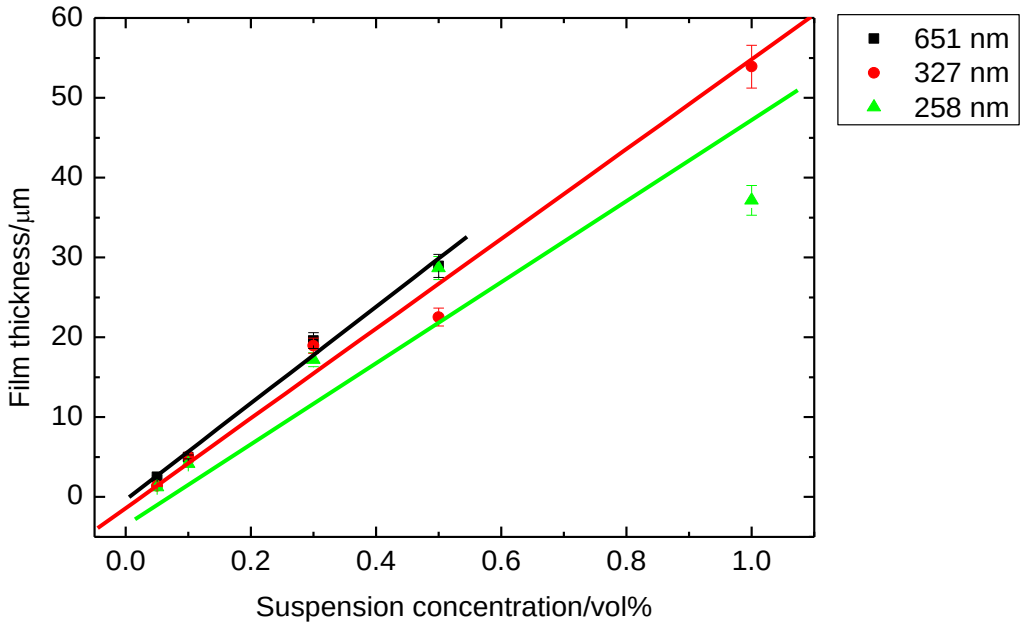

Figure 4-16 Dependence of the film thickness on the volume fraction.

In addition, Febry-Perot (FP) fringes can be used as a non-destructive technique to measure the film thickness [223] (refer to Section 3.3.2 for details). For example, with the information of FP fringes (marked with red arrows in the inserted picture in Figure 4-17) of the reflectance spectrum obtained from the incident angle of 10°, the wavelengths for each fringe and corresponding $2\sqrt{n_{eff}^2 - \sin^2\theta}(\frac{\lambda_1 - \lambda_{r+1}}{\lambda_1 \lambda_{r+1}})$ are summarised in Table 4-4. Plotting r vs. $2\sqrt{n_{eff}^2 - \sin^2\theta}(\frac{\lambda_1 - \lambda_{r+1}}{\lambda_1 \lambda_{r+1}})$ produces a straight line of film thickness as gradient, as shown in Figure 4-17. The thickness of this polystyrene film is calculated to be 5.21 ± 0.25 μm. Compared with the result from the SEM measurement (5.06 ± 0.74 μm), there is a little discrepancy between them because the optical analysis has given the average thickness of the film over a much larger (1 mm^2) area.

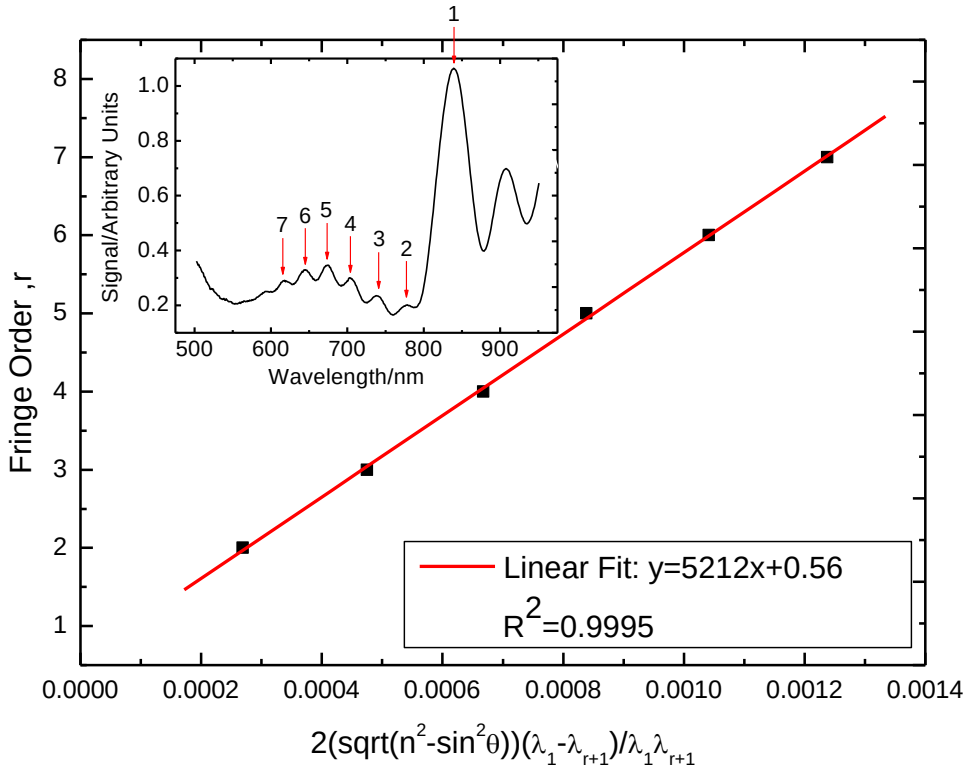

Figure 4-17 Linear fit to determine the thickness of the polystyrene film from the Fabry-Perot fringes obtained from the inset reflectance spectrum at incident angle of 10 °.

Table 4-4: Fabry-Perot fringes of the spectrum at 10° incident angle in Figure 4-17

Fabry-Perot fringe order r	λr/nm	$2\sqrt{n_{eff}^2-\sin^2\theta}\,\frac{\lambda_1-\lambda_{r+1}}{\lambda_1\lambda_{r+1}}$
1	838	/
2	777	2.69E-4
3	736	4.75E-4
4	702	6.67E-4
5	673	8.38E-4
6	643	1.04E-3
7	616	1.23E-3

4.4 Chapter summary

In this chapter, the synthesis and characterization of colloidal crystal templates for macroporous metals prepared from monodisperse polystyrene spheres through

convective self-assembly have been described. The films exhibit high crystallinity, as shown by SEM images and reflectance spectroscopy. The film thickness can be varied by volume fraction of colloidal suspensions. The films are stable and have a void fraction about 26%, which makes them capable of being filled and the planar and uniformity make them ideal for macroporous network templating. Moreover, since the starting template can be made from spheres of variable sizes, the void volume of the macroporous structures can be tuned accordingly.

5 3-DOM METALS VIA TEMPLATE-DIRECTED ELECTROCHEMICAL PLATING

5.1 Introduction

Metal electrochemical plating is a well-developed technique. In commercial plating solutions, a mixture of additives is widely used to enhance the film thickness distribution and to control the surface smoothness. The most common copper plating electrolyte is an acid copper sulfate based solution containing small amount of chloride ions and organic molecules known as brighteners, levellers, and suppressors [239-241]. The brighteners are sulphur-bearing organic molecules such as bis(sodiumsulfopropyl)disulfide (SPS) and the suppressors are typically polyethylene glycol (PEG) or polypropylene glycol (PPG). In most cases, an aromatic nitrogen-based molecule or polymer such as thiourea or benzotriazole (BTA), acts as a leveller to produce mirror-like plated surface. Chloride ions are added in the concentration range of a few mM [242-245] and act as a catalyst. In spite of the fact that the process has been used in industry for generations, the mechanism of the catalytic reaction is still a subject of debate. It has been demonstrated that copper reduced from commercial electrolytes is capable of filling micron- or submicron-sized trenches with depth-to-width ratio as high as 10:1 in a bottom-up fashion without voids [240,246]. However, the additives cause organic contamination sometimes. In this work, a non-additive copper acid plating solution is developed to obtain smooth and uniform copper structures.

Silver is generally reduced from silver cyanide electrolytes [73,247-251] with

or without additives but normally includes $Ag(CN)_3^{2-}$ or some other more complex species according to the cyanide concentration. The cyanide complex is favoured because it is stable. Table 5-1 gives the stability constants of various silver complexes, which shows silver cyanide having the highest stability [252]. Cyanide may be considered as an additive agent. It gives rise to strong adsorption, controls the silver reduction process and leads to deposits having suitable properties (good adherence to the base and homogeneity). On consideration of pollution and toxicity, several attempts have been performed to replace cyanoargentate ions by other silver electrolytes based on nitrate [163,253-255], thiourea [256,257], etc. These solutions have not been developed because of instability and/or low quality of the resulting deposit. Consequently, cyanide solutions are most commonly used in spite of their high toxicity. However the thiosulfate bath has shown to be a promising alternative to produce silver deposits in an efficient and non-toxic way [258-260]. It has high conductivity and adequate stability. The deposits are smooth and have good adherence to the substrates [261-263].

Table 5-1: Stability constants of silver complexes [252]

Complex ions	Logarithm of stability constant
$Ag(CN)_3^{2-}$ cyanide	21.10
AgI_3^{2-} iodide	13.68
$Ag(S_2O_3)_2^{3-}$ thiosulfate	13.46
$Ag(SCN)_4^{3-}$ thiocyanate	10.08
$AgBr_4^{3-}$ bromide	8.73
$Ag(SO_3)_2^{3-}$ sulfite	7.35
$Ag(NH_3)_2^{+}$ ammonia	7.05

Potentiostatic deposition is the most common method for electrochemical plating but galvanostatic deposition is advantageous in some applications. The galvanostatic deposition uses a three-electrode configuration, in which a constant

current is applied between the auxiliary and working electrodes, and the potential of the working electrode (measured with respect to the reference electrode) is monitored. Most industrial electrochemical depositions are operated galvanostatically, at a constant current, so that the growth rate will be exactly calculated. This is not possible during potentiostatic deposition that works with a constant voltage. However, during potentiostatic processing, one can identify with certainty the specific processes that will proceed at a significant rate at the applied voltage; during galvanostatic processing, the voltage can vary with time, and unwanted processes may occur.

5.2 Preliminary work

As reviewed in Section 1.2 and 2.2.3, though 3-DOM silver and copper are the most interesting candidates to achieve a complete PBG in visible or to serve as efficient SERS-active substrates, there are few reports on them due to the fabrication difficulties. In our work, the preparation of the 3-DOM structures was start with the testing of common electrochemical sources of silver and copper. We have found that macroporous copper could be simply reduced from copper sulphate acid solution. However the selection of silver bath was a tough task. Table 5-2 summarises the test outcome for a few silver bath, in which only silver thiosulfate and silver perchlorate baths have given multilayer macroporous structures while the former demonstrated cleaner but rougher structural properties than the latter, as shown in Figure 5-1(a) and (b). The reductions from simple silver ions ($AgNO_3$, Ag_2SO_4) have resulted in monolayer structures, see Figure 5-1(c) and (d). We assumed that the deposition from simple Ag^+ could take place on the ITO surface but the grains are over coarse, which block the metal penetrate outwards to the second layer of the polystyrene templates. We deposited silver onto bare ITO glass substrates without polystyrene templates

from silver nitrate and silver thiosulfate baths respectively and found those grown from simple silver ions bath resulted in much larger grain sizes, as shown in Figure 5-2. Moreover simple Ag^+ ions solutions - $AgSO_4$ and $AgNO_3$ electrolytes are not stable and black precipitates appear after 1 day storage.

Table 5-2: Macroporous silver from electrochemical growth

Silver source	Outcome
AgI_3^{2-}	Solution turned to yellow when the reaction begins.
$Ag(S_2O_3)_2^{3-}$	Multilayer porous silver, see Figure 5-1(a).
$Ag(SCN)_4^{3-}$	Black precipitates appear while voltage is applied.
$AgClO_4$	Multilayer porous silver, see Figure 5-1(b).
$AgNO_3$	Monolayer porous silver, see Figure 5-1(c).
AgCl	No metal being deposited.
Ag_2SO_4	Monolayer porous silver, see Figure 5-1(d).

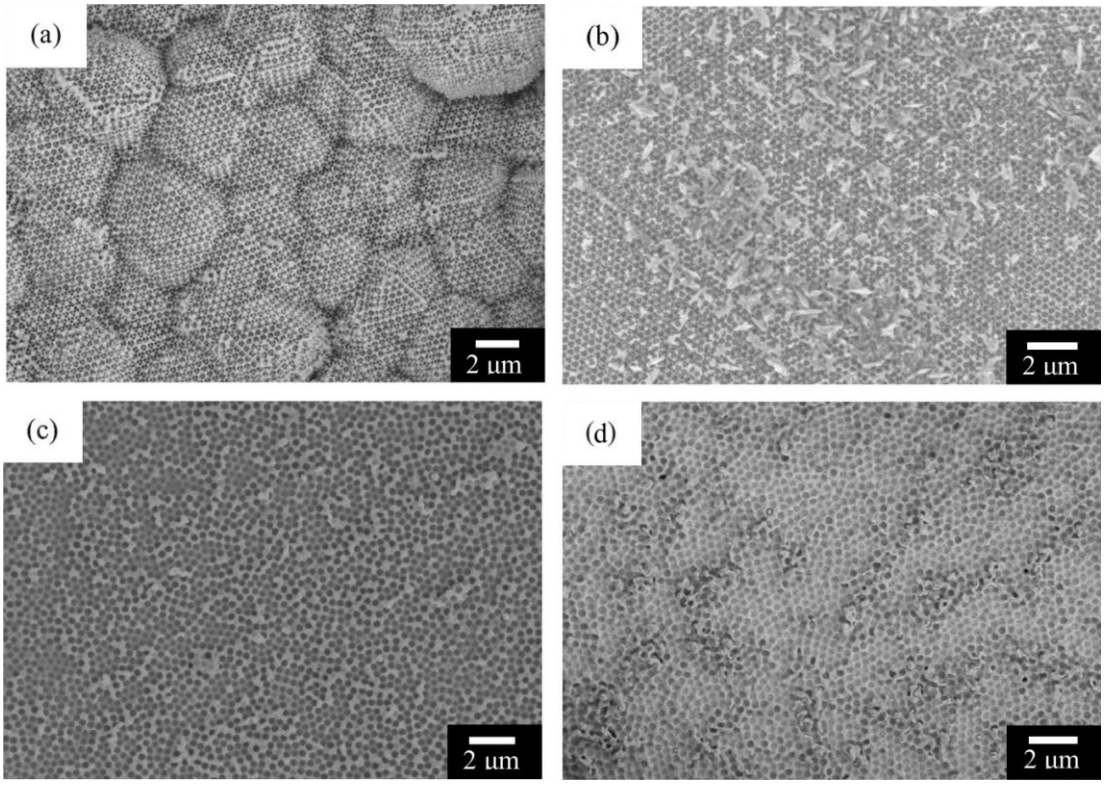

Figure 5-1 SEM images of macroporous silver reduced from various plating solutions (a) silver thiosulfate; (b) silver perchlorate; (c) silver nitrate; and (d) silver sulphate. They all resulted in macroporous structures but surface morphologies are completely different.

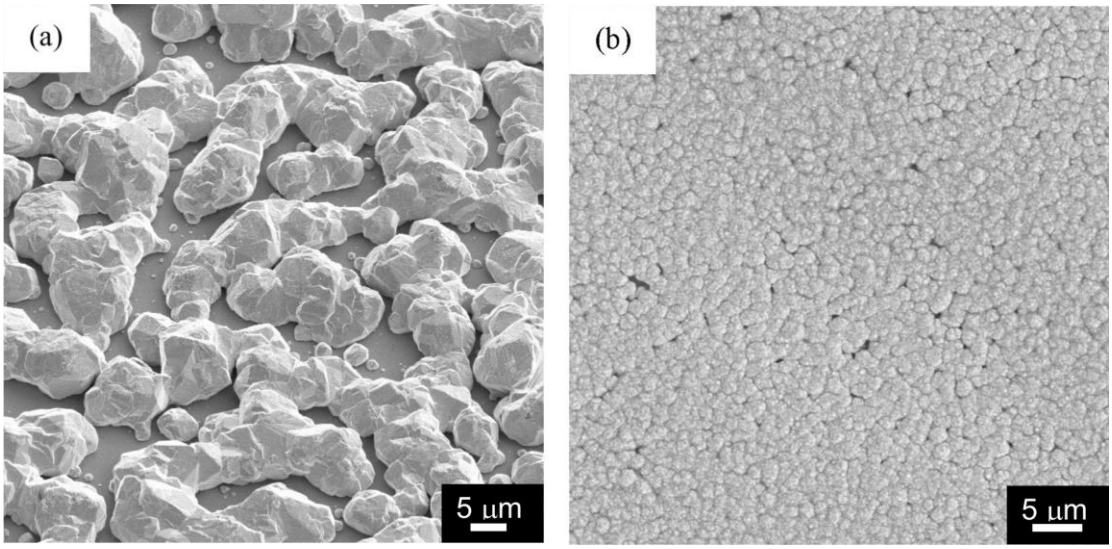

Figure 5-2 Electrodeposited silver without templating from (a) silver nitrate bath; (b) silver thiosulfate bath.

5.3 Experiment

5.3.1 Bath solution

Copper was reduced from 0.10 M copper sulfate ($CuSO_4 \cdot 5H_2O$, 98+%, reagent grade, Aldrich) solution and a mixed bath solution consisted of 0.10 M copper sulfate and 0.05 M hydrochloride acid (HCl, 37%, reagent grade, Aldrich) (pH ~ 1.3). The Cl^- ion is an addititive often being incorporated into copper electrochemical bath. The addition of a small amount (a few mM) of Cl^- has been found to modify the electrode kinetics essentially by increasing the transfer coefficient of the reaction of copper ion reduction [243-245].

As for silver, it was plated from complex ions and the bath contains 0.10 M silver nitrate ($AgNO_3$, 99+%, reagent grade, Aldrich), 0.10 M sodium chloride (NaCl, 99+%, Aldrich), and 0.25 M sodium thiousulfate ($Na_2S_2O_3$, 99%, Aldrich). The solution was prepared with deionised water and could be stored at room temperature for at least a month before observation of black precipitates. In addition, silver was

also reduced from silver perchlorate solution. To obtain the silver perchlorate solution, silver wire (99.99%, Advent Research Materials Ltd.) was connected as a work electrode and the bath was 5 mM perchloric acid solution ($HClO_4$, 70%, Aldrich). A positive voltage 500 mA was applied for 480 seconds and silver was dissolved in a 500 ml perchlorate acid solution following

$$2Ag(s) + 2H^+(aq) \rightarrow 2Ag^+(aq) + H_2(g)\uparrow \quad \textbf{(5.1)}$$

Hence the 5 mM silver perchlorate solution (pH ~ 2) was prepared and stored at room temperature.

The as-prepared polystyrene colloidal templates were used directly without any further treatment. They were robust and adhere well to the substrate. There was no evidence for re-suspension of the polystyrene particles when placed in the electroplating solution. The templates were masked with insulate tape with a circular area of 1 cm in diameter exposed to the plating solution. After the plating, samples were washed with deionised water and blow dried with nitrogen and subsequently dipped into toluene for at least 10 min to dissolve the polystyrene template in order to reveal the porous structure. After this, samples were taken out, rinsed with deionised water, nitrogen blow-dried and stored in desiccators.

5.3.2 Parameters

All experiments were carried out galvanostatically at room temperature with a conventional three-electrode setup: a saturated sulfate electrode ($HgSO_4$) as the reference electrode (RE), platinum wires were used as the auxiliary electrode (AE), and a piece of ITO glass slide assembled with the polystyrene template was served as the working electrode (WE), as illustrated schematically for cupric system deposition shown in Figure 5-3. Current densities were varied from -0.5 mA/cm^2, -1 mA/cm^2, -2

mA/cm^2, -3 mA/cm^2, -5 mA/cm^2, 8 mA/cm^2, -10 mA/cm^2, to -12 mA/cm^2, and for each current density, the plating time of 100s, 300s, 600s, and 900s was performed to give a total of 32 configurations. However for the silver films plated from silver perchlorate solution, a constant current density -2 mA/cm^2 was used but the plating time was varied from 600 s, 1800 s, 2400 s to 3600 s in order to gain a systematic result.

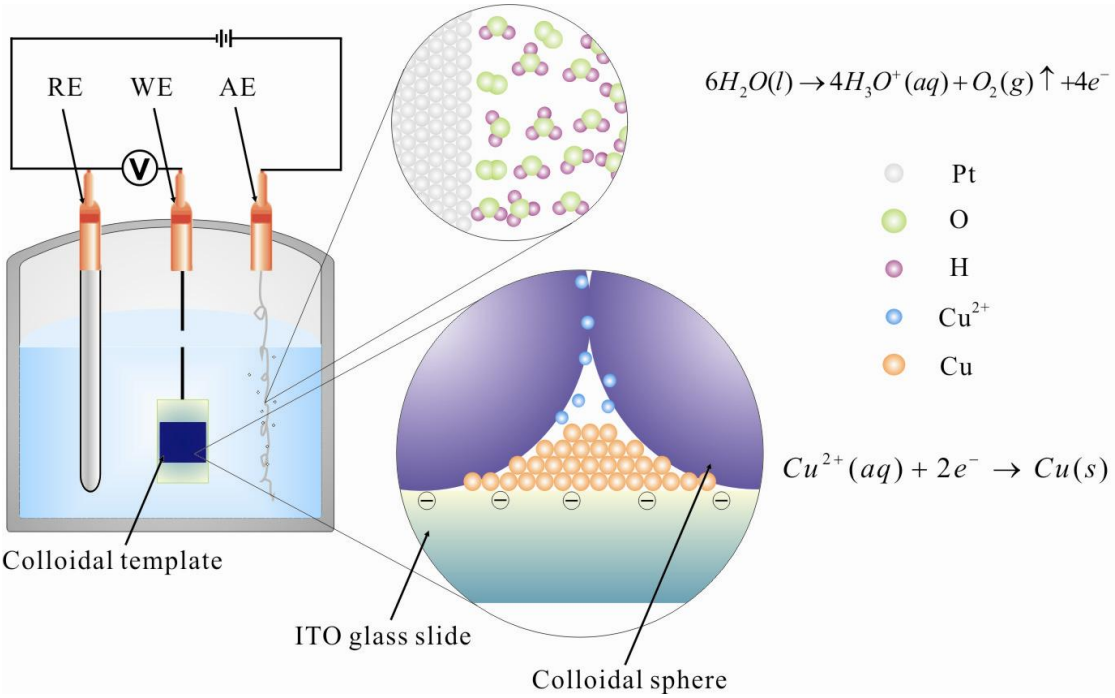

Figure 5-3 Schematic three electrodes setup of copper electroplating using acid $CuSO_4$ bath.

For copper reduced from simple cupric ions systems, the reaction at the working electrode/cathode was

$$Cu^{2+}(aq) + 2e^- \rightarrow Cu(s) \qquad E^0_{Cu^{2+}/Cu} = 0.337V \tag{5.2}$$

The balancing reaction at the auxiliary electrode was

$$6H_2O(l) \rightarrow 4H_3O^+(aq) + O_2(g) \uparrow +4e^- \quad E^0_{H_2O/O_2} = -1.229V \tag{5.3}$$

Therefore the overall reaction equation was

$$2Cu^{2+}(aq) + 6H_2O(l) \rightarrow 2Cu(s) + 4H_3O^+(aq) + O_2(g)\uparrow \quad \textbf{(5.4)}$$

Due to the low solubility of oxygen in water, bubbles were rapidly formed when the reaction occurs.

For silver reduced from the silver thiosulfate systems, the majority complex ion was $[Ag(S_2O_3)_2]^{3-}$.

$$Ag^+ + {S_2O_3}^{2-} \Leftrightarrow [Ag(S_2O_3)]^- \quad K_1 = 10^{8.82} \quad \textbf{(5.5)}$$

$$[Ag(S_2O_3)]^- + {S_2O_3}^{2-} \Leftrightarrow [Ag(S_2O_3)_2]^{3-} \quad K_2 = 10^{13.46} \quad \textbf{(5.6)}$$

Hence the reaction at the cathode was

$$[Ag(S_2O_3)_2]^{3-}(aq) + e^- \rightarrow Ag(s) + 2S_2O_3^{2-}$$
$$E^0_{[Ag(S_2O_3)_2]^{3-}/Ag} = 0.017V \quad \textbf{(5.7)}$$

The balancing reaction at the auxiliary electrode is

$$S_2O_3^{2-}(aq) + 15H_2O(l) \rightarrow 2SO_4^{2-}(aq) + 10H_3O^+(aq) + 8e^-$$
$$E^0_{S_2O_3^{2-}/SO_4^{2-}} = -0.716V \quad \textbf{(5.8)}$$

Therefore the over all reaction equation is

$$8[Ag(S_2O_3)_2]^{3-}(aq) + 15H_2O(l) \rightarrow 8Ag(s) + 2SO_4^{2-} + 15S_2O_3^{2-} + 10H_3O^+(aq) \quad \textbf{(5.9)}$$

For the silver reduced from the silver perchlorate solution, $AgClO_4$ acted as a source of Ag^+ and the reaction on the working electrode was

$$Ag^+(aq) + e^- \rightarrow Ag(s) \qquad E^0_{Ag^+/Ag} = 0.799V \quad \textbf{(5.10)}$$

All potentials at the work electrodes were monitored precisely with respect to the reference electrode and were recorded as function of plating time.

5.4 Results and discussions

5.4.1 Structural characterisation

5.4.1.1 Role of chloride ions

The function of chloride ions in copper electrochemical deposition has been examined. Chloride ions were reported to accumulate in the growing film and influence the film thickness distribution [243]. Figure 5-4(a) shows a SEM image of a copper thin film prepared without chloride ions in the electrochemical bath. Although the three-dimensional porous structure has been obtained, it exhibits rough surface and varied pore geometries, attributing to non-uniform film thickness. In contrast, when the deposition was carried out using the solution incorporated with chloride ions (~ 0.05 M), the film presents smooth surface and highly ordered pore arrangement, as shown in Figure 5-4(b). This confirms a small amount of chloride ions can enhance film thickness distribution.

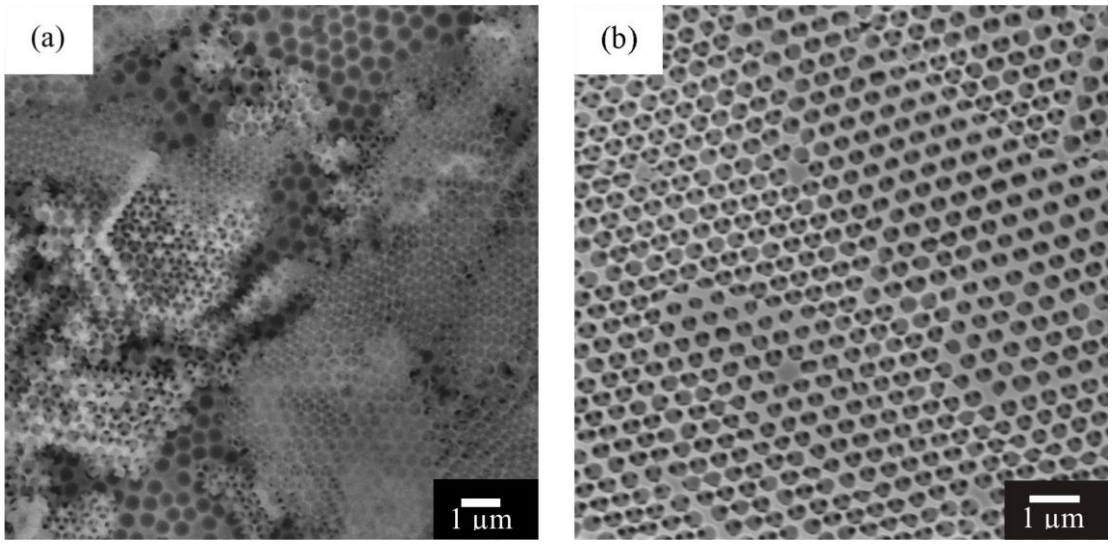

Figure 5-4 SEM images of macroporous copper films (a) prepared without 0.10 M copper sulphate solution, showing apparent uneven thickness distribution; (b) prepared 0.10 M copper sulphate solution incorporated with 0.05M chloride ions as additives, showing smooth uniform surface.

Figure 5-5 shows a few examples of the macroporous copper thin films plated

using the chloride ions involved acid copper sulfate electrolyte. The current density and plating time were constant at -5 mA/cm^2 and 600 seconds, respectively. They all present periodic arrangements of macro-sized pores, which were inversely replicated from the colloidal crystal templates. The top surfaces are uniform and display similar pore geometries, which demonstrated that the porous structure is highly reproducible.

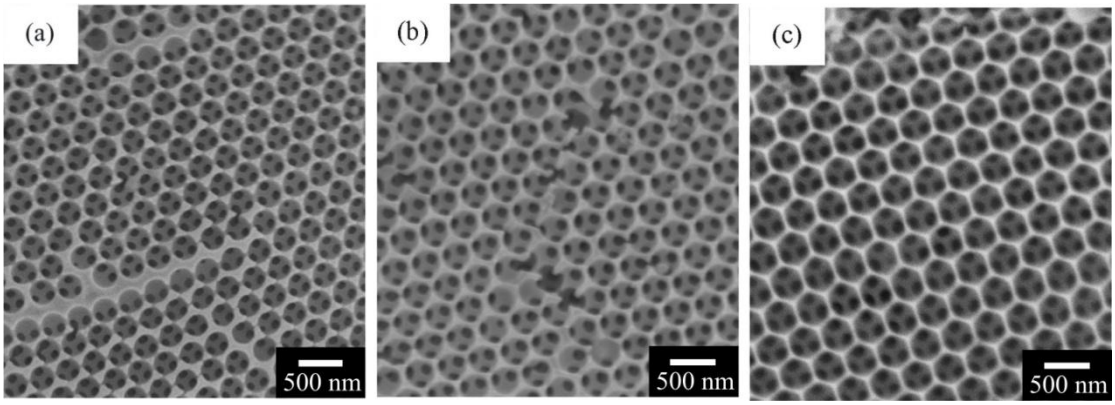

Figure 5-5 SEM images of macroporous copper films prepared using acid Cu^{2+}/Cl^- bath with current density *i* = -5 mA/cm^2 and plating time t = 600 s.

5.4.1.2 Porous structure

The colloidal spheres were self-assembled into an f.c.c lattice and each sphere was in contact with 12 nearest neighbours. Therefore, when the plating solution infiltrated into the interstices between the colloidal spheres it could not reach the contact regions, then removal of the colloidal templating spheres left behind macropores with interconnecting windows that were formed at the contact regions between the colloidal spheres, as illustrated in representative SEM images of macroporous copper and silver in Figure 5-6. Air voids replaced the position of polystyrene spheres. The mouths of these voids are approximately circular and through each hole of the top layer, three black holes of the second layer are visible, demonstrating the macroporous metal has a three-dimensional framework, as

illustrated in Figure 5-6(a) & (c) for copper and silver respectively. In addition, a fracture section of macroporous copper in Figure 5-6(b) and a focused ion beam (FIB) cleaved cross section of macroprous silver in Figure 5- 6(d) show that the layer by layer ordered pores mirroring the ordered arrays of the polystyrene spheres. The insets in Figure 5-6(a) & (c) are FFTs calculted from low magnification SEM images of 20 × 20 μm^2 in area. The sharp reciprocal spots can be regarded as a diffraction pattern, confirming long-rang periodicity in the porous thin films.

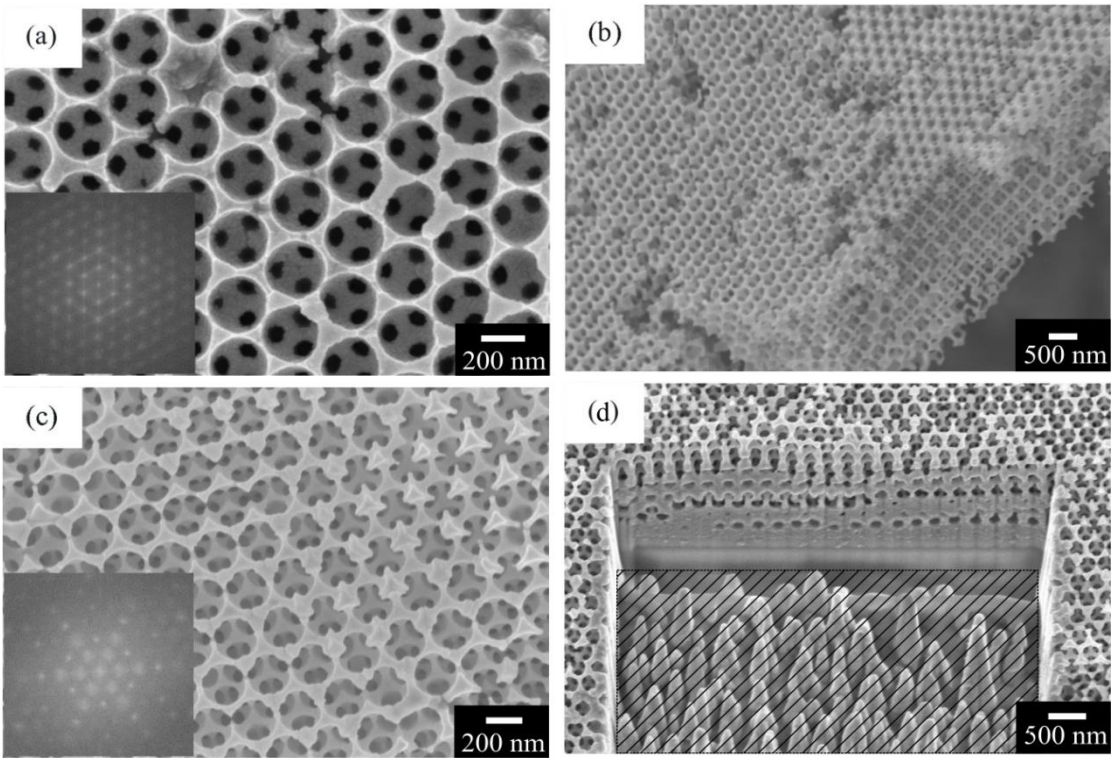

Figure 5-6 SEM images of macroporous copper and silver thin films (a) & (c) top surface view, inserts are FFT images obtained from areas of 20 ×20 μm^2; (b) fractured edge of copper film and (d) cross sectional view of silver film, features shaded are from FIB damage.

In addition, the pore centre-to-centre distance is comparable to the diameter of the polystyrene spheres used. For example, the centre-to-centre distances of the films shown in Figure 5-6 are measured as 315 ± 15 nm and 314 ± 17 nm for copper and silver respectively and the original polystyrene sphere size was 327 ± 6.0 nm. This

confirms the inverse films do not suffer significant shrinkage after the removal of the template and this is one of main advantages of the electrochemical plating.

5.4.1.3 Surface morphology

The smooth top surface of the polystyrene film has been mirrored in the macroporous copper film, as shown in Figure 5-7(a) & (b). This suggests a uniform growth over all the plating area. On the other hand, the silver film displays a much rougher, stepped surface. In the macroporous silver film, there appear to be ´´domains´´, varying in size from ~ 1 μm to 4 μm, as illustrated in Figure 5-7(c), although the pore centre-to-centre distance matches the diameter of the polystyrene template spheres. A closer inspection and cross sectional view in Figure 5-8 reveal that the domains are near-surface features - the porous structures are continuous at the bottom but step up to the surface. The 'floret'- like appearance could be due to the malleability of silver, which leaded to some restructuring during drying. Similar features have been observed in electroless plated macroporous gold structures reported by Jiang *et al.* [214]. However, the authors did not take any further investigations on the surface.

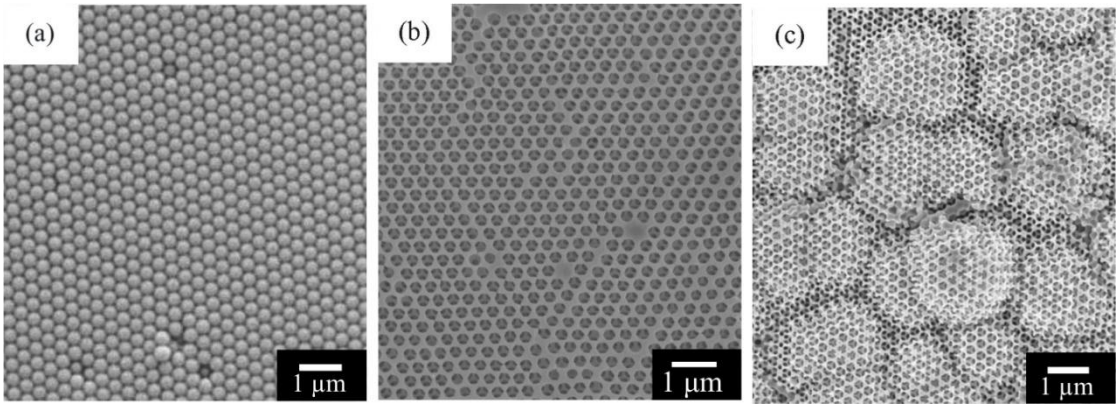

Figure 5-7 Surface features of the thin films (a) colloidal template, (b) corresponding inverted macroporous copper and (c) macroporous silver.

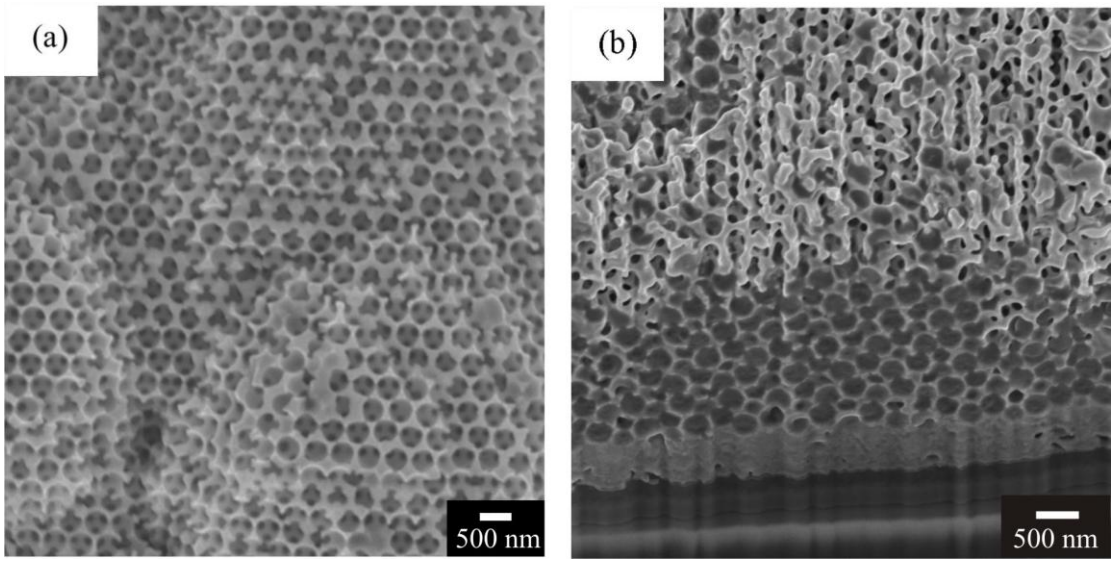

Figure 5-8 SEM images of the 3-DOM silver structures (a) high magnification surface view; (b) cross sectional view, revealed by FIB. Both images confirms porous structures are continuous at the bottom but step up to the surface.

Figure 5-9 shows low magnification top surface view SEM images of the polystyrene template and corresponding inverse copper and silver. Macroporous domains of either copper or silver thin films extend over comparable size of the original polystyrene domains (~ 40 μm in width), which indicates that the electroplating does not disrupt the long-range order of the structure. Since the electrochemical plating is a volume-template technique, the metal elements would fill any vacancies in the colloidal template from the bottom upwards the top surface. Also, preferential plating sites were expected to be the pre-existing drying cracks where transport is more facile than those between the polystyrene spheres. However, a significant difference was observed between the macroporous silver and copper. Silver has been plated directly into both the interstitial spaces between the colloidal spheres and all the drying cracks between domains and the solid silver joints all macroporous domains together hence enhances mechanical strength of the frameworks; while the copper formed isolated domains located exclusively along the

crack direction, with the cracks remaining unfilled. The SEM image of a cleaved silver film in Figure 5-10(b) shows clearly that the drying cracks have been completely filled from the bottom up. The silver formed a ridge abutted over the cracks due to higher ions transpor at these positions; while the copper cross sectional image in Figure 5-10(a) shows a gap between the macroprous domains.

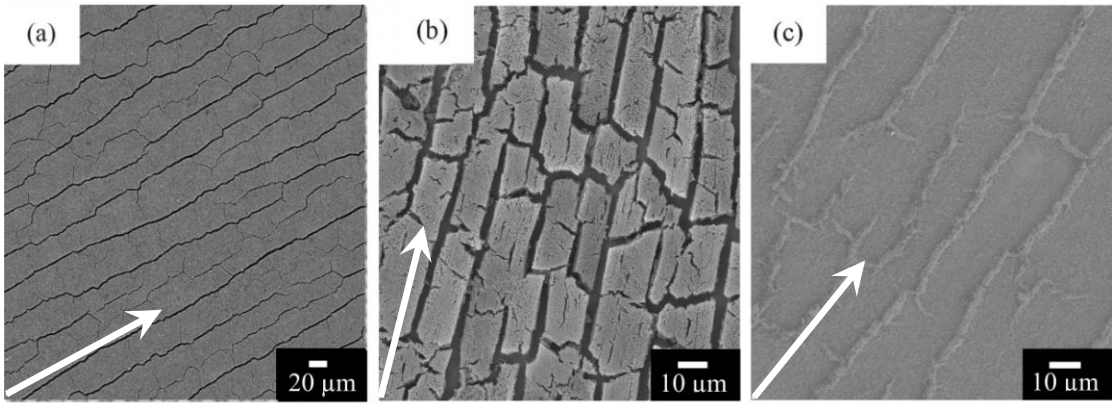

Figure 5-9 Low magnification SEM top surface view (a) colloidal template and corresponding inverted structures (b) macroporous copper and (c) macroporous silver. The growth directions are indicated by arrows.

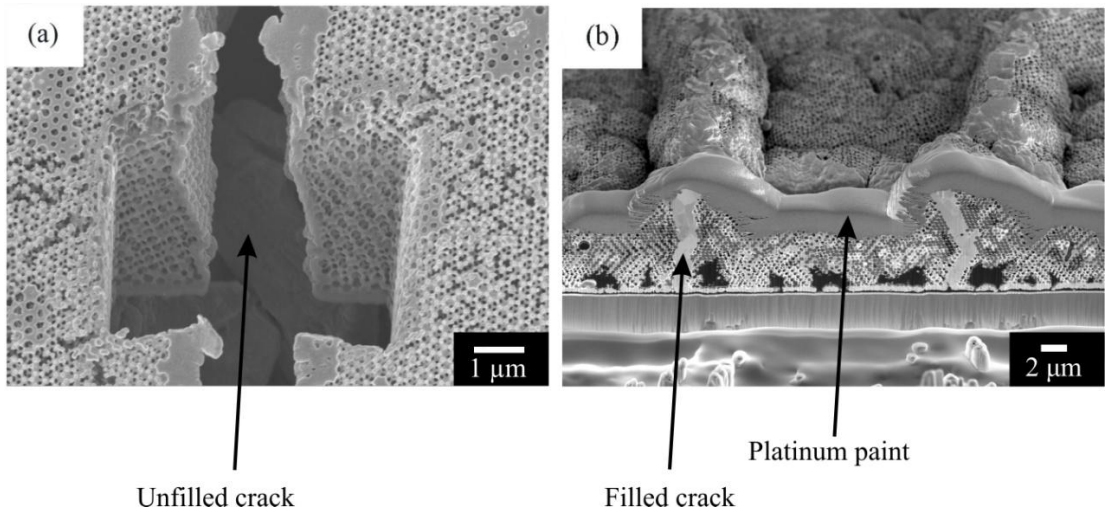

Figure 5-10 Unfilled or filled cracks in macroporous films (a) in copper, drying crack of the polystyrene template is remain; (b) in silver, crack has been completely filled by dense metal.

Going back to the surface topography, the differences observed in Figure 5-7

of the two surfaces can be explained by their macrostructure. In the case of silver, there was a dense network which restricted macroporous domains. Nucleation started from various sites on the substrate and stress would be built when different nucleation areas met each other. The stress has been relieved upwards, resulting in the step up porous structure. In the macroporous copper film, isolated macroporous domains were formed but the absence of dense copper in the cracks means that the stress could relax laterally, resulting in the flat smooth surface.

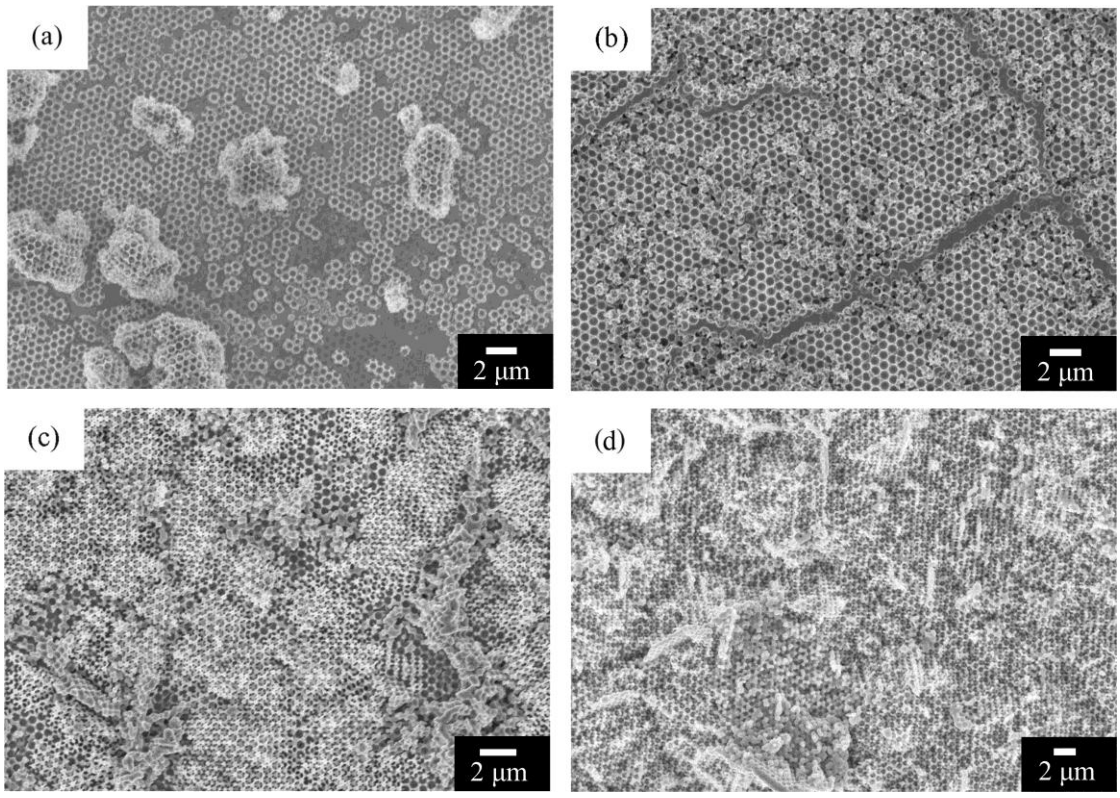

Figure 5-11 SEM images of macroporous silver thin film grown from silver perchlorate bath with templating sphere size D = 651 nm and current density i = -2 mA/cm^2, plating time were (a) 600 s; (b) 1800 s; (c) 2400 s and (d) 3600 s.

For the silver plated from silver perchlorate solution, the SEM images in Figure 5-11 reveals that after the removal of the polystyrene templates, the spherical voids inverted from the original colloidal spheres are presented. However, the periodicity has been ruined by non-uniform nucleation at different spatial sites. For a

plating time of 600 s, the conductive glass substrate has yet been fully covered and it produced discontinuous shallow ´´dishes´´. Meanwhile at certain positions, porous structures have exceeded monolayer, referring to Figure 5-11(a). The substrate was fully covered by the porous structure when plating time was 1800 s, as shown in Figure 5-11(b), although the isolated multilayer porous structures are remain randomly distributed all over the plating area. When the plating time reached 3600 s, non-uniform growth rate left a porous structure with rough surfaces after templating sphere removal, as illustrated in Figure 5-11(d).

5.4.2 Isolated macroporous domains

5.4.2.1 Hypothesis - copper dissolution

In the copper electrochemical plating using acid Cu^{2+}/Cl^{-} bath, isolated macroporous domains were formed with the drying cracks of the polystyrene templates remaining unfilled. We now consider the possible why one system results in a filled structure and one remains as isolated domains. If we consider the electrochemistry of the acid Cu^{2+}/Cl^{-} system, there are quite a few of reactions that may occur, as concluded in Table 5-3.

Since CuCl and $CuCl_2^{-}$ are yellowish and neither of them was being observed, the reactions of Equation 5.15 to 5.17 can be negligible. Hence possible reactions occurred in the drying cracks are copper oxidation and dissolution incorporate with oxygen. It was assumed that at the start of the deposition, the majority of Cu^{2+} ions were reduced to metal copper and the process was mainly controlled by Cu^{2+} diffusion from the solution to the surface of the electrode. When oxygen existed in the solution, at low oxygen pressure, the copper oxidation rate was controlled by the transport of dissolved oxygen to the surface of working electrode [264]. Both copper

deposition and oxidation rate would be expected to be higher in the cracked areas where diffusion is much faster than the interstitial spaces between polystyrene spheres. As a result, any copper elements that were plated in the drying cracks would be rapidly dissolved hence leaving the cracks unfilled.

Table 5-3: Possible reactions in acid Cu^{2+}/Cl^- bath

Reaction	Standard potential	Equation
$Cu^{2+}(aq)+e^- \rightarrow Cu^+(aq)$	$E^0_{Cu^{2+}/Cu^+}=0.159V$	5.11
$Cu^+(aq)+e^- \rightarrow Cu(s)$	$E^0_{Cu^+/Cu}=0.520V$	5.12
$2Cu(s)+\frac{1}{2}O_2(g) \rightarrow Cu_2O(s)$	/	5.13
$Cu_2O(s)+2H^+(aq) \rightarrow 2Cu^{2+}(aq)+H_2O(l)+2e^-$	$E^0_{Cu_2O/Cu^{2+}}=0.203V$	5.14
$Cu^{2+}(aq)+Cl^-+e^- \rightarrow CuCl(s)$	$E^0_{Cu^{2+}/CuCl}=0.559V$	5.15
$CuCl(s)+e^- \rightarrow Cu(s)+Cl^-(aq)$	$E^0_{CuCl/Cu}=0.137V$	5.16
$Cu(s)+2Cl^- \rightarrow CuCl_2^-(aq)+e^-$	$E^0_{Cu/CuCl_2^-}=0.224V$	5.17

A schematic image of the copper dissolution process is shown in Figure 5-12, in which the total electroplating voltage V_1 is consisted of two parts – the voltages drives the copper dissolution V_2 and that of the copper reduction V_3.

$$V_1 = V_2 + V_3 \qquad \textbf{(5.18)}$$

According to the Nernst equation

$$E = E^0 - \frac{RT}{nF}\ln\frac{[red]}{[ox]} \qquad \textbf{(5.19)}$$

where the ratio [red]/[ox] is equivalent to the probability of being reduced ions over that of being oxidized ions, R is the universal gas constant, R = 8.314 $JK^{-1}\ mol^{-1}$, T is the absolute temperature and F is the Faraday constant, F = 9.6485×104 $C\ mol^{-1}$. At room temperature (25 ℃), RT/F may be treated as a constant and replaced by

0.0592 V. *n* is the number of electrons transferred, which is 2 for Cu^{2+}.

Thus

$$V_2 = E^0_{Cu_2O/Cu^{2+}} - \frac{0.0592}{2} \ln \frac{1}{[Cu^{2+}_{diss}]^2} \quad \textbf{(5.21)}$$

$$V_3 = E^0_{Cu^{2+}/Cu} - \frac{0.0592}{2} \ln[Cu^{2+}] - E^0_{RE} \quad \textbf{(5.22)}$$

where the value of $E_{RE}{}^0$ was taken as 0.658 V for the CR5-$HgSO_4$ reference electrode used. Since dissolution potential V_2 represented a negative value with respect to the oxidation voltage V_3, it was expected that the voltage V_1 would more negative when the dissolution commenced.

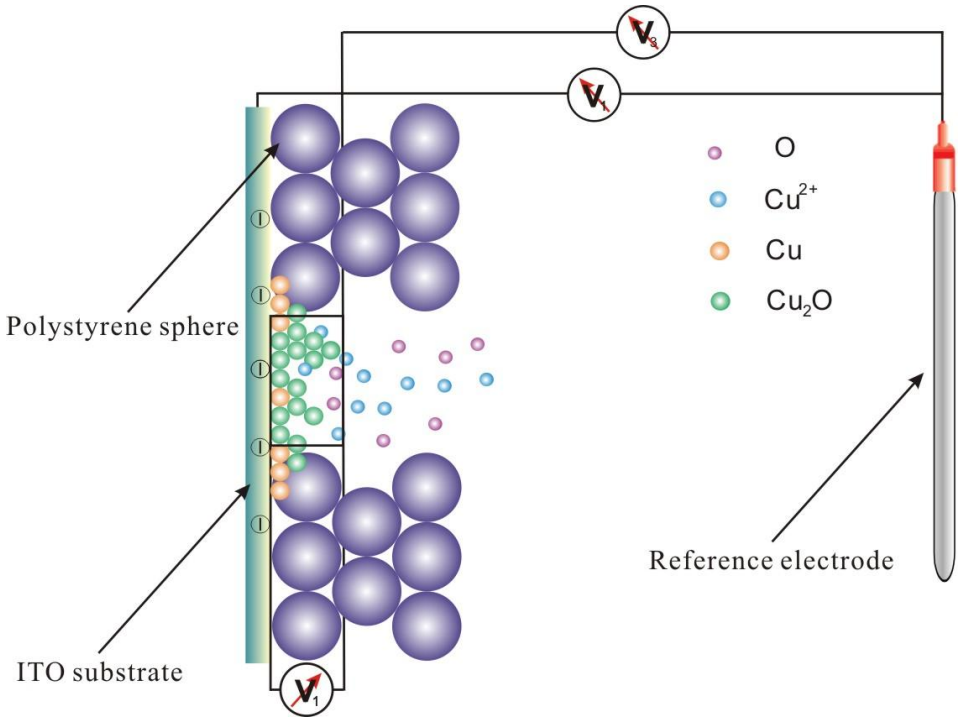

Figure 5-12 Copper reduction and dissolution can be illustrated as reactions in two cells. Total voltage recorded combines potentials of both processes $V_1 = V_2 + V_3$.

5.4.2.2 Plating chemistry

To prove that oxygen diffusion is critical to the copper dissolution, we repeated the experiments in oxygen-free solutions. A flow of bubbling argon was kept

in the solution during the plating process to purge oxygen from the solution.

In addition, we deposited copper using copper glycerol solution which is free from O_2 or Cl^- but consists of 0.10 M copper sulfate ($CuSO_4 \cdot 5H_2O$, 98+%, reagent grade, Aldrich), 0.20 M glycerol ($C_3H_5(OH)_3$, 99+%, Aldrich), 0.60 M sodium hydroxide (NaOH, 98+%, reagent grade, Aldrich), and 1.00 M sodium sulphate (Na_2SO_4, 98+%, reagent grade, Aldrich) to reduce the grain size [265]. All solutions were freshly prepared with deionised water. Copper ions were transformed to Cu(glyc) and $[Cu(glyc)_2]^{2-}$ complex ions following:

$$2Cu^{2+} + 2C_3H_5(OH)_3 + 3OH^- \rightarrow [Cu_2(OH)(glyc)_2]^+ \downarrow + 2H_2O \quad \textbf{(5.23)}$$

$$Cu_2(OH)(glyc)_2^+ + OH^- \rightarrow 2Cu(glyc) + 2H_2O \quad \textbf{(5.24)}$$

$$Cu(glyc) + C_3H_5(OH)_5 + 2OH^- \rightarrow [Cu(glyc)_2]^{2-} + 2H_2O \quad \textbf{(5.25)}$$

Copper was deposited onto the polystyrene template by:

$$Cu(glyc)(aq) + 2H_2O(l) + 2e^- \rightarrow Cu(s) + C_3H_5(OH)_5(l) + 2OH^-(aq) \quad \textbf{(5.26)}$$

$$[Cu(glyc)_2]^{2-}(aq) + 4H_2O(l) + 2e^- \rightarrow Cu(s) + 2C_3H_5(OH)_5(l) + 4OH^-(aq) \quad \textbf{(5.27)}$$

After plating, the polystyrene spheres were removed by toluene dissolution and the samples were blow-dried with nitrogen.

The voltage of the reduction process of the argon degassed Cu^{2+}/Cl^- bath was recorded as function of plating time and as shown in Figure 5-13. Potential vs. plating time (E-T) curves from the oxygen involved bath at the same current density of -5 mA/cm^2 and -8 mA/cm^2 were added for comparison. Considering the dissolution hypothesis, the voltage of O_2 involved bath would be lower than that of the Argon degassed one and the voltage difference is determined by the copper dissolution rate.

Since both of the copper reduction and dissolution rate increase with increasing current density, the voltage difference would be going higher too. The voltages of the O_2 involved bath were more negative at ~ -100 mV and -500 mV lower than that of the degassed bath for -5 mA/cm^2 and -8 mA/cm^2, respectively. This is consistent with the hypothesis.

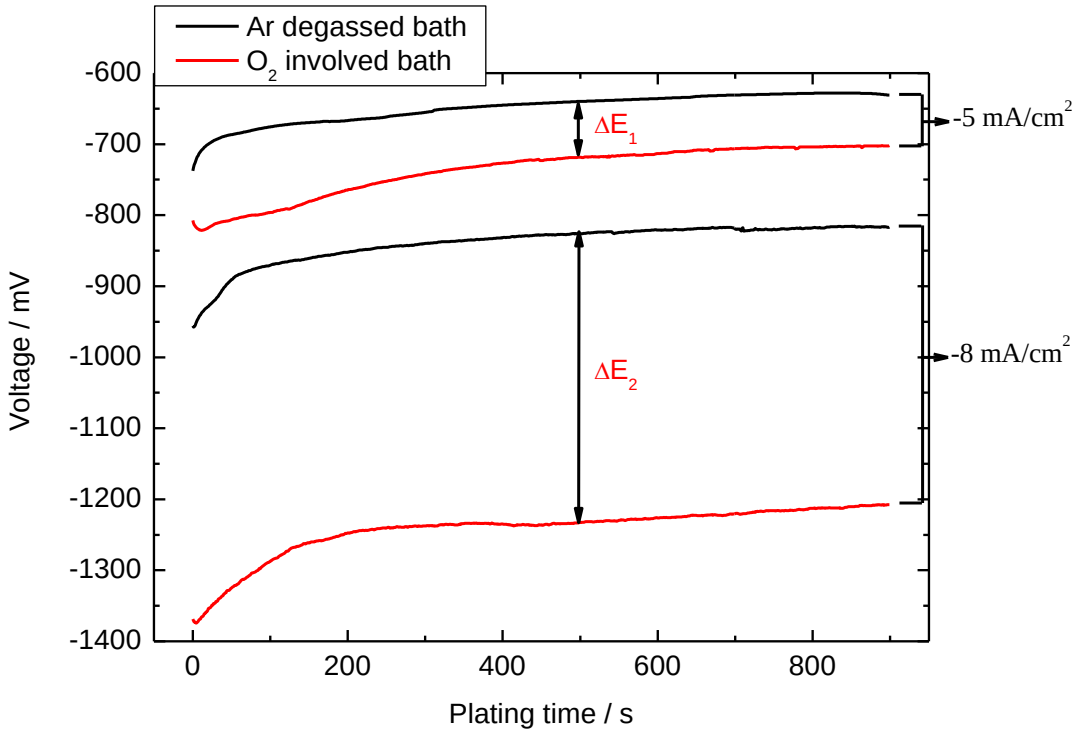

Figure 5-13 E-T lines of argon degassed and O_2 involved acid Cu^{2+}/Cl^- bath, potential difference ΔE is attributed to copper dissolution.

5.4.2.3 Structural analysis

Figure 5-14 illustrates SEM images of the macroporous copper films grown from the degassed Cu^{2+} and copper glycerol solution and all drying cracks have been filled. Closer inspections over the filled cracking areas are illustrated in Figure 5-15. Before removal of the colloidal spheres, dense metal deposits are detectable in the drying cracks of the polystyrene film, as shown in Figure 5-15(a). When the

polystyrene spheres have been dissolved, it is revealed that the dense copper joints macroporous domains together (Figure 5-15(b)). A cross sectional image further confirmed the crack has been completely infiltrated from bottom up to the exposed the surface, referring to Figure 5-15(c).

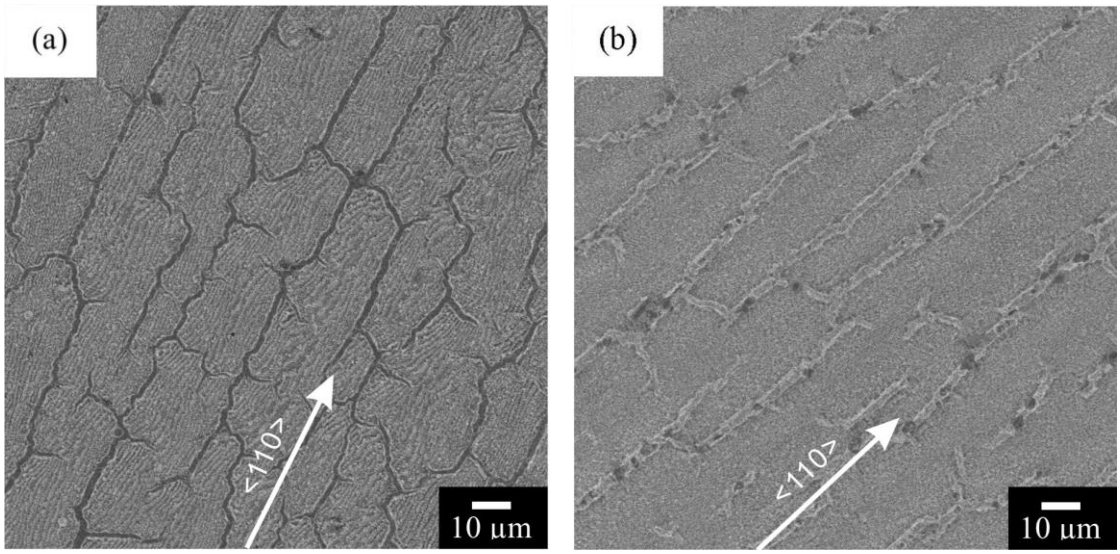

Figure 5-14 Top surface view of macorporous copper films plated from oxygen free bath (a) argon degassed solution (b) copper glycerol solution. Arrows represent crack directions <110>, which were the growth direction of the colloidal templates.

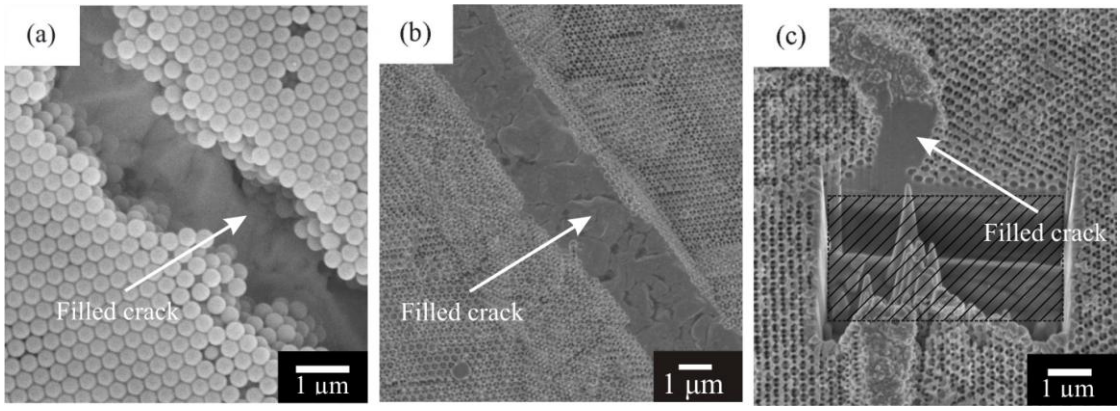

Figure 5-15 Crack filled films plated from oxygen free copper glycerol bath (a) polystyrene copper composite after plating (b) macroporous structure after toluene dissolving (c) cross sectional view revealed by FIB, the shaded feature is from FIB damage. Filled cracks are marked by arrows.

The filling of the cracks when copper was deposited in oxygen-free

environment approved the hypothesis that oxygen is critical to the dissolution behaviour. Coupled with an increase in the surface roughness, which is consistent with the discussion of the stress constraining geometry in Section 5.4.1.3.

5.4.3 Chemical composition

5.4.3.1 Phase identification

The crystallinity of the macroporous structure was examined using the X-ray diffraction. Figure 5-16 shows typical XRD patterns obtained from the as-prepared macroporous copper and silver copper films. A spectrum taking from ITO-coated glass substrate was added for comparison.

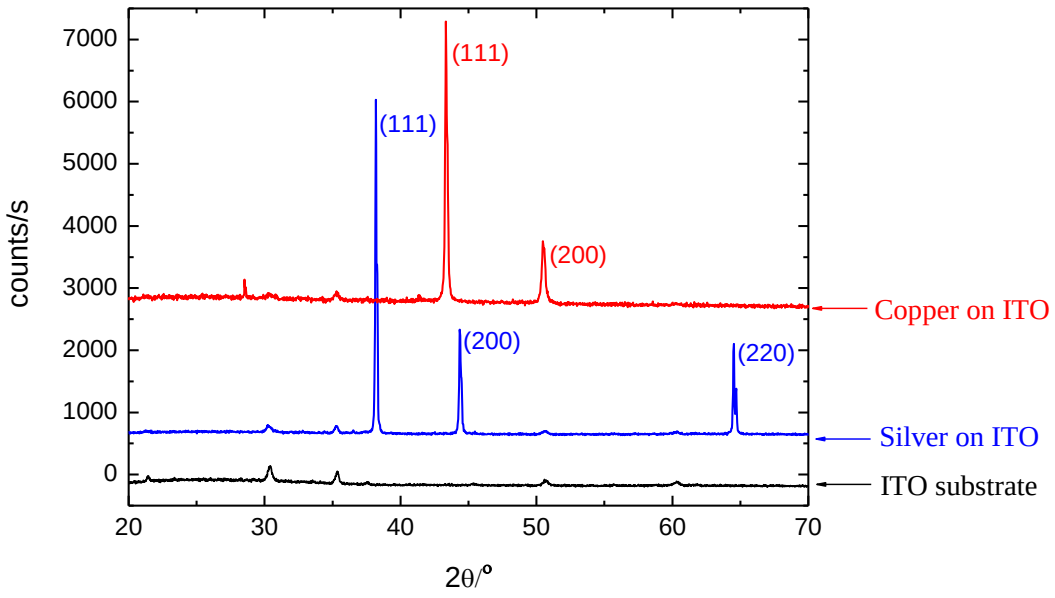

Figure 5-16 XRD patterns of electroplated 3-DOM copper and silver thin films.

The patterns show the characteristic reflections expected for highly polycrystalline structure with a face-centred cubic structure and a preferred (111) orientation. They are consistent with those obtained for non-templated films

electrochemically deposited under the same plating conditions. According to Scherrer formula, the grain size *d* is given by

$$d = \frac{0.9\lambda}{\delta_{hkl} \cos\theta_{hkl}} \quad \textbf{(5.28)}$$

where λ is the wavelength of incident x-rays, taken as a value of 0.154 nm , δ is the width of the peak at half maximum intensity of a specific phase (*hkl*) in radians, and θ is the center angle of the peak. From the width of the peaks (111) at half-maximum the calculated average grain size for copper and silver are 21.9 ± 0.4 nm and 21.6 ± 0.2 nm, respectively. Both sizes are an order of magnitude smaller than the pore diameters. In addition, the grain size of the silver is even significantly smaller than that of the ´´domains´´ shown in Figure 5-7(c). This confirms that the edges of the ´´domains´´ cannot be grain boundaries.

5.4.3.2 Oxidation

Oxidation is the main limitation of the application of macroporous metals. XRD patterns of old macroporous copper and silver structures are shown in Figure 5-17(a) and (b) respectively. The patterns were taken from the same sample at different time: as-prepared, one-month old, and one-year old, shown by the red, green and blue lines respectively. The pattern of ITO glass substrates is added for comparison. All structures display good crystalline order though both the macroporous copper and silver samples have been oxidized after a year, as indicated by the oxides peaks of Cu_2O and Ag_2O in Figure 5-17.

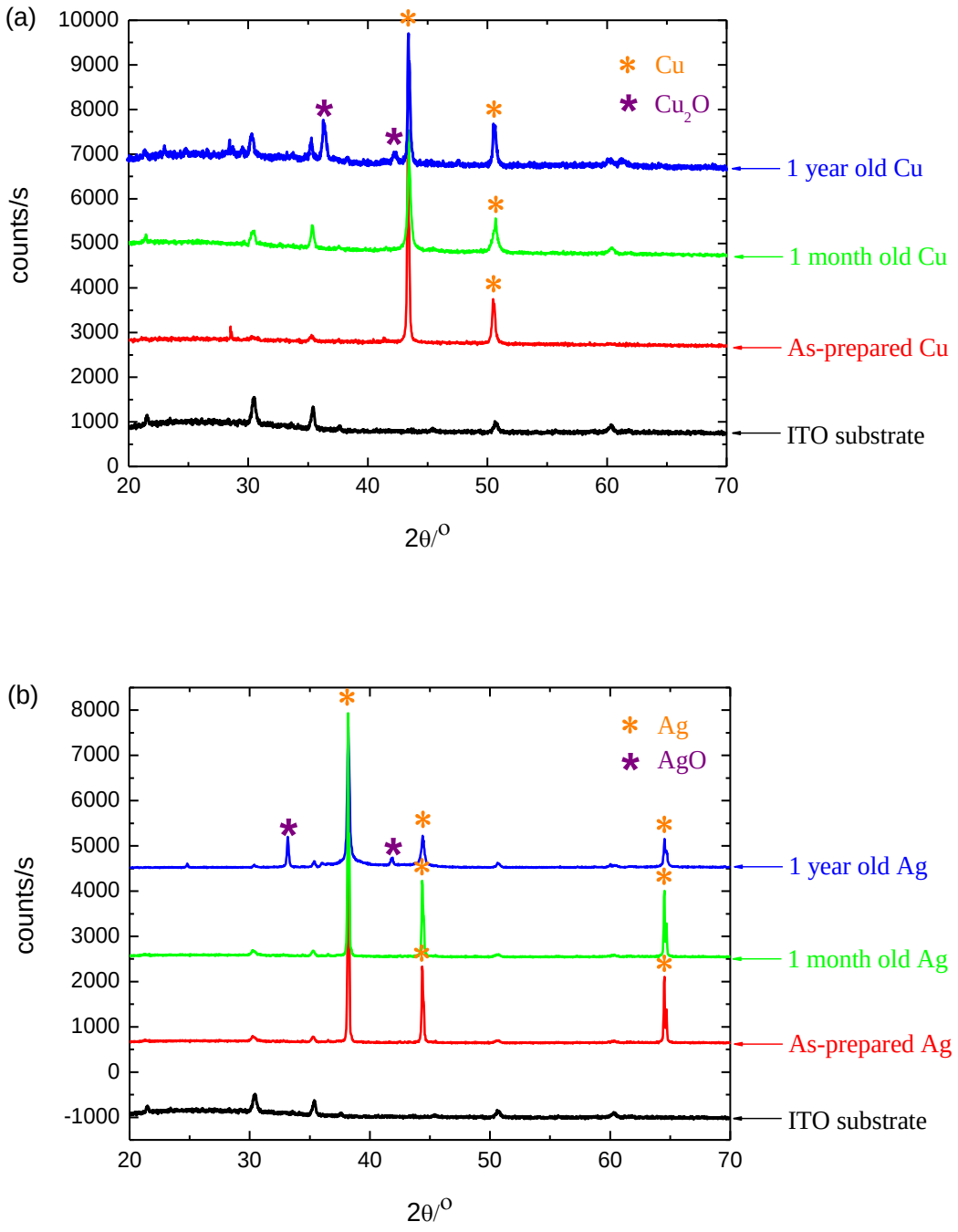

Figure 5-17 XRD patterns of the 3-DOM (a) copper and (b) silver, representing age oxidization.

EDX analysis has provided chemical examination closer to the surface and showed that the presence of oxygen in the one-month old macroporous samples, as shown in Figure 5-18. The EDX spectrum obtained from selected areas of either

copper or silver structures demonstrates the presence of oxygen. The gold peaks in the spectra Figure 5-18(b) & (d) are from gold-coating. The samples were coated by thin (5 - 10 nm) layers of gold prior analysis because the metal oxides diminished their conductivity. However, the oxidized structures may regenerated by low temperature (~ 250 ℃) annealing in hydrogen atmosphere [266,267].

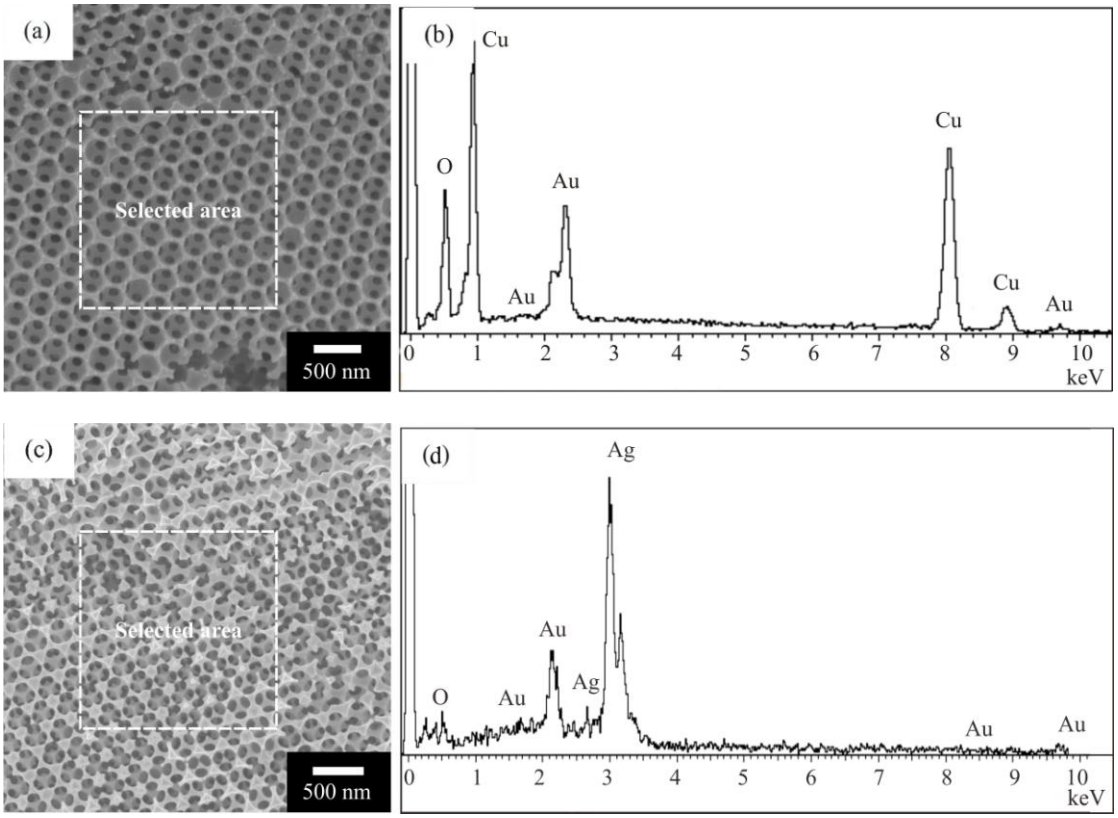

Figure 5-18 EDX analysis of a macroporous films showing presence of oxygen in the one-month old samples.

5.5 Electrochemical plating

5.5.1 Electrochemical response

Figure 5-19 shows voltage vs. time response obtained during the reduction of Cu^{2+} ions for the current densities varied from -3, -5, -8 to -12 mA/cm^2, referring to Figure 5-19. As soon as the current was applied, the reduction of copper ions directly

located at the bottom of the polystyrene template created a concentration gradient that caused a flux of ions towards the polystyrene template. In this process, the voltage exhibits a decrease less negative that is ascribed to the formation of the diffusion layer. Subsequently copper started to grow onto the interstices surrounding each sphere out through the template. At this stage, the voltage continues to decrease as the resistance that comes from the polystyrene template decreases.

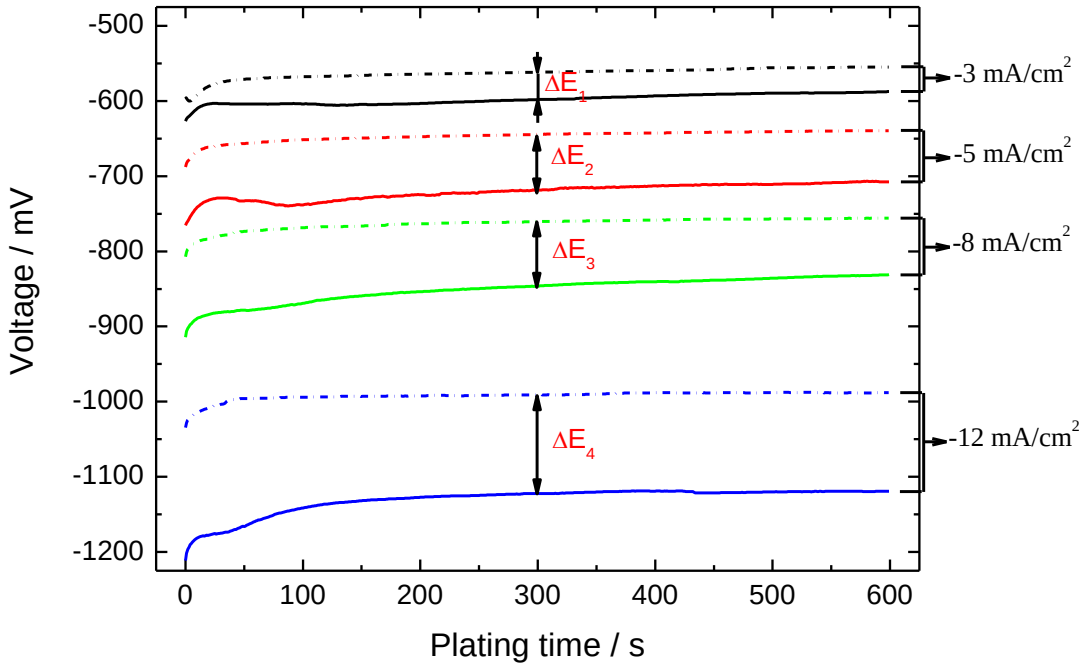

Figure 5-19 Voltage-Time responses for cupric ions reduction with various current densities from -3 mA/cm^2 to -12 mA/cm^2. Dashed and solid lines represent the responses for template masked or bare ITO-coated glass substrates respectively.

The Cu^{2+} ions were plated to both template masked and bare ITO-coated glass substrates for each current density and a fixed plating time 600 s. Corresponding E-T curves are shown by solid and dashed lines respectively in Figure 5-19. There are certain potential differences between the masked and bare substrates and they are increasing linearly with the current density, as shown in Figure 5-20. This

demonstrates that the potential difference comes from the resistance of the colloidal template.

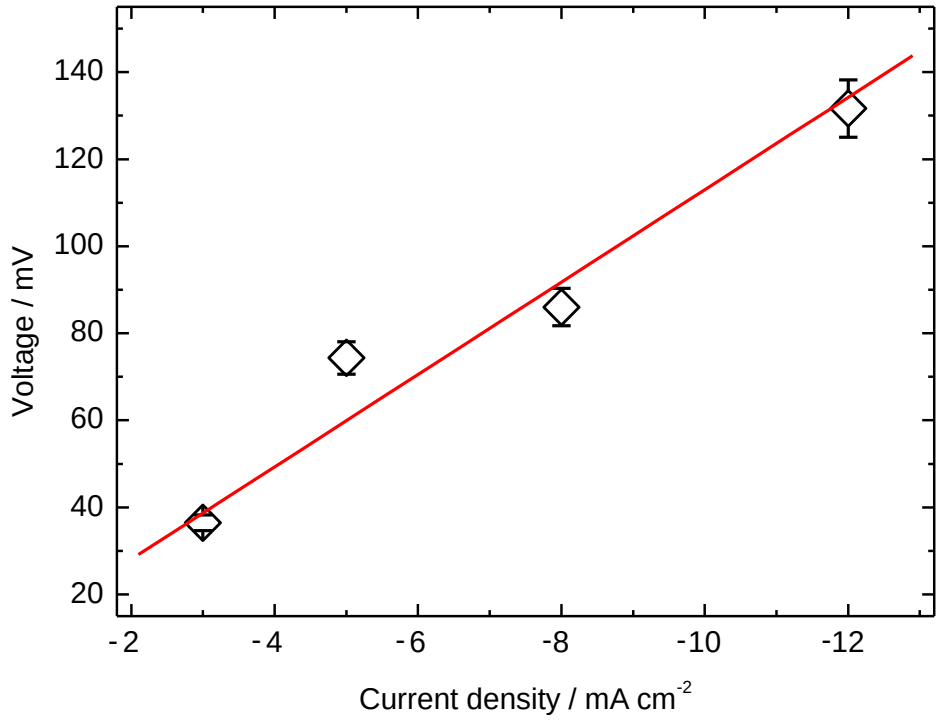

Figure 5-20 Linear fit for potential differences with respect to current density of electrochemical reduction of acid Cu^{2+}/Cl^- bath.

5.5.2 Faraday's law

Faraday's 1st law of electrolysis states that assuming 100% current density is achieved the mass of copper deposited (m) is proportional to the number of electrons that passes through:

$$m = \frac{M}{nF} \cdot Q \qquad \textbf{(5.29)}$$

where Q is the total electrical charge transferred, M is the molar mass of the metal, n is the valence number of the substance as an ion in solution (it is *2* for Cu^{2+} ions and 1 for Ag^+), and F is the Faraday's constant, *F=96,485* C/mol.

In galvanostatic depositions, Q is obtained from the deposition current (I) multiplied by the total deposition time (T):

$$Q = I \cdot T \tag{5.30}$$

and

$$m = \rho \cdot V = \rho \cdot S \cdot t \tag{5.31}$$

where ρ is the density of copper, S is the area deposited and t is the thickness of the copper film. Since only the voids between the polystyrene spheres are filled and the void density is 26% for an f.c.c array, we take 26% of the area exposed to the electrolyte as the effective deposit area S_{eff}. Therefore the film thickness can be calculated by:

$$t = \frac{MIT}{nF\rho S_{eff}} \tag{5.32}$$

As the deposit area S_{eff} for all samples is around 0.26cm^2, M is 63.55g/mol and ρ is 8.92 g/cm^3 for copper while 107.87g/mol and 10.49 g/cm^3 respectively for silver , the film thickness is determined by the deposition time and the current applied and the results are shown in Table 5-4.

Table 5-4: Predicted porous film thickness from Equation 5.32 (μm)

Time / *i*	Copper				Silver			
	100 s	**300 s**	**600 s**	**900 s**	**100 s**	**300 s**	**600 s**	**900 s**
1 mA/cm^2	0.14	0.42	0.84	1.26	0.41	1.23	2.46	3.69
2 mA/cm^2	0.28	0.84	1.68	2.52	0.82	2.46	4.92	7.38
3 mA/cm^2	0.41	1.23	2.46	3.69	1.23	3.69	7.38	11.07
5 mA/cm^2	0.69	2.12	4.27	6.38	2.05	6.15	12.30	18.45
10 mA/cm^2	1.38	4.24	8.54	12.76	4.10	12.30	24.60	36.90

5.5.3 Current density

Our experiment suggested low current densities would result in incomplete filled surfaces. Figure 5-21 are representative SEM images of macroporous copper films grown from copper glycerol solution with increasing current densities, from -0.5 mA/cm^2, -2 mA/cm^2, -3 mA/cm^2, to -5 mA/cm^2, with a constant deposition time of 900s.

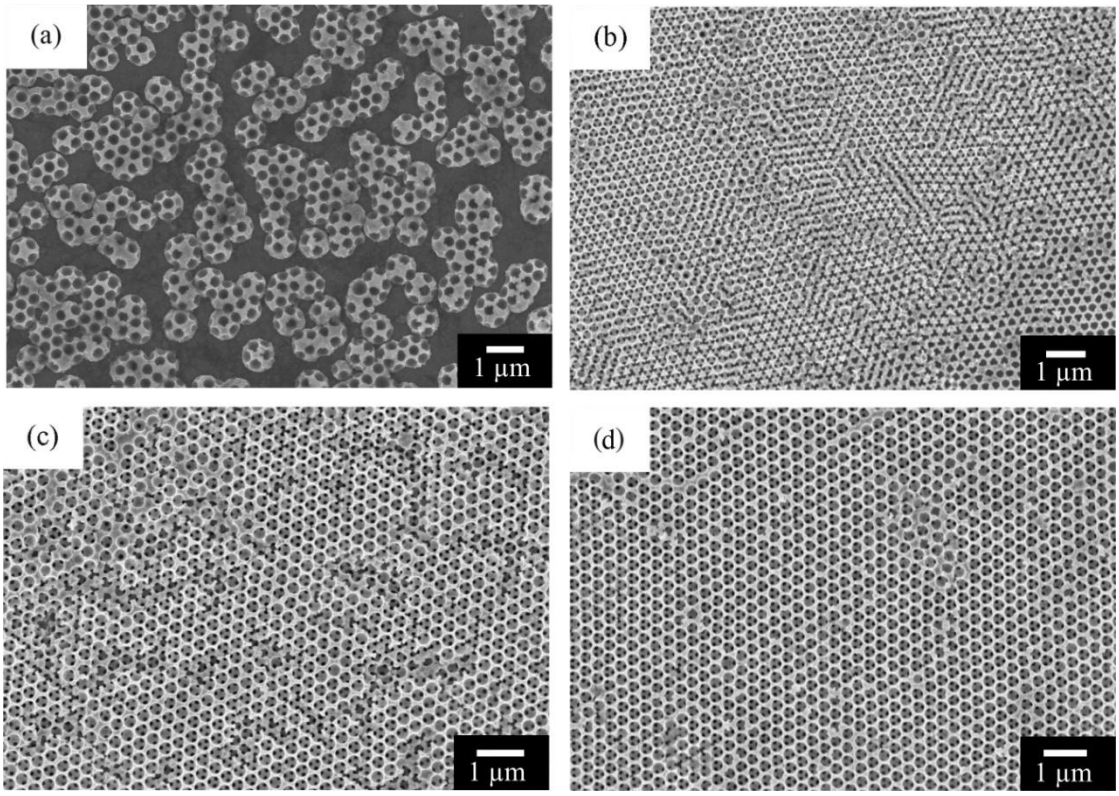

Figure 5-21 Surface view of macorporous copper films plated from various current densities (a) -0.5 mA/cm^2 (b) -2 mA/cm^2 (c) -3 mA/cm^2 (d) -5 mA/cm^2.

At the lowest current density of -0.5 mA/cm^2, we can see a number of randomly distributed nearly hemispherical structures, each punctuated by arrays of sphere pores, as shown in Figure 5-21(a). It demonstrates the numerous nucleation sites were initiated randomly all over the plating area. The pore centre-to-centre distances match the diameter of the original polystyrene spheres. As the current density increases, the hemispherical porous structures grow larger and approach to

overlap each other. Eventually completely overlapped when the current density is -5 mA/cm^2, as shown in Figure 5-21(d), a flat and smooth surface has obtained.

5.5.4 Plating time

To effectively control the thickness of the films, one needs to know the actual growth rate other than the theoretical predicted by Faraday's 1st law. To determine this, depositions were performed with a constant current density of -5 mA/cm^2 but various deposition times from 100 seconds to 900 seconds. Since it is hard to directly measure the thickness of the films with SEM, the film thickness was estimated by counting the number of the layers. For instance, the copper thin films grown with a current density of -5 mA/cm^2 but plating time varied from 100 s, 300 s, 600 s to 900 s resulted in monolayer, 7 layers, 13 layers and 20 layers, respectively, as shown in Figure 5-22. The SEM counted number of layers are summarized in Table 5-5. Since the structures are of f.c.c lattice, the theoretical number of layers, *N*, can be calculated by

$$N = \frac{2\sqrt{3}}{3}\left(\frac{t}{D} - 1\right) + 1 \qquad \textbf{(5.33)}$$

where *t* is the thickness of the plated film and *D* is the void diameter, which is comparable to the diameter of the polystyrene spheres. Therefore the theoretical number of layers of the macroporous films are determined and shown in Table 5-5.

From Table 5-5, the experimental results are smaller than the theoretical calculation results because the latter was obtained with an assumption of 100% deposition efficiency. Plotting the number of layers versus the plating time and the lines are the best-fit results using a linear function, as shown in Figure 5-23.

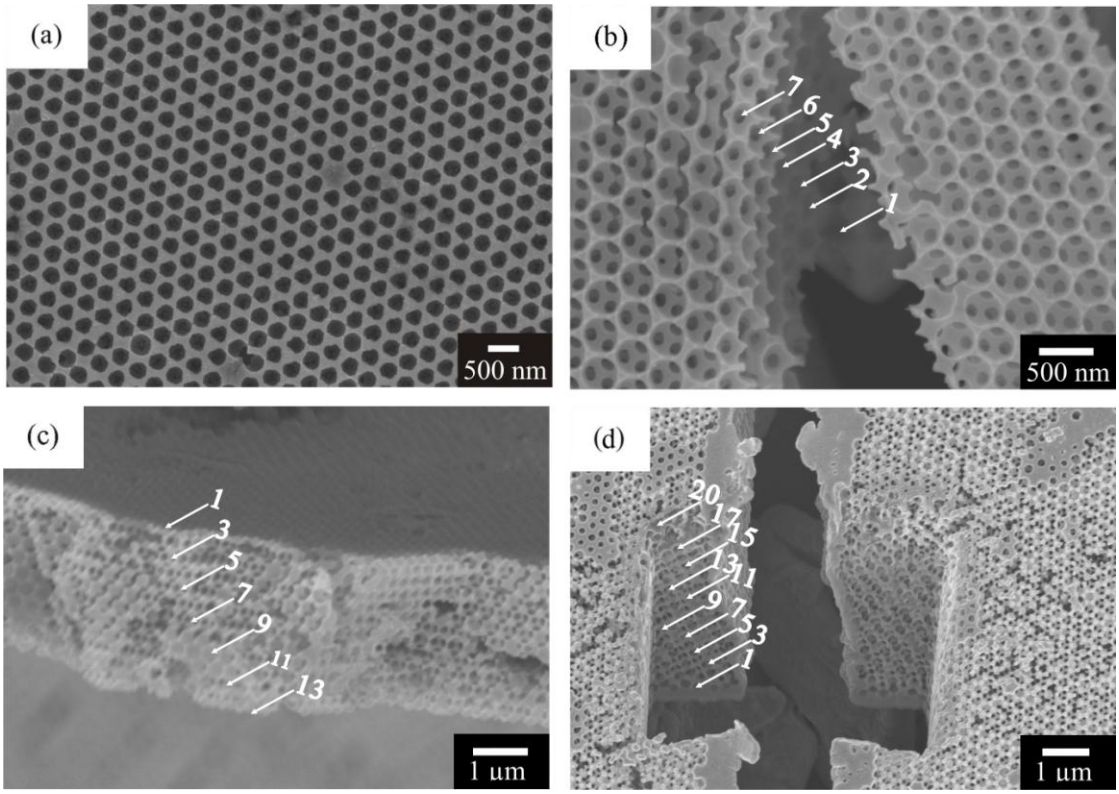

Figure 5-22 SEM images of macorporous copper films plated from constant current density *i* = -5 mA/cm^2 but increasing plating time (a) 100 s (b) 300 s (c) 600 s (d) 900 s.

Table 5-5: Number of layers of macroporous copper films at current density *i* = - 5 mA/cm^2

Time/s	Theoretical thickness /µm	Theoretical number of layers			Experimental number of layers		
		258nm	327nm	651nm	258nm	327nm	651nm
100	0.69	4	2	1	2	1	1
300	2.12	9	8	4	6	6	2
600	4.27	19	16	7	15	13	4
900	6.38	28	23	11	23	20	7

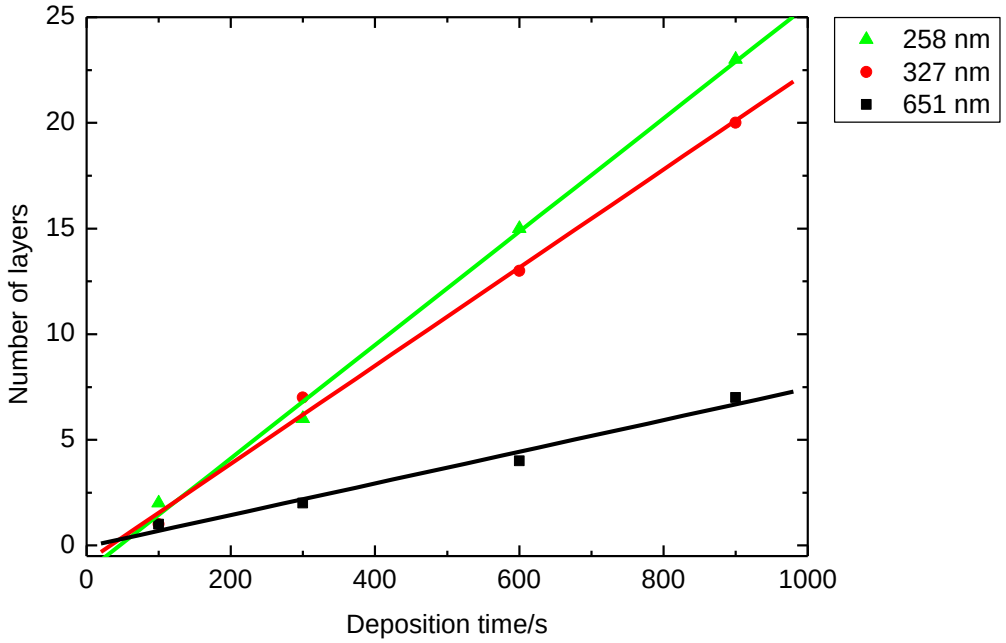

Figure 5-23 Dependence of number of layers of copper films vs. plating time.

However for the crack-filled films, it is hard to tell the number of the layers of the films due to the high surface roughness. As illustrated the Zygo images in Figure 5-24, the surface roughness could reach tens of microns.

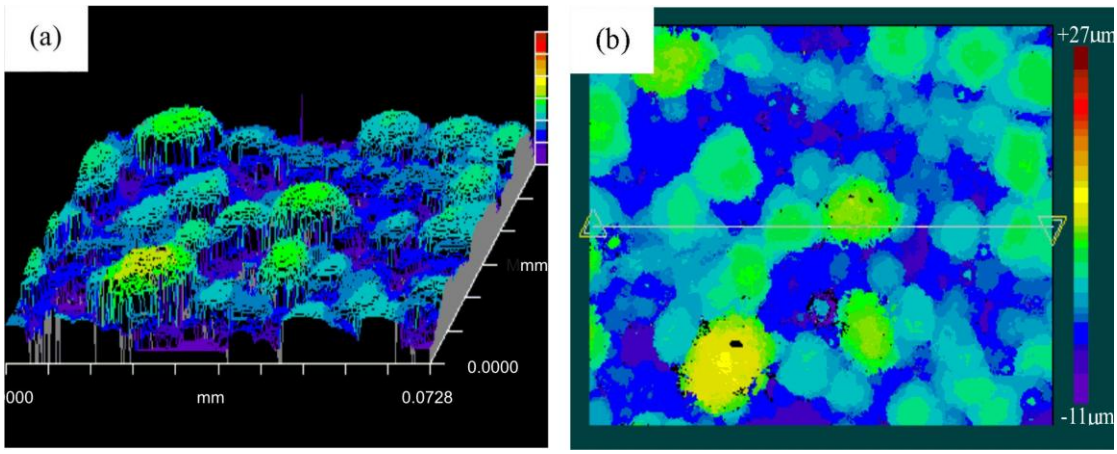

Figure 5-24 Zygo interferometer images reveal high surface roughness of crack filled films.

5.6 Optical properties

Figure 5-25 is a series of reflectance spectra obtained from a bulk copper film electroplated on a bare ITO glass slide. As expected, the continuous film does not display any stop band properties at all.

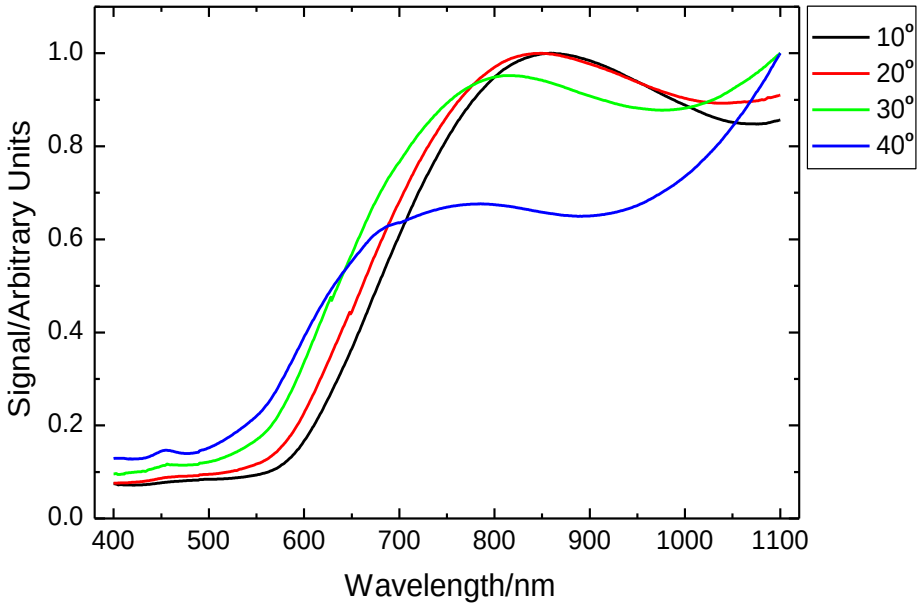

Figure 5-25 Reflectance spectra of a dense copper film prepared with current density *i* = -5 mA/cm^2 and plating time t = 600 s.

5.6.1 Metal dependence

Measurement of the reflectance spectra of the inverse copper and silver films in the visible length range are shown in Figure 5-26, along with the spectra obtained from the polystyrene template for comparison. The incident angles were varied from 10 °to 50 °. All spectra have been background-subtracted and normalised. The peaks correspond to multiple Bragg reflections arising from the ordered structures. When the wavelength of incident light satisfies the Bragg condition, it is diffracted away from the propagation axis, leading a peak in the reflectance spectrum. The reflectance peaks are shifted to shorter wavelength region, which could be due to the decrease of either the pore centre-to-centre distance or the refractive index.

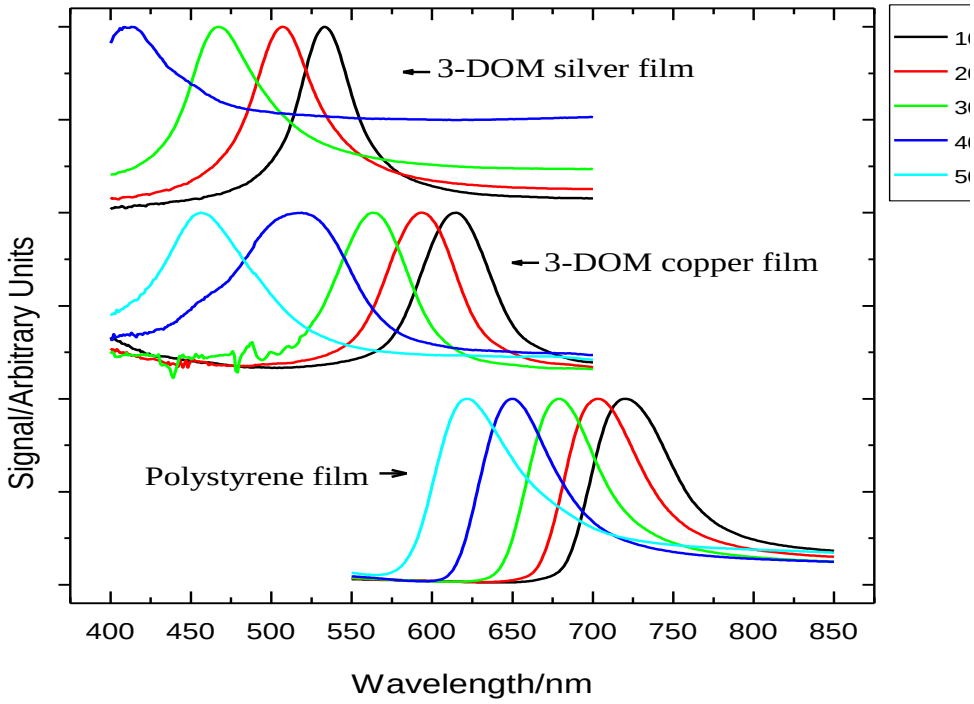

Figure 5-26 Reflectance spectra of the 3-DOM copper and silver films (templating sphere size D = 327 ± 6.0 nm), showing reflectance peaks correspond to stop bands arising from the periodic modulated structure.

An approximate estimation for the pore sizes of the inverse films can be obtained from the combining Bragg's law and Snell's law (Equation 3.3) demonstrating the position of the peak is determined by the sphere diameter and the effective refractive index. Plotting $sin^2\theta$ vs λ^2 gives a straight line in good agreement with the experimental data, as shown in Figure 5-27. This is consistent with long range order in both the template and macroporous structures.

The diameter of the colloidal particles is calculated as 344 ± 2 nm and the void sizes are 336 ± 2 nm and 333 ± 3 nm for copper and silver respectively. This indicates that volume shrinkages are not more than 4%, which is consistence with the measurement of SEM sizing. In contrast, metals grown from nanoparticle infiltration

have shown shrinkages of up to 30% [36,196,268]. Since the void sizes are approximately the same as that of the original polystyrene spheres, the shifts of the reflectance spectra are due to the material properties: the peaks shift to shorter wavelength is actually due to decreases of the effective refractive index, as shown in Table 5-6.

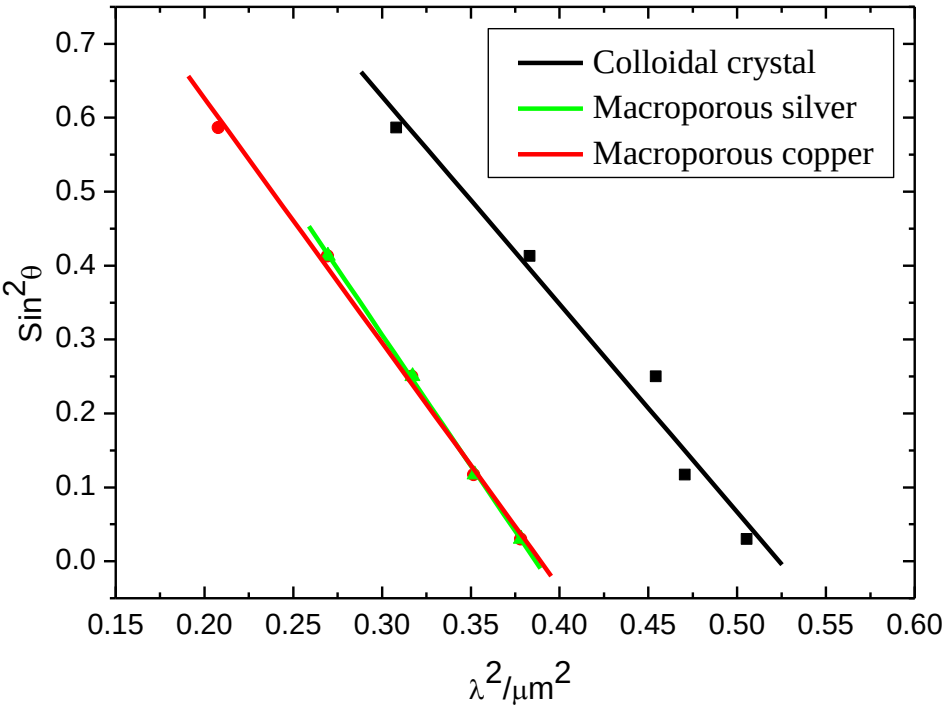

Figure 5-27 Linear fits for the reflection peaks in Figure 5-26.

Table 5-6: Lattice space and effective refractive index calculated by the reflectance spectra

Films	Lattice space D_1 /nm	SEM determined void size D_2 /nm	Effective refractive index n_{eff}
Polystyrene	344 ±2	327 ±6.0	1.28
Inverse copper	336 ±2	315 ±15	1.14
Inverse silver	333 ±3	314 ±17	1.00

5.6.2 Film thickness dependence

Reflectance spectra were investigated on the 3-DOM metallic films with increasing thickness, as shown in Figure 5-28. The copper thin film grown with the constant current density of -5 mA/cm^2 but increasing plating time from 100s, 300s, 600s, to 900s. The number of layers of the films are 1, 6, 13, and 20 respectively. As the monolayer structure diffracts less light, it fails to display any angle-resolved peaks. The other three thin films show stop-band properties over the wavelength range from 450 nm to 650 nm and there is no any significant difference between the three sets of reflectance spectra. It demonstrates momolayer porous structure is not sufficient to display any stop-bands but when the film thickness exceeds a couple of layers, further increasing of the thickness will not enhance the stop-band properties.

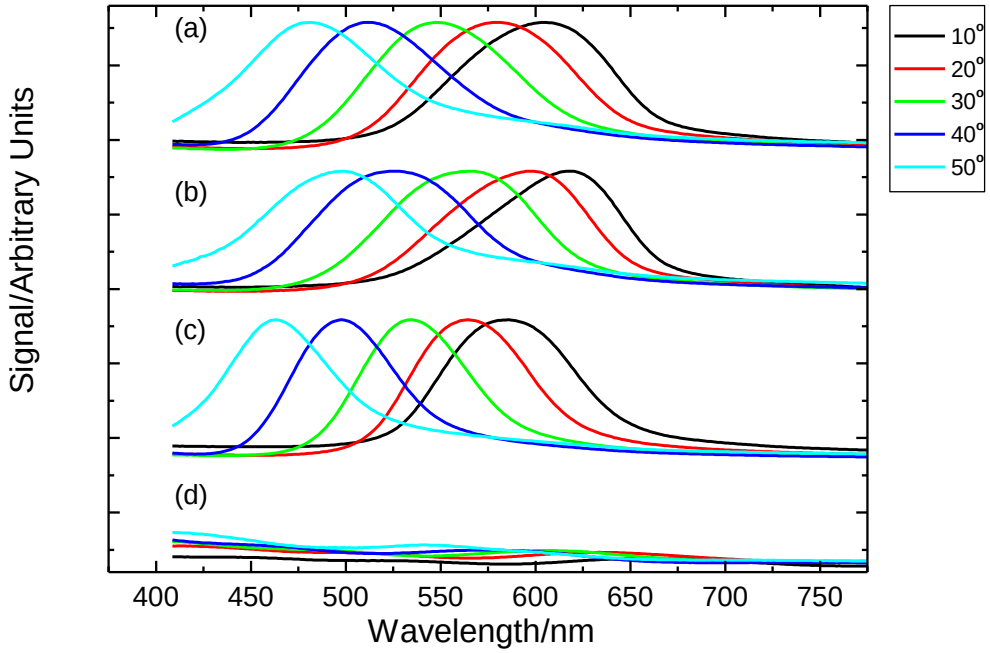

Figure 5-28 Reflectance spectra of the 3-DOM copper films (templating sphere size D = 327 ± 6.0 nm, current density *i* = -5 mA/cm^2) of plating time (a) 900 s, (b) 600 s, (c) 300 s and (d) 100 s.

5.6.3 Void size dependence

The position of the reflection peaks is thus determined by the void size. Since in a face-centred cubic structure, the void diameter D is determined by

$$D = \sqrt{\frac{3}{2}} d_{hkl} \tag{5.34}$$

and the combining Bragg's law and Snell's law stated [221,222]

$$\lambda = 2 d_{hkl} \sqrt{n_{eff}^2 - \sin^2 \theta} \tag{5.35}$$

Thus

$$\lambda = 2\sqrt{\frac{2}{3}} D \cdot \sqrt{n_{eff}^2 - \sin^2 \theta} \tag{5.36}$$

where d_{hkl} is the lattice constant or the distance between two diffracting (hkl) planes, θ is the angle of the incident to the normal surface, λ is the peak wavelength, and n_{eff} is the effective refractive index of the structure.

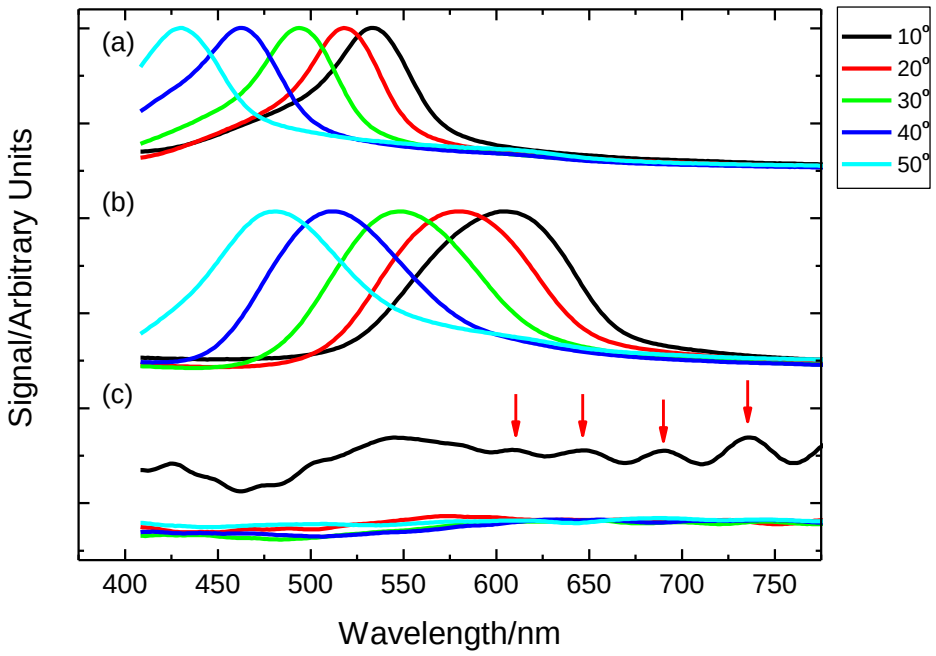

Figure 5-29 Reflectance spectra of the 3-DOM copper films of templating sphere size (a) 248 ± 5.7 nm, (b) 327 ± 6.0 nm, and (c) 651 ± 23.4 nm.

Reflectance spectra were taken over the thin films template by all the three sphere size of 248 nm, 327 nm and 651 nm, which are shown in Figure 5-29. The macroporous copper films grown from 248 nm and 327 nm templating spheres showed angle-solved peaks in the visible range and they have band width ranging from 400 to 550 nm, and from 450 to 650 nm respectively. The porous film template by 651 nm polystyrene spheres doesn't display any reflection peaks in the visible range however it has the trend to show the band in the infrared range, as Febry-Perot fringes are observed (marked by red arrows in Figure 5-29) from the spectrum at incident angle of 10 ?.

5.7 Preliminary SERS measurements

5.7.1 Dye dependence

The performance of the 3-DOM metallic films as SERS substrates was evaluated by using common dyes rhodamine 6G (R6G) and benzotriazole (BZT) as probe molecules. Figure 5-30 gives the chemical formulas of the R6G and BZT, in which the R6G consists of two chromophores, a dibenzopyrene chomophore (xanthene), and a carboxyphenyl group and the BZT molecule contains a triazole ring and a benzene ring. The R6G adsorbs to the surface through physical adsorption but the BZT chemisorbs to the metallic surfaces. This binding process is irreversible and the dyes should displace any surface species bound to the surface ensuring a good Raman signal. For comparison, spectra from R6G and the BZT dye were initially taken using silver colloid prepared through the standard Lee and Meisel preparation technique [143,144] and are shown in Figure 5-31. The colloids produced from this technique have a mean size of 60 nm [149]. All measurements were taken using the 633 nm He-Ne laser excitation with the ×50 objective and 0.5 mW at the focal point.

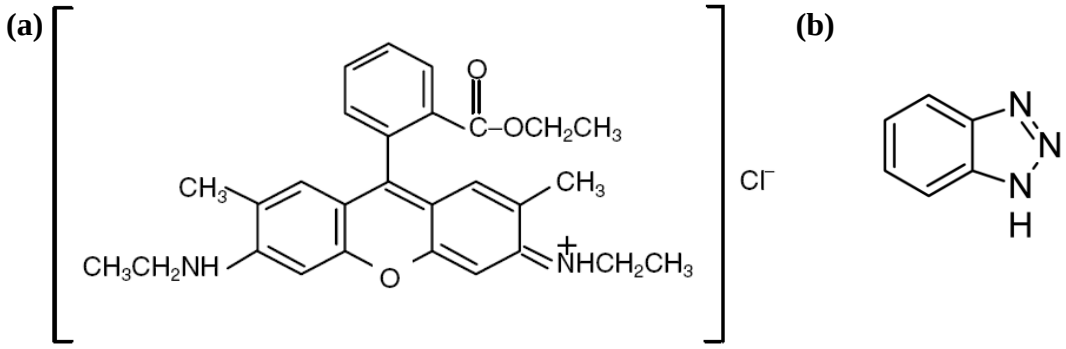

Figure 5-30 Chemical formulas of analytes (a) rhodamine 6G and (b) benzotriazole.

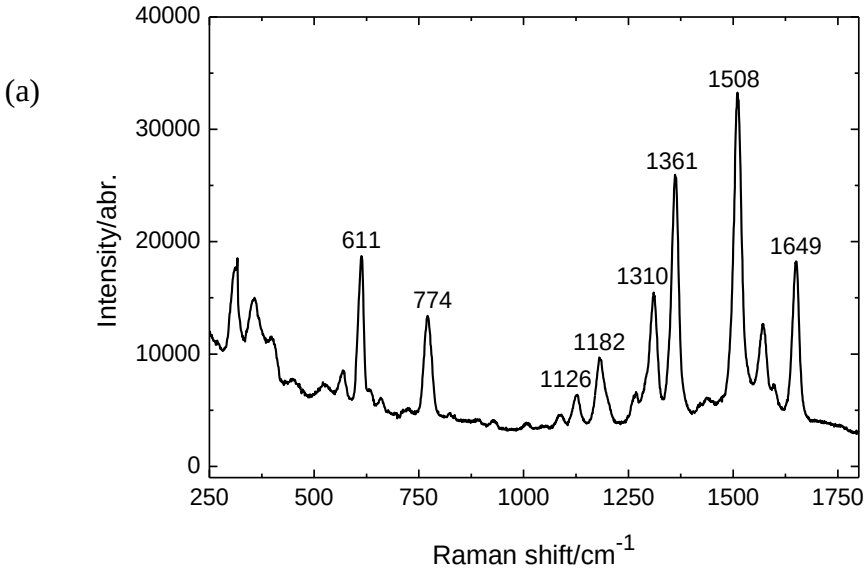

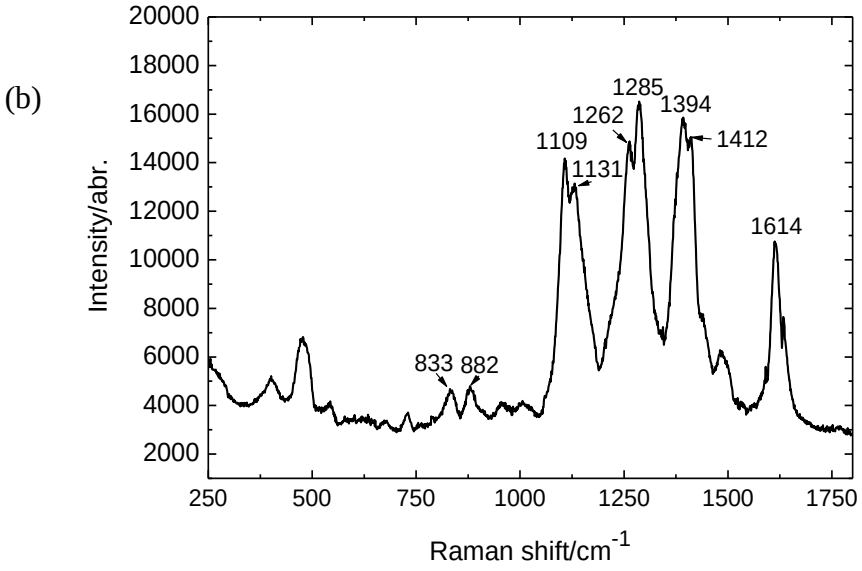

Figure 5-31 Reference spectra of (a) R6G and (b) BZT taking using silver colloid using 633 nm laser excitation.

In Figure 5-31(a), the band at *ca.* 633 cm^{-1} is assigned as in-plane bend of the xanthene ring [269]; the band at *ca.* 774 cm^{-1} is assigned to the C-H out of plane bending mode; the band at *ca.* 1126 cm^{-1} is due to the C-H in-plane bending mode; those at *ca.* 1361, 1508, 1649 cm^{-1} come from the C-C stretching modes of aromatic benzene rings [270,271]. In Figure 5-31(b), the band at *ca.* 833 cm^{-1} is assigned to the benzene ring breathing mode; the one at *ca.* 1109 cm^{-1} is N-H in-plane bending mode; the one at *ca.* 1285 cm^{-1} is C-H in-plane bending mode; the one at *ca.* 1394 cm^{-1} is triazole ring stretching mode, the other one at *ca.* 1614 cm^{-1} is from benzene ring stretching mode [272,273].

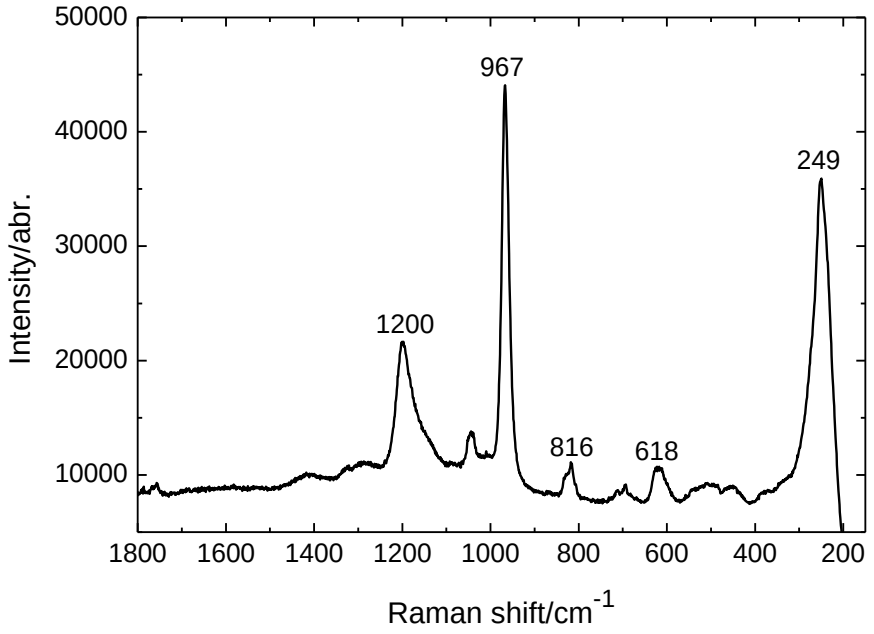

Figure 5-32 Background Raman spectrum taking using macroporous silver film grown from silver thiosulfate solution using 633 nm laser excitation.

Extensive measurements were taken for R6G from the surfaces of the silver films prepared from silver thiosulfate solution but only intermittent and extremely weak signals were observed. Background measurements obtained from silver films that have not been exposed to any analyte displayed strong Raman signals, as shown

in Figure 5-32. The spectrum corresponds to the Raman response of non-adsorbed $S_2O_3^{2-}$ ions [274] and the peaks from right to left are corresponding to symmetric S-S stretching, asymmetric S-O bending, symmetric S-O bending, symmetric S-O stretching, and asymmetric S-O stretching modes respectively. This suggests that surface coverage of sulfate species will prevent the adsorption of R6G or BZT to the surface and hence the macroporous silver films in the following measurements had to be prepared from the silver perchlorate solution in order to eliminate the disturbance of $S_2O_3^{2-}$ ions.

5.7.2 Metal dependence

Though silver is the best SERS active material, Raman signals may detectable on structured copper substrates. Figure 5-33 shows a Raman spectrum taking from 3-DOM copper thin films using BZT as the target molecule. The spectrum taking from silver colloids has been added for comparison. Though the intensity may disadvantageous for detecting tiny concentration of a target compound by SERS, the 3-DOM copper film is inexpensive to fabricate. In our measurements however, the 3-DOM copper failed to give reproducible results. Oxidation is a common reason for SERS activity reduction but in our case, as presented in Section 5.4.3.2, the macroporous copper suffers minor oxidation and is relatively stable in air. Further investigation needs to be taken to find out the instability of SERS arising from the 3-DOM copper.

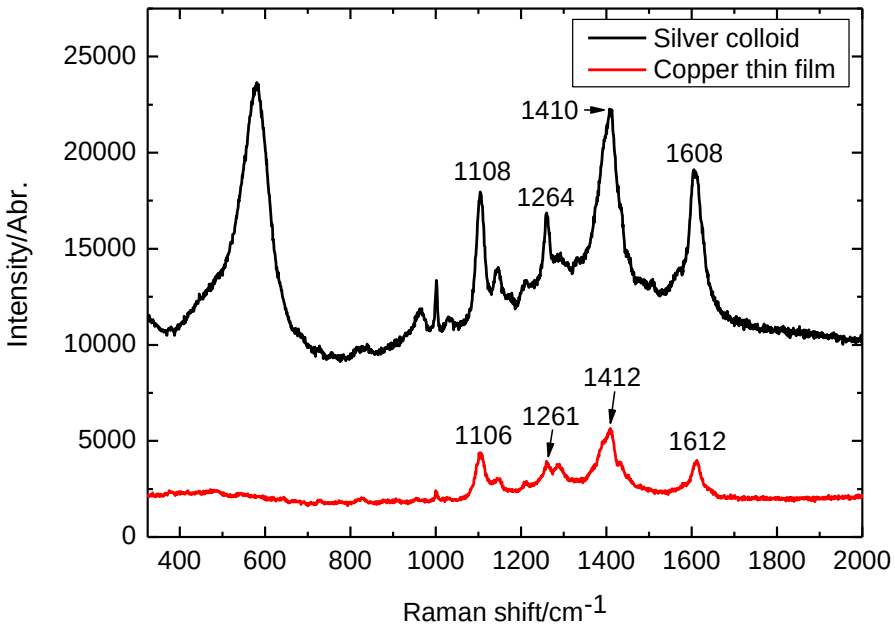

Figure 5-33 Raman spectra taking from 3-DOM copper thin film and silver colloids using BZT as target molecule and 633 nm laser excitation.

5.7.3 Void size dependence

SERS spectra of BZT taking using macroporous silver films inverted from polystyrene spheres of diameters 248 nm, 327 nm and 651 nm are shown in Figure 5-34. The Raman intensities of the three dominating vibrational modes at ca. 1105, 1268, and 1415 cm^{-1} increase with increasing diameters of the polystyrene spheres and the largest signals were obtained from the films prepared with the 651 nm templating spheres. When the void size increases, the electrical field potential around each void increases, which is known to be beneficial for an electromagnetic enhancement. This agrees very well with size-dependent Raman enhancement in 2-D silver porous arrays or metallic colloids [91,132,275]. We have collected series of SERS spectra from different points on each sample and the intensities are highly reproducible. It should also be noted that larger void size corresponds to higher

coverage of molecular in the void, resulting in a higher Raman enhancement. Subsequent experiments were performed on the 651 nm void size because of its highest signal intensity.

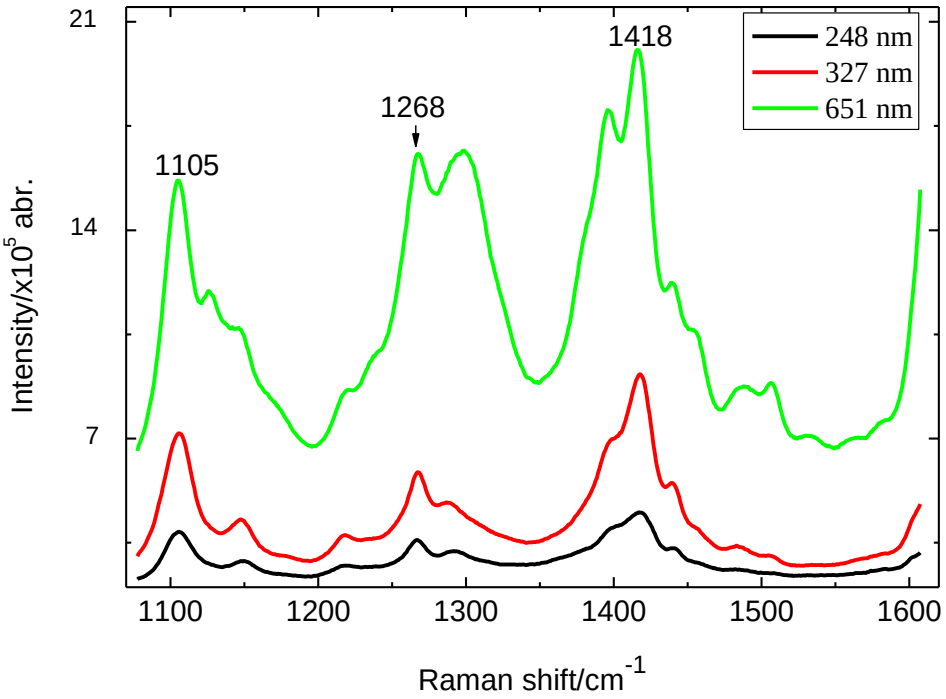

Figure 5-34 Raman spectra from benzotriazole taking using macroporous silver using 633 nm laser excitation.

5.7.4 Dye concentration dependence

To investigate the dependence of the SERS signal intensity with dye concentration, data were collected from films of the same thickness treated with different concentrations of benzotriazole. Figure 5-35 shows the average spectra obtained from films prepared with a deposition time of 1200 s treated with BZT of concentration of 0.10, 0.25, 0.75 and 1.00 μM for 30 min each. The films were subsequently rinsed with ethanol to remove all molecular that was not bounded. There are significant changes to the sharpness of the spectral features and the background

with changing concentration.

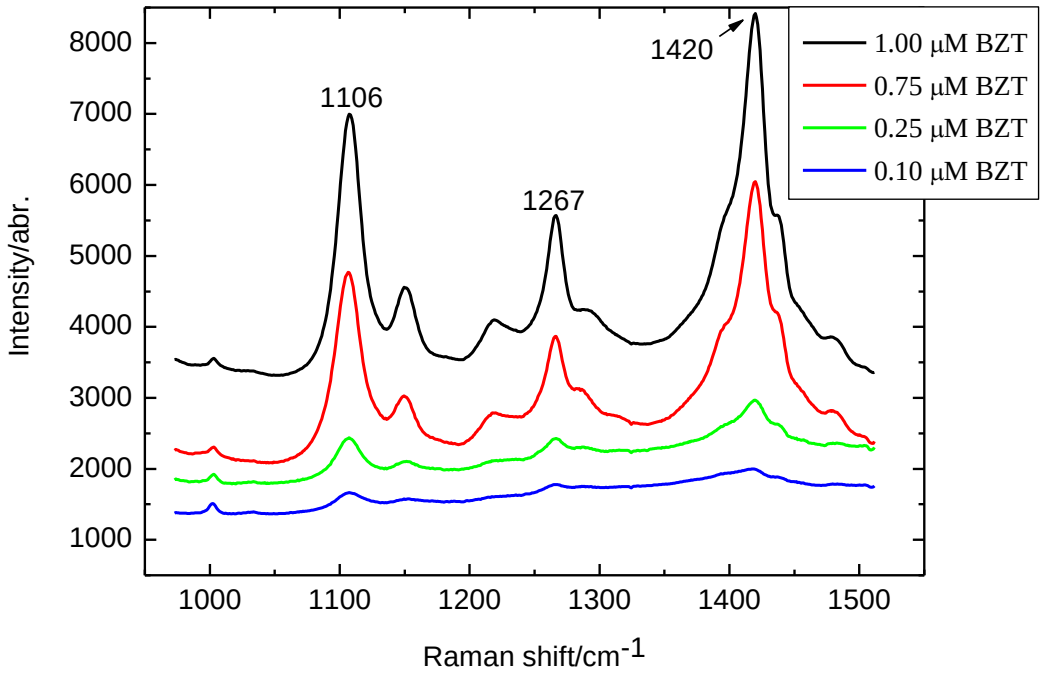

Figure 5-35 Raman spectra from increased BZT concentration taking using macroporous silver using 633 nm laser excitation.

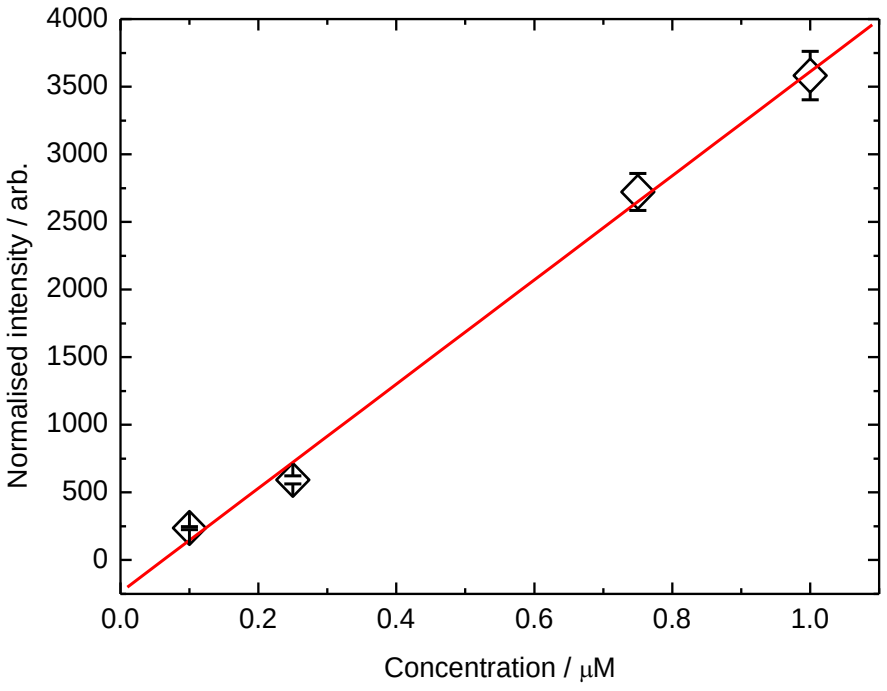

Figure 5-36 Dependence of the Raman intensity on the dye concentration.

By fitting the most resolved spectral feature it is possible to extract a concentration isotherm for the surfaces, as illustrated in Figure 5-36. The isotherm appears to be as expected although further measurements on surfaces prepared with more dye concentrations are required in order to confirm this.

5.7.5 Film thickness dependence

To evaluate the efficiency of the enhancement as a function of the thickness of the film, the measurement were taken using films prepared with a current of -2 mA/cm^2 for individually 600, 1800, 2400 and 3600 s. The resulting films were treated with BZT of concentration of 1.00 μM for 30 min and then rinsed with ethanol to remove all unbound molecular.

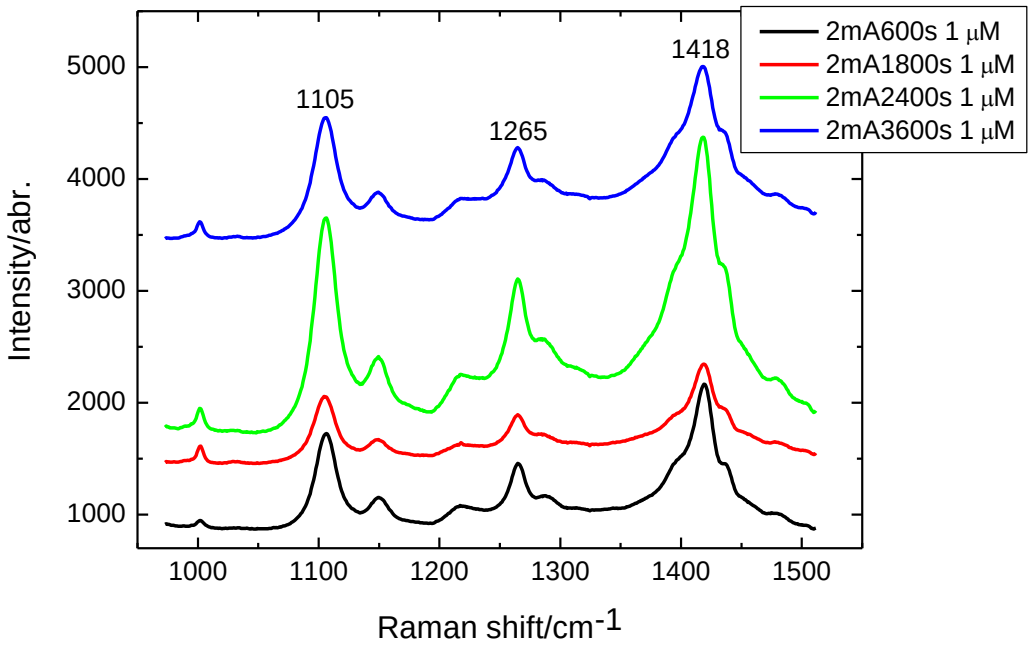

Figure 5-37 Raman spectra from BZT taking using macroporous silver with increasing plating time/film thickness using 633 nm laser excitation.

It appears that the maximum enhancement occurs for films that have been prepared with a 2400 second deposition time, as shown in Figure 5-37. This is correlated to the SEM images in Figure 5-11, in which the thin film plated by 2400s shows the best order but it has become disordered when the plating times reached 3600 seconds. Since the periodicity should be a significant factor of the SERS enhancement [121,158,160,276], the variation of the intensity shown in Figure 5-38 is most likely contributing to the periodicity of the structure and the film of the highest periodicity has performed the best while using as the SERS substrate.

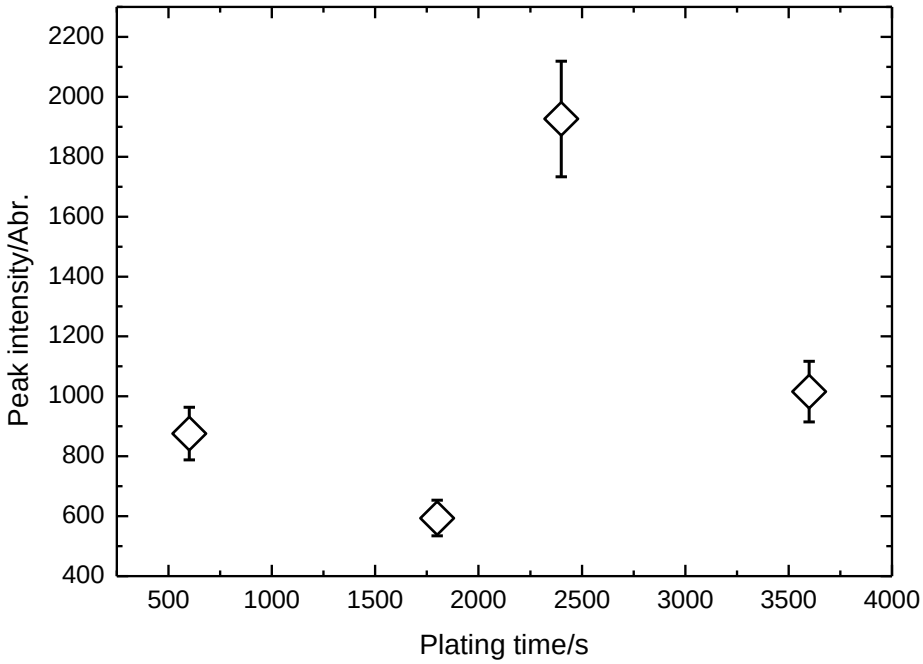

Figure 5-38 Dependence of Raman intensity on the macroporous film thickness using 1105 cm^{-1} peak.

However the film roughness may be reduced through modifying the bath solution with certain additives, which help distribute nucleation rate evenly at all sites. Though it has been reported that the thickness of the film couldn't be a major factor [121,156] because only the molecules in the top layer will be illuminated by the

excitation laser and hence contribute to the Raman signals. Most work on SERS to date are using monolayer nanostructures [72,128,152,157], however further work on their performance over the film thickness might be interesting.

5.8 Chapter summary

Electrochemical plating has been demonstrated for the preparation of highly ordered, three-dimensional macroporous copper and silver network. They were exactly the inverse replicas of the original polystyrene films, consisted of spherical voids arranged in face-centred cubic lattice on the metal matrices. The diameter of the spherical voids could be controlled by the choice of the diameter of the polystyrene particles used to prepare the template. Reverse to the close packed colloidal sphere domains divided by drying cracks, the inverse silver film was consisted of macroporous domains joint by dense solid metal whilst in the copper films the interstitial spaces between the colloidal spheres were infiltrated but the drying cracks between the domains were remain. The electrochemical plating process has been discussed and we found that limited diffusion of oxygen was responsible for the preservation of drying cracks.

XRD has given the composition and the crystal structure and the crystalline grain size. Both silver and copper macroporous structures displayed good crystalline though presented oxidation after a year. Preliminary studies of the optical properties revealed that the resulting macroporous films have stop band properties in the visible wavelength range consistent with variation in the effective refractive index of the films. While using chemically adsorbed BZT are used as target molecules. Primary experimental results showed that the porous silver nanostructured films are highly desirable for detection of molecules bases by SERS technique in terms of high Raman

intensity enhancement. The Raman intensity was proportional to the concentration of the dye. However further tests are required to make sure that the results are reproducible. Also, despite there did not appear to be possible significant variation in the signal intensity with the thickness of the film, measurements from a greater range of film thicknesses are required to confirm this.

6 CONCLUSIONS AND FUTURE WORK

This chapter presents the overall conclusion of the thesis and a discussion on possible directions of future work.

6.1 Thesis conclusion

The research on the 3-DOM metals described in this thesis was motivated by their prospective applications in photonics and plasmonics. The design and fabrication of sub-micron 3-DOM materials involved the creation of a periodic lattice of colloidal crystals through convective self-assembly, the infiltration of the colloidal crystals with metals electrochemically reduced from corresponding electrolytes, and subsequent the removal of the colloidal templates. In previous chapters, experimental results on the three-dimensional highly ordered macroporous metals grown using this template-directed electrochemical deposition have been described. The microstructure and optical properties of the 3-DOM silver and copper thin films have been examined using optical microscopy, scanning electron microscopy, optical reflectance spectroscopy. The application of the 3-DOM metals as SERS-active substrates have been evaluated using surface enhanced Raman spectroscopy. The main results of this thesis are summarised below.

6.1.1 Templating film growth

The polystyrene nanoparticles were made by emulsion polymerization of styrene monomers, in which the variation in mean diameter has been realized by

tuning the concentration of the monomer. Large area colloidal crystals made of monodisperse polystyrene spheres have been prepared through evaporation-induced self-assembly. Parameters that influence the crystallinity and quality such as the film substrate, sphere polydispersity, growth temperature and relative humidity of the suspension have been studied individually. Continuous and uniform thin film has been obtained on surfactant-modified indium tin oxide (ITO) coated glass substrate and highly ordered colloidal crystals were obtained at controlled growth temperature and relative humidity.

The periodicity of the colloidal crystal has been confirmed by SEM images, and further by the sharp spot array of the fast Fourier transforms (FFTs) and the reflectance peaks arising from multiple Bragg refractions. It has been concluded that the polystyrene arrays were long-range ordered close-packed arrangement in both parallel and perpendicular directions to the glass substrates. In addition, the thickness of the colloidal thin film has been tuned by varying the column fraction of the colloidal suspensions and a linear function between the film thickness and the volume fraction has been achieved when the volume fraction was over 0.05 %.

6.1.2 3-DOM metal growth

Noble metals copper and silver have been electrochemically deposited from solutions of copper sulfate, silver thiosulfate, and silver perchlorate. Galvanostatic deposition was chosen to reduce metals at a constant rate. The resulting metallic macroporous structures inverted the topography features of the colloidal crystals. They were consisted of highly ordered spherical voids embedded in metallic matrices. The void size was determined directly by the sphere diameter of the colloidal crystal templates. The shrinkage of the resulting porous structure was negligible after

template removal, which preserved the periodicity extended over large spatial scale. The thickness of the macroporous copper films has been found linear to the plating time at a constant current density for all templating sphere sizes. However, for the cracked filled structures, it was unlikely to measure the film thickness due to their high surface roughness in micron sizes.

Oxidation of both of the macroporous copper and silver thin films have been studied by X-ray diffraction and energy-dispersive X-ray analysis. All fresh samples displayed good crystalline but oxides peaks presented in those were more than one month old. However, the metals could be regenerated through low temperature annealing in hydrogen atmosphere to restore their activity in applications.

6.1.3 Surface morphology

In contrast to the close packed colloidal sphere domains divided by drying cracks, the inverse silver film consisted of macroporous domains joined by dense solid metal whilst in the copper films the interstitial spaces between the colloidal spheres were infiltrated but the drying cracks between the domains were remain. The electrochemical plating process has been discussed and high diffusion rate of oxygen which was produced spontaneously by the balancing reaction on the auxiliary electrode, was found to be responsible for the preservation of drying cracks. Oxygen free solutions made of either argon degassed copper sulfate solution and copper glycerol solution have shown crack filling features, which proved the oxygen diffusion controlled copper resolution hypothesis. The plating voltage went to more negative direction for the oxygen-involved bath than the argon-degassed solution because there was an additional voltage for the copper dissolution process. The dissolution rate increased with the current density and resulted in a larger voltage

difference between the oxygen involved and degassed solutions.

The smooth surface of the polystyrene films has been mirrored in the macroporous copper films. However, in the macroporous silver films, the porous structures were continuous at the bottom but stepped up to the top surface, giving the ´´domain´´ appearance. Such surface feature have been explained that the dense silver filled the drying cracks and the stress built up during the electrochemical growth could only be relieved upwards, resulting in steps. In contrast, drying cracks were preserved and stress could relax in isolated macroporous domains laterally.

6.1.4 Optical properties

The macroporous metallic films were opalescent and exhibited characteristic optical properties. The position of the angle-resolved reflectance peak was determined by the effective refractive index and void size that can be controlled by the choice of the diameter of the colloidal spheres. The stop band of the silver film was in shorter wavelength region than that of the copper due to the lower refractive index of silver. The films made of colloidal spheres of diameter of 248 nm and 327 nm showed stop bands in the visible wavelength range while those made of 651 nm have bands in the near-IR infrared. In addition, the study over film thickness has found that two dimensional monolayer macroporous thin films were not sufficient to display the stop band but bands of comparable width have been obtained from thin films over a couple of layer thick.

Additionally the void sizes of the macroporous copper and silver films were calculated by the peak wavelengths and corresponding incident angle. Void sizes of 336 nm and 333 nm were obtained for the thin films of copper and silver, respectively, obtained for the tempting sphere diameter of 344 nm, showing the shrinkage after

removal of the polystyrene films was less than 4 %, which confirms a dense growth by electrochemical plating.

6.1.5 SERS measurements

Preliminary SERS measurements on the macroporous metallic films used as active substrate have been taken on void size, dye concentration and film thickness effects on their performances. The largest void size of 651 nm showed the highest SERS intensity. The intensity of the SERS signals increased linear to the increasing of the dye concentration but it was not dependent on the thickness of the nanostructured films. However, the best ordered film showed that highest intensity and confirmed that periodicity is one of the main parameters that affecting the SERS performance. The results have confirmed the highly ordered porous silver nanostructure was desirable for Raman intensity enhancement. However further work are required to ensure its using as a stable and reproducible substrate.

6.2 Suggestions for future work

With regard to the direct formation of three-dimensional ordered macroporous metallic structures, there are many avenues open to progress this work both in terms of understanding their fundamental properties and exploiting their unique applications. Some of these areas are highlighted below.

Firstly, the electrochemical growth can be extended for metallic composites. For example, silver or gold are the most promising SERS substrates. However, if a substrate made from cheaper alternatives such as copper and then coated the surface with silver or gold, it would work the same in use but certainly at a much lower cost. The colloidal crystal will be initially penetrated by a metallic element e.g. Cu and then

the colloidal particles are chemically dissolved to expose the inner shell of the void to another electrolyte. Nucleation of the new metal e.g. Ag will take place on all of the conductive surfaces of the macroporous structure and the original metal will be coated with a thin layer of the new metal. Though the void size will become smaller, the periodicity and macroporous features will be preserved. However, the plating parameters have to be carefully chosen to make sure a uniform distribution of the nucleation and to avoid over-filling. This consecutive growth is one of the unique advantages of using the electrochemical plating.

Secondly, further investigation on SERS can be conducted for a wider range of moleculars. The concentration will be varied to obtain the minimum detection limit for each type of molecular. Here also requires further measurements on the thin films of tuned void size or film thickness to develop a better understanding of the enhancement arising from the localised plasmons and long-range periodicity. Since the key to the application of 3-DOM metallic structures as the SERS-active substrates is the reproducibility and stability of the thin films, measurements should be performed on the films grown at the same conditions including the void size, plating current and time, to monitor if the enhancement is reproducible.

Thirdly, computer modelling will be used to predict the properties and to find analytical solutions to problems in fabrication. Defects such as drying cracks, staking faults may reduce the performance of the 3-DOM metallic structures. The metallic structure have significant propagation losses, unless the fabrication precision and quality are of the highest possible standard [8]. Computer modelling may combine simulation with actual experiments. The properties of the Bragg diffraction will be primarily investigated and the dependence of its reflection on the geometrical parameters will be analysed. Experimental results for the stop-band behaviour of the

fabricated structures will then be given to validate the theoretical results. Model of either defect-free or induced-defects structures can be stimulated [15]. The modelling system is able to characterise any complex photonic structures instead of time-consuming or expensive fabrication and measurements of the trial-and-error steps.

Finally, high surface area and rigid metallic structure make the macroporous metals are ideal scaffolds. For example, a phase change material that use chemical bonds to store and release heat can be used for body, room and equipment thermal controlling applications. When the material reaches a certain temperature, it change phase (solid melts to liquid) and absorbs large amounts of heat without getting hotter; when the ambient temperature in the space around the material falls, it solidifies and releases its stored heat. However, the phase transform material is a wax and needs storage medium before any practical uses. The voids of the macroporous metals are uniform and interconnected by small windows that make the wax accessible to the entire internal surfaces. When they hosted the phase change material and used in the wall of thermal efficient housing, they will ensure a uniform loading of the phase transform material and thus ensures a uniform room temperature without the carbon emissions and costs associated with conventional air conditioning.

7 REFERENCES

1. Roychoudhuri C, Kracklauer AF, Creath K. The Nature of Light - What is a Photon? Boca Raton, FL: CRC Press, Taylor & Francis Group; 2008.

2. Joannopoulos JD, Johnson SG, Winn JN, Meade RD. Photonic Crystals - Modeling the Flow of Light. 2nd edition ed. New Jersey, USA: Princeton University Press; 2008.

3. Nojima S, Kamakura Y. *Journal of the Physical Society of Japan* 2008; **77:**(3), 034403.

4. Creighton JA, Blatchford CG, Albrecht MG. *Journal of the Chemical Society-Faraday Transactions Ii* 1979; **75:** 790-798.

5. Braun PV, Zehner RW, White CA, Weldon MK, Kloc C, Patel SS, Wiltzius P. *Europhysics Letters* 2001; **56:**(2), 207-213.

6. McLachlan MA. Synthesis and Characterisation of Thin Films Photonic Crystals. University of Glasgow: PhD thesis; 2005.

7. Pine DJ, Manoharan VN, Thorne J. *Abstracts of Papers of the American Chemical Society* 2001; **221:** U232.

8. Gnan M, Bellanca G, Chong H, Bassi P, Rue R. *Optical and Quantum Electronics* 2006; **38:**(1-3), 133-148.

9. Hirayama H, Hamano T, Aoyagi Y. *Applied Physics Letters* 1996; **69:**(6), 791-793.

10. Lee JH, Kim YS, Constant K, Ho KM. *Advanced Materials* 2007; **19:**(6), 791-794.

11. Lin SY, Fleming JG, Hetherington DL, Smith BK, Biswas R, Ho KM, Sigalas MM, Zubrzycki W, Kurtz SR, Bur J. *Nature* 1998; **394:**(6690), 251-253.

12. Temelkuran B, Ozbay E, Sigalas M, Tuttle G, Soukoulis CM, Ho KM. *Applied Physics A-Materials Science & Processing* 1998; **66:**(3), 363-365.

13. Katsarakis N, Chatzitheodoridis E, Kiriakidis G, Sigalas MM, Soukoulis CM, Leung WY, Tuttle G. *Applied Physics Letters* 1999; **74:**(22), 3263-3265.

14. McCalmont JS, Sigalas MM, Tuttle G, Ho KM, Soukolis CM. *Applied Physics Letters* 1996; **68:**(19), 2759-2761.

15. Giorgio A, Perri AG. *Journal of Computational Electronics* 2003; **2:** 397-401.

16. Lin SY, Chow E, Hietala V, Villeneuve PR, Joannopoulos JD. *Science* 1998; **282:**(5387), 274-276.

17. Mekis A, Chen JC, Kurland I, Fan SH, Villeneuve PR, Joannopoulos JD. *Physical*

Review Letters 1996; **77:**(18), 3787-3790.

18. Povinelli ML, Johnson SG, Lidorikis E, Joannopoulos JD, Soljacic M. *Applied Physics Letters* 2004; **84:**(18), 3639-3641.

19. Campbell M, Sharp DN, Harrison MT, Denning RG, Turberfield AJ. *Nature* 2000; **404:**(6773), 53-56.

20. Celio H, Barton E, Stevenson KJ. *Langmuir* 2006; **22:**(26), 11426-11435.

21. Ito T, Okazaki S. *Nature* 2000; **406:**(6799), 1027-1031.

22. Moon JH, Kim WS, Ha JW, Jang SG, Yang SM, Park JK. *Chemical Communications* 2005;(32), 4107-4109.

23. Ao XY, He SL. *Optics Letters* 2004; **29:**(21), 2542-2544.

24. Chincholi A. Parallel Fabrication of Photonic Crystals using Interference Lithography. University of Cincinnati: MSc thesis; 2005.

25. Divliansky I, Mayer TS, Holliday KS, Crespi VH. *Applied Physics Letters* 2003; **82:**(11), 1667-1669.

26. Divliansky IB, Shishido A, Khoo IC, Mayer TS, Pena D, Nishimura S, Keating CD, Mallouk TE. *Applied Physics Letters* 2001; **79:**(21), 3392-3394.

27. Jensen TR, Malinsky MD, Haynes CL, Van Duyne RP. *Journal of Physical Chemistry B* 2000; **104:**(45), 10549-10556.

28. Wang X, Xu JF, Su HM, Zeng ZH, Chen YL, Wang HZ, Pang YK, Tam WY. *Applied Physics Letters* 2003; **82:**(14), 2212-2214.

29. Ullal CK, Maldovan M, Thomas EL, Chen G, Han YJ, Yang S. *Applied Physics Letters* 2004; **84:**(26), 5434-5436.

30. Yang SM, Jang SG, Choi DG, Kim S, Yu HK. *Small* 2006; **2:**(4), 458-475.

31. Sumida T, Wada Y, Kitamura T, Yanagida S. *Chemical Communications* 2000;(17), 1613-1614.

32. Braun P, Wiltzius P. *Advanced Materials* 2001; **13:**(7), 482-485.

33. Luo G, Liu ZJ, Li L, Xie SH, Kong JL, Zhao DY. *Advanced Materials* 2001; **13:**(4), 286-289.

34. Bartlett PN, Birkin PR, Ghanem MA, Toh CS. *Journal of Materials Chemistry* 2001; **11:**(3), 849-853.

35. Sumida T, Wada Y, Kitamura T, Yanagida S. *Chemistry Letters* 2001;(1), 38-39.

36. Imhof A, Pine DJ. *Nature* 1997; **389:**(6654), 948-951.

37. Imhof A, Pine DJ. *Recent Advances in Catalytic Materials* 1998; **497:** 167-172.

38. Cai MM, Shen JH, Ji Z. *Rare Metal Materials and Engineering* 2003; **32:** 752-754.

39. Manoharan VN, Imhof A, Thorne JD, Pine DJ. *Micro- and Nano-Photonic Materials and Devices* 2000; **3937:** 44-50.

40. Barbetta A, Carnachan RJ, Smith KH, Zhao CT, Cameron NR, Kataky R, Hayman M, Przyborski SA, Swan M. *Macromolecular Symposia* 2005; **226:** 203-211.

41. Yan HW, Blanford CF, Smyrl WH, Stein A. *Chemical Communications* 2000;(16), 1477-1478.

42. Tessier P, Velev OD, Kalambur AT, Lenhoff AM, Rabolt JF, Kaler EW. *Advanced Materials* 2001; **13:**(6), 396-400.

43. Lei ZB, Li JM, Ke YX, Zhang YG, Zhang HC, Li FQ, Xing JY. *Journal of Materials Chemistry* 2001; **11:**(12), 2930-2933.

44. Wang DY, Caruso F. *Advanced Materials* 2003; **15:**(3), 205-+.

45. Yeo SH, Teh LK, Wong CC. *Journal of Porous Materials* 2006; **13:**(3-4), 281-285.

46. Miguez H, Meseguer F, Lopez C, Mifsud A, Moya JS, Vazquez L. *Langmuir* 1997; **13:**(23), 6009-6011.

47. Kim JC, Kim YN, Hur NH, Kim WS, Kang YG. *Physica Status Solidi B-Basic Research* 2004; **241:**(7), 1585-1588.

48. Galisteo JF, Garcia-Santamaria F, Golmayo D, Juarez BH, Lopez C, Palacios E. *Journal of Optics A-Pure and Applied Optics* 2005; **7:**(2), S244-S254.

49. Stein A, Schroden RC. *Current Opinion in Solid State & Materials Science* 2001; **5:**(6), 553-564.

50. Braun PV, Wiltzius P. *Nature* 1999; **402:**(6762), 603-604.

51. Busch K, John S. *Physical Review e* 1998; **58:**(3), 3896-3908.

52. Biswas R, Sigalas MM, SubRamania G, Ho KM. *Physical Review B* 1998; **57:**(7), 3701-3705.

53. Biswas R, Sigalas MM, SubRamania G, Soukoulis CM, Ho KM. *Physical Review B* 2000; **61:**(7), 4549-4553.

54. Lanata M, Cherchi M, Zappettini A, Pietralunga SM, Martinelli M. *Optical Materials* 2001; **17:**(1-2), 11-14.

55. Fleming JG, Lin SY, El-Kady I, Biswas R, Ho KM. *Nature* 2002; **417:**(6884), 52-55.

56. Noda S, Tomoda K, Yamamoto N, Chutinan A. *Science* 2000; **289:**(5479), 604-606.

57. McIntosh KA, Mahoney LJ, Molvar KM, Mcmahon OB, Verghese S, Rothschild M, Brown ER. *Applied Physics Letters* 1997; **70:**(22), 2937-2939.

58. Straub M, Ventura M, Gu M. *Physical Review Letters* 2003; **91:**(4).

59. Ozin GA, Yang SM. *Advanced Functional Materials* 2001; **11:**(2), 95-104.

60. Blanco A, Chomski E, Grabtchak S, Ibisate M, John S, Leonard SW, Lopez C, Meseguer F, Miguez H, Mondia JP, Ozin GA, Toader O, van Driel HM. *Nature* 2000; **405:**(6785), 437-440.

61. Vlasov YA, Bo XZ, Sturm JC, Norris DJ. *Nature* 2001; **414:**(6861), 289-293.

62. Weaver JH, Frederikse HPR. Optical Properties of Selected Elements - CRC Handbook of Chemistry and Physics. 87th Edition ed. http://www.hbcpnetbase.com/: Internet version; 2006.

63. Moroz A. *Physical Review Letters* 1999; **83:**(25), 5274-5277.

64. Moroz A. *Europhysics Letters* 2000; **50:**(4), 466-472.

65. Zhang WY, Lei XY, Wang ZL, Zheng DG, Tam WY, Chan CT, Sheng P. *Physical Review Letters* 2000; **84:**(13), 2853-2856.

66. Mahajan S, Baumberg JJ, Russell AE, Bartlett PN. *Physical Chemistry Chemical Physics* 2007; **9:**(45), 6016-6020.

67. Tessier PM, Velev OD, Kalambur AT, Rabolt JF, Lenhoff AM, Kaler EW. *Journal of the American Chemical Society* 2000; **122:**(39), 9554-9555.

68. Tessier PM, Christesen SD, Ong KK, Clemente EM, Lenhoff AM, Kaler EW, Velev OD. *Applied Spectroscopy* 2002; **56:**(12), 1524-1530.

69. Xu LB, Zhou WLL, Frommen C, Baughman RH, Zakhidov AA, Malkinski L, Wang JQ, Wiley JB. *Chemical Communications* 2000;(12), 997-998.

70. Bartlett PN, Baumberg JJ, Birkin PR, Ghanem MA, Netti MC. *Chemistry of Materials* 2002; **14:**(5), 2199-2208.

71. Wijnhoven JEGJ, Zevenhuizen SJM, Hendriks MA, Vanmaekelbergh D, Kelly JJ, Vos WL. *Advanced Materials* 2000; **12:**(12), 888-890.

72. Abdelsalam ME, Bartlett PN, Baumberg JJ, Cintra S, Kelf TA, Russell AE. *Electrochemistry Communications* 2005; **7:**(7), 740-744.

73. Bartlett PN, Baumberg JJ, Coyle S, Abdelsalam ME. *Faraday Discussions* 2004; **125:** 117-132.

74. Sun FQ, Cai WP, Li Y, Cao BQ, Lu F, Duan GT, Zhang LD. *Advanced Materials* 2004; **16:**(13), 1116-1121.

75. Strutt JW. *Philosophical Magazine* 1887; **24:** 145-159.

76. Kuzmiak V, Maradudin AA. *Physical Review B* 1997; **55:**(12), 7427-7444.

77. Tanaka K, Nakamura T, Takamatsu W, Yamanishi M, Lee Y, Ishihara T. *Physical Review Letters* 1995; **74:**(17), 3380-3383.

78. Zou SL, Schatz GC. *Journal of Chemical Physics* 2004; **121:**(24), 12606-12612.

79. Kogelnik H, Shank CV. *Applied Physics Letters* 1971; **18:**(4), 152-154.

80. Yablonovitch E, Gmitter TJ, Leung KM. *Physical Review Letters* 1991; **67:**(17), 2295-2298.

81. Yablonovitch E, Gmitter TJ. *Journal of the Optical Society of America A-Optics Image Science and Vision* 1990; **7:**(9), 1792-1800.

82. Yablonovitch E. *Physical Review Letters* 1987; **58:**(20), 2059-2062.

83. Yablonovitch E. *Journal of the Optical Society of America B-Optical Physics* 1993; **10:**(2), 283-295.

84. Yablonovitch E. *Journal of Physics-Condensed Matter* 1993; **5:**(16), 2443-2460.

85. Yablonovitch E. *Scientific American* 2001; **285:**(6), 46-55.

86. John S. *Physical Review Letters* 1984; **53:**(22), 2169-2172.

87. John S. *Physical Review Letters* 1987; **58:**(23), 2486-2489.

88. John S, Quang T. *Physical Review A* 1994; **50:**(2), 1764-1769.

89. John S, Florescu M. *Journal of Optics A-Pure and Applied Optics* 2001; **3:**(6), S103-S120.

90. Wang ZL, Chan CT, Zhang WY, Ming NB, Sheng P. *Physical Review B* 2001; **64:**(11), 113108.

91. Chan CY, Xu JB, Waye MY, Ong HC. *Applied Physics Letters* 2010; **96:** 033104-1-033104-3.

92. Dimitrov AS, Nagayama K. *Langmuir* 1996; **12:**(5), 1303-1311.

93. Fleury V, Barkey D. *Europhysics Letters* 1996; **36:**(4), 253-258.

94. Helseth LE, Wen HZ, Hansen RW, Johansen TH, Heinig P, Fischer TM. *Langmuir* 2004; **20:**(17), 7323-7332.

95. Jiang P. *Angewandte Chemie-International Edition* 2004; **43:**(42), 5625-5628.

96. Ho KM, Chan CT, Soukoulis CM. *Physical Review Letters* 1990; **65:**(25), 3152-3155.

97. Vlasov YA, Astratov VN, Karimov OZ, Kaplyanskii AA, Bogomolov VN, Prokofiev AV. *Physical Review B* 1997; **55:**(20), 13357-13360.

98. Cassagne D, Jouanin C, Bertho D. *Physical Review B* 1996; **53:**(11), 7134-7142.

99. Haus JW, Sozuer HS, Inguva R. *Journal of Modern Optics* 1992; **39:**(10), 1991-2005.

100. Yannopapas V, Stefanou N, Modinos A. *Journal of Physics-Condensed Matter* 1997; **9:**(46), 10261-10270.

101. Tarhan II, Watson GH. *Physical Review B* 1996; **54:**(11), 7593-7597.

102. Tarhan II, Watson GH. *Physical Review Letters* 1996; **76:**(2), 315-318.

103. Moroz A, Sommers C. *Journal of Physics-Condensed Matter* 1999; **11:**(4), 997-1008.

104. Kokalj A. *Computational Materials Science* 2003; **28:**(2), 155-168.

105. Yu X, Lee Y-J, Furstenberg R, White JO, Braun PV. *Advanced Materials* 2007; **19:** 1689-1692.

106. Kuai SL, Bader G, Hache A, Truong VV, Hu XF. *Thin Solid Films* 2005; **483:**(1-2), 136-139.

107. Smith WE, Dent G. Modern Raman Spectroscopy - A Practical Approach. England: John Wiley & Sons, Ltd; 2005.

108. Ferraro JR, Nakamoto K, Brown CW. Introductory Raman Spectroscopy. 2nd edition ed. London: Academic Press; 2003.

109. Gardiner DJ. Practical Raman spectroscopy. London: Springer-Verlag; 1989.

110. Fleischm M, Hendra PJ, Mcquilla AJ. *Chemical Physics Letters* 1974; **26:**(2), 163-166.

111. Jeanmaire DL, Vanduyne RP. *Journal of Electroanalytical Chemistry* 1977; **84:**(1), 1-20.

112. Albrecht MG, Creighton JA. *Journal of the American Chemical Society* 1977; **99:**(15), 5215-5217.

113. Brown RJC, Wang J, Tantra R, Yardley RE, Milton MJT. *Faraday Discussions* 2006; **132:** 201-213.

114. Cunningham D, Littleford RE, Smith WE, Lundahl PJ, Khan I, Mccomb DW, Graham D, Laforest N. *Faraday Discussions* 2006; **132:** 135-145.

115. Kneipp K, Kneipp H, Itzkan I, Dasari RR, Feld MS. *Journal of Physics-Condensed Matter* 2002; **14:**(18), R597-R624.

116. Moskovits M. *Journal of Raman Spectroscopy* 2005; **36:**(6-7), 485-496.

117. Le Ru EC, Etchegoin PG. *Faraday Discussions* 2006; **132:** 63-75.

118. Michaels AM, Nirmal M, Brus LE. *Journal of the American Chemical Society* 1999; **121:**(43), 9932-9939.

119. Kerker M, Siiman O, Bumm LA, Wang DS. *Applied Optics* 1980; **19:**(19), 3253-3255.

120. Jarvis RM, Brooker A, Goodacre R. *Faraday Discussions* 2006; **132:** 281-292.

121. Kuncicky DM, Christesen SD, Velev OD. *Applied Spectroscopy* 2005; **59:**(4), 401-409.

122. Otto A, Mrozek I, Grabhorn H, Akemann W. *Journal of Physics-Condensed Matter* 1992; **4:** 1143-1212.

123. Weaver GC, Norrod K. *Journal of Chemical Education* 1998; **75:**(5), 621-624.

124. Roy D, Wang J, Welland ME. *Faraday Discussions* 2006; **132:** 215-225.

125. Sawai Y, Takimoto B, Nabika H, Ajito K, Murakoshi K. *Faraday Discussions* 2006; **132:** 179-190.

126. Tian ZQ, Ren B, Wu DY. *Journal of Physical Chemistry B* 2002; **106:**(37), 9463-9483.

127. Tian ZQ, Yang ZL, Ren B, Li JF, Zhang Y, Lin XF, Hu JW, Wu DY. *Faraday Discussions* 2006; **132:** 159-170.

128. Abdelsalam ME, Mahajan S, Bartlett PN, Baumberg JJ, Russell AE. *Journal of the American Chemical Society* 7 A.D.; **129:** 7399-7406.

129. Itoh T, Maeda T, Kasuya A. *Faraday Discussions* 2006; **132:** 95-109.

130. Abe H, Manzel K, Schulze W, Moskovits M, Dilella DP. *Journal of Chemical Physics* 1981; **74:**(2), 792-797.

131. Mrozek I, Otto A. *Applied Physics A-Materials Science & Processing* 1989; **49:** 389-391.

132. Chaney SB, Shanmukh S, Dluhy RA, Zhao Y-P. *Applied Physics Letters* 2005; **87:** 031908.

133. Kahl M, Voges E, Kostrewa S, Viets C, Hill W. *Sensors and Actuators B-Chemical* 1998; **51:**(1-3), 285-291.

134. Li HG, Baum CE, Sun J, Cullum BM. *Applied Spectroscopy* 2006; **60:**(12), 1377-1385.

135. Perney NMB, Baumberg JJ, Zoorob ME, Charlton MDB, Mahnkopf S, Netti CM. *Optics Express* 2006; **14:**(2), 847-857.

136. Girlando A, Philpott MR, Heitmann D, Swalen JD, Santo R. *Journal of Chemical Physics* 1980; **72:**(9), 5187-5191.

137. Dieringer JA, McFarland AD, Shah NC, Stuart DA, Whitney AV, Yonzon CR, Young MA, Zhang XY, Van Duyne RP. *Faraday Discussions* 2006; **132:** 9-26.

138. Sanda PN, Warlaumont JM, Demuth JE, Tsang JC, Christmann K, Bradley JA. *Physical Review Letters* 1980; **45:**(18), 1519-1523.

139. Smith WE. *Chemical Society Reviews* 2008; **37:**(5), 955-964.

140. Baia M, Baia L, Astilean S. *Chemical Physics Letters* 2005; **404:**(1-3), 3-8.

141. Murray CA, Allara DL. *Journal of Chemical Physics* 1982; **76:**(3), 1290-1303.

142. Murray CA, Allara DL, Rhinewine M. *Physical Review Letters* 1981; **46:**(1), 57-60.

143. Lee PC, Meisel D. *Journal of Physical Chemistry* 1982; **86:**(17), 3391-3395.

144. Leopold N, Lendl B. *Journal of Physical Chemistry B* 2003; **107:**(24), 5723-5727.

145. Manzel K, Schulze W, Moskovits M. *Chemical Physics Letters* 1982; **85:**(2), 183-186.

146. Emory SR, Jensen RA, Wenda T, Han MY, Nie SM. *Faraday Discussions* 2006; **132:** 249-259.

147. Green M, Liu FM, Cohen L, Kollensperger P, Cass T. *Faraday Discussions* 2006; **132:** 269-280.

148. Kneipp K, Kneipp H. *Faraday Discussions* 2006; **132:** 27-33.

149. Maher RC, Cohen LF, Le Ru EC, Etchegoin PG. *Faraday Discussions* 2006; **132:** 77-83.

150. Svedberg F, Kall M. *Faraday Discussions* 2006; **132:** 35-44.

151. Futamata M. *Faraday Discussions* 2006; **132:** 45-61.

152. Mahajan S, Abdelsalam M, Suguwara Y, Cintra S, Russell A, Baumberg J, Bartlett P. *Physical Chemistry Chemical Physics* 2007; **9:**(1), 104-109.

153. Baumberg JJ, Kelf TA, Sugawara Y, Cintra S, Abdelsalam ME, Bartlett PN, Russell AE. *Nano Letters* 2005; **5:**(11), 2262-2267.

154. Banholzer MJ, Millstone JE, Qin LD, Mirkin CA. *Chemical Society Reviews* 2008; **37:**(5), 885-897.

155. Wu DY, Li JF, Ren B, Tian ZQ. *Chemical Society Reviews* 2008; **37:**(5), 1025-1041.

156. Kuncicky DM, Prevo BG, Velev OD. *Journal of Materials Chemistry* 2006; **16:**(13), 1207-1211.

157. Cintra S, Abdelsalam ME, Bartlett PN, Baumberg JJ, Kelf TA, Sugawara Y, Russell AE. *Faraday Discussions* 2006; **132:** 191-199.

158. Kelf TA, Sugawara Y, Cole RM, Baumberg JJ, Abdelsalam ME, Cintra S, Mahajan S, Russell AE, Bartlett PN. *Physical Review B* 2006; **74:**(24), 245415-1-245415-12.

159. Netti MC, Coyle S, Baumberg JJ, Ghanem MA, Birkin PR, Bartlett PN, Whittaker DM. *Advanced Materials* 2001; **13:**(18), 1368-1370.

160. Gaponenko SV. *Physical Review B* 2002; **65:**(14), 140303-1-140303-4.

161. Gaponenko SV. *Saratov Fall Meeting 2001: Coherent Optics of Ordered and Random Media Ii* 2002; **4705:** 83-87.

162. Allard M, Sargent EH, Kumacheva E, Kalinina O. *Optical and Quantum Electronics* 2002; **34:**(1-3), 27-36.

163. Lellig C, Hartl W, Wagner J, Hempelmann R. *Angewandte Chemie-International Edition* 2002; **41:**(1), 102-104.

164. Chan CH, Chen CC, Huang CK, Weng WH, Wei HS, Chen H, Lin HT, Chang HS, Chen WY, Chang WH, Hsu TM. *Nanotechnology* 2005; **16:**(9), 1440-1444.

165. Mei DB, Liu HG, Cheng BY, Li ZL, Zhang DZ, Dong P. *Physical Review B* 1998; **58:**(1), 35-38.

166. Trau M, Saville DA, Aksay IA. *Langmuir* 1997; **13:**(24), 6375-6381.

167. Meseguer F. *Colloids and Surfaces A* 2005; **270:** 1-7.

168. Vesaratchanon JS, Nikolov A, Wasan DT. *Journal of Colloid and Interface Science* 2008; **322:**(1), 180-189.

169. Vesaratchanon S, Nikolov A, Wasan DT. *Advances in Colloid and Interface Science* 2007; **134-35:** 268-278.

170. Hoogenboom JP, Derks D, Vergeer P, van Blaaderen A. *Journal of Chemical Physics* 2002; **117:**(24), 11320-11328.

171. Mayoral R, Requena J, Moya JS, Lopez C, Cintas A, Miguez H, Meseguer F, Vazquez L, Holgado M, Blanco A. *Advanced Materials* 1997; **9:**(3), 257-260.

172. Salvarezza RC, Vazquez L, Miguez H, Mayoral R, Lopez C, Meseguer F. *Physical Review Letters* 1996; **77:**(22), 4572-4575.

173. Bresson F, Chen CC, Chi GC, Chen YW. *Applied Surface Science* 2003; **217:**(1-4), 281-288.

174. Lin KH, Crocker JC, Prasad V, Schofield A, Weitz DA, Lubensky TC, Yodh AG. *Physical Review Letters* 2000; **85:**(8), 1770-1773.

175. Holgado M, Garcia-Santamaria F, Blanco A, Ibisate M, Cintas A, Miguez H, Serna CJ, Molpeceres C, Requena J, Mifsud A, Meseguer F, Lopez C. *Langmuir* 1999; **15:**(14), 4701-4704.

176. Rogach AL, Kotov NA, Koktysh DS, Ostrander JW, Ragoisha GA. *Chemistry of Materials* 2000; **12:**(9), 2721-2726.

177. Park SH, Xia YN. *Advanced Materials* 1998; **10:**(13), 1045-1048.

178. Clark NA, Hurd AJ, Ackerson BJ. *Nature* 1979; **281:**(5726), 57-60.

179. Okubo T. *Langmuir* 1994; **10:**(6), 1695-1702.

180. Velev OD, Lenhoff AM, Kaler EW. *Science* 2000; **287:**(5461), 2240-2243.

181. Haynes CL, Van Duyne RP. *Journal of Physical Chemistry B* 2001; **105:**(24), 5599-5611.

182. Wang DY, Mohwald H. *Advanced Materials* 2004; **16:**(3), 244-247.

183. Rehg TJ, Higgins BG. *Aiche Journal* 1992; **38:**(4), 489-501.

184. Zhou ZC, Zhao XS. *Langmuir* 2005; **21:**(10), 4717-4723.

185. Goldenberg LM, Wagner J, Stumpe J, Paulke BR, Gornitz E. *Materials Science & Engineering C-Biomimetic and Supramolecular Systems* 2002; **22:**(2), 405-408.

186. Jiang P, Bertone JF, Hwang KS, Colvin VL. *Chemistry of Materials* 1999; **11:**(8),

2132-2140.

187. Brinker CJ, Lu YF, Sellinger A, Fan HY. *Advanced Materials* 1999; **11:**(7), 579-585.

188. Vos WL, Megens M, vanKats CM, Bosecke P. *Langmuir* 1997; **13:**(23), 6004-6008.

189. Holland BT, Blanford CF, Do T, Stein A. *Chemistry of Materials* 1999; **11:**(3), 795-805.

190. Ye YH, Badilescu S, Truong VV, Rochon P, Natansohn A. *Applied Physics Letters* 2001; **79:**(6), 872-874.

191. Dziomkina NV, Vancso GJ. *Soft Matter* 2005; **1:**(4), 265-279.

192. Yang PD, Deng T, Zhao DY, Feng PY, Pine D, Chmelka BF, Whitesides GM, Stucky GD. *Science* 1998; **282:**(5397), 2244-2246.

193. Abdelsalam ME, Bartlett PN, Baumberg JJ, Coyle S. *Advanced Materials* 2004; **16:**(1), 90-93.

194. Petrov AS, Talbot JB. *Journal of the Electrochemical Society* 2009; **156:**(3), D92-D97.

195. Lei ZB, Zhang YG, Wang H, Ke YX, Li JM, Li FQ, Xing JY. *Journal of Materials Chemistry* 2001; **11:**(8), 1975-1977.

196. Wijnhoven JEGJ, Vos WL. *Science* 1998; **281:**(5378), 802-804.

197. Bartlett PN, Birkin PR, Ghanem MA. *Chemical Communications* 2000; **2000:**(17), 1671-1672.

198. Sumida T, Wada Y, Kitamura T, Yanagida S. *Langmuir* 2002; **18:**(10), 3886-3894.

199. Chung YW, Leu IC, Lee JH, Yen JH, Hon MH. *Journal of the Electrochemical Society* 2007; **154:**(6), E77-E83.

200. Srivastava AK, Madhavi S, White TJ, Ramanujan RV. *Journal of Materials Chemistry* 2005; **15:**(41), 4424-4428.

201. Juarez BH, Lopez C, Alonso C. *Journal of Physical Chemistry B* 2004; **108:**(43), 16708-16712.

202. Bartlett PN, Ghanem MA, El Hallag IS, de Groot P, Zhukov A. *Journal of Materials Chemistry* 2003; **13:**(10), 2596-2602.

203. Liu F, Yan QF, Zhou WJ, Zhao XS, Lee JY. *Chemistry of Materials* 2006; **18:**(18), 4328-4335.

204. Li X, Tao FF, Jiang Y, Xu Z. *Journal of Colloid and Interface Science* 2007; **308:**(2), 460-465.

205. Kulinowski KM, Jiang P, Vaswani H, Colvin VL. *Advanced Materials* 2000; **12:**(11), 833-838.

206. Yan HW, Blanford CF, Holland BT, Smyrl WH, Stein A. *Chemistry of Materials* 2000; **12:**(4), 1134-1141.

207. Velev OD, Tessier PM, Lenhoff AM, Kaler EW. *Nature* 1999; **401:**(6753), 548.

208. Meyer J. *Materialwissenschaft und Werkstofftechnik* 2008; **39:**(12), 958-962.

209. Jiang SQ, Kan CW, Yuen CWM, Wong WK. *Journal of Applied Polymer Science* 2008; **108:**(4), 2630-2637.

210. Wu XC, Bittner AM, Kern K. *Langmuir* 2002; **18:**(12), 4984-4988.

211. Kohn A, Eizenberg M, Shacham-Diamand Y. *Journal of Applied Physics* 2002; **92:**(9), 5508-5511.

212. Kuhn A, Argoul F. *Journal of Electroanalytical Chemistry* 1995; **397:**(1-2), 93-104.

213. Nahrstedt B, Glesne T, McNally J, Kenemuth J, Magrath B. *Applied Optics* 1996; **35:**(19), 3680-3686.

214. Jiang P, Cizeron J, Bertone JF, Colvin VL. *Journal of the American Chemical Society* 1999; **121:**(34), 7957-7958.

215. Brankovic SR, McBreen J, Adzic RR. *Journal of Electroanalytical Chemistry* 2001; **503:**(1-2), 99-104.

216. Sasaki K, Wang JX, BalasubRamanian M, McBreen J, Uribe F, Adzic RR. *Electrochimica Acta* 2004; **49:**(22-23), 3873-3877.

217. Watt IM. The Principles and Practice of Electron Microscopy. 2nd Edition ed. Cambridge University Press; 1997.

218. McQuarrie DA, Simon JD. Physical Chemistry: A Molecular Approach. University Science Books; 1997.

219. Seiler H. *Journal of Applied Physics* 1983; **54:**(11), R1-R18.

220. Copeland PL. *Physical Review* 1940; **58:**(7), 604-607.

221. Comoretto D, Grassi R, Marabelli F, Andreani LC. *Materials Science & Engineering C-Biomimetic and Supramolecular Systems* 2003; **23:**(1-2), 61-65.

222. Miguez H, Blanco A, Meseguer F, Lopez C, Yates HM, Pemble ME, Fornes V, Mifsud A. *Physical Review B* 1999; **59:**(3), 1563-1566.

223. Mangaiyarkarasi D, Breese MBH, Sheng OY, Ansari K, Vijila C, Blackwood D. Porous silicon based Bragg reflectors and Fabry-Perot interference filters for photonic applications. 2006. 61250X.

224. Cheng BY, Ni PG, Jin CJ, Li ZL, Zhang DZ, Dong P, Guo XC. *Optics Communications* 1999; **170:**(1-3), 41-46.

225. Ni PG, Dong P, Cheng BY, Li XY, Zhang DZ. *Advanced Materials* 2001; **13:**(6), 437-441.

226. Harkins WD. *Journal of the American Chemical Society* 1947; **69:**(6), 1428-1447.

227. Madaeni SS, Ghanbarian M. *Polymer International* 2000; **49:**(11), 1356-1364.

228. Munro D, Goodall AR, Wilkinson MC, Randle K, Hearn J. *Journal of Colloid and Interface Science* 1979; **68:**(1), 1-13.

229. Reese CE, Asher SA. *Journal of Colloid and Interface Science* 2002; **248:**(1), 41-46.

230. Barron C. Synthesis and Properties of Macroporous Thin Films - Towards Multifunctional Photonic Crystals. Imperial College London: PhD thesis; 2006.

231. Dubrovinsky LS. *Science* 1997; **278:**(5342), 1474-1475.

232. Woodcock LV. *Nature* 1997; **385:**(6612), 141-143.

233. Ye YH, LeBlanc F, Hache A, Truong VV. *Applied Physics Letters* 2001; **78:**(1), 52-54.

234. Gu ZZ, Fujishima A, Sato O. *Chemistry of Materials* 2002; **14:**(2), 760-765.

235. Kuai SL, Hu XF, Hache A, Truong VV. *Journal of Crystal Growth* 2004; **267:**(1-2), 317-324.

236. Odom TW. Introduction to Nanofabrication. 5 A.D.

237. McLachlan MA, Johnson NP, De la Rue RM, Mccomb DW. *Journal of Materials Chemistry* 2004; **14:**(2), 144-150.

238. Huibers PDT, Shah DO. *Langmuir* 1997; **13:**(22), 5995-5998.

239. Vereecken PM, Binstead RA, Deligianni H, Andricacos PC. *Ibm Journal of Research and Development* 2005; **49:**(1), 3-18.

240. Reid J. *Japanese Journal of Applied Physics Part 1-Regular Papers Short Notes & Review Papers* 2001; **40:**(4B), 2650-2657.

241. Wang T, Lindquist P, Erdemli S, Basol EC, Zhang R, Uzoh CE, Basol BM. *Thin Solid Films* 2005; **478:**(1-2), 345-351.

242. Jovic VD, Jovic GM. *Journal of the Serbian Chemical Society* 2001; **66:**(11-12), 935-952.

243. Chassaing E, Wiart R. *Electrochimica Acta* 1984; **29:**(5), 649-660.

244. Soares DM, Wasle S, Weil KG, Doblhofer K. *Journal of Electroanalytical Chemistry* 2002; **532:**(1-2), 353-358.

245. Ramos A, Miranda-Hernandez M, Gonzalez I. *Journal of the Electrochemical Society* 2001; **148:**(4), C315-C321.

246. Harraz FA, Kamada K, Sasano J, Izuo S, Sakka T, Ogata YH. *Physica Status Solidi A-Applications and Materials Science* 2005; **202:**(8), 1683-1687.

247. Bek RY, Shuraeva L, Ovchinnikova SN. *Russian Journal of Electrochemistry*

2004; **40:**(10), 1079-1083.

248. Saitou M. *Journal of the Electrochemical Society* 2005; **152:**(3), C113-C115.

249. Sanchez H, Chainet E, Nguyen B, Ozil P, Meas Y. *Journal of the Electrochemical Society* 1996; **143:**(9), 2799-2804.

250. Leidheis H, Ghuman ARP. *Journal of the Electrochemical Society* 1973; **120:**(4), 484-487.

251. Alsmeyer YW, Mccreery RL. *Analytical Chemistry* 1991; **63:**(13), 1289-1295.

252. Dean JA. Lange's Handbook of Chemistry (15th Edition). McGraw-Hill Inc.; 1999.

253. Friedt JM, Choi KH, Frederix F, Campitelli A. *Journal of the Electrochemical Society* 2003; **150:**(10), H229-H234.

254. Zeiri L, Younes O, Efrima S, Deutsch M. *Physical Review Letters* 1997; **79:**(23), 4685-4688.

255. Zarkadas GM, Stergiou A, Papanastasiou G. *Journal of Applied Electrochemistry* 2004; **34:**(6), 607-615.

256. Kim JY, Yu J, Lee JH, Lee TY. *Journal of Electronic Materials* 2004; **33:**(12), 1459-1464.

257. Esplandiu MJ, Hagenstrom H, Kolb DM. *Langmuir* 2001; **17:**(3), 828-838.

258. Vandeputte S, Hubin A, Vereecken J. *Electrochimica Acta* 1997; **42:**(23-24), 3429-3441.

259. Gonnissen D, Hubin A, Vereecken J. *Electrochimica Acta* 1999; **44:**(24), 4129-4137.

260. Pollet B, Lorimer JP, Hihn JY, Touyeras F, Mason TJ, Walton D. *Ultrasonics Sonochemistry* 2005; **12:**(1-2), 7-11.

261. Snveeraraghavan S, Krishnan RM, Natarajan SR. *Metal Finishing* 1989; 115-117.

262. Pauwels L, Simons W, Hubin A, Schoukens J, Pintelon R. *Electrochimica Acta* 2002; **47:**(13-14), 2135-2141.

263. Foster DG, Shapir Y, Jorne J. *Journal of the Electrochemical Society* 2003; **150:**(6), C375-C380.

264. Galvani CM, Graydon A, Riley DJ, York D. *Journal of Physical Chemistry C* 2007; **111:**(9), 3669-3674.

265. Koyano H, Kato M, Takenouchi H. *Journal of the Electrochemical Society* 1992; **139:**(11), 3112-3116.

266. Segeth W, Andreasen H, Boerma DO, Niesen L. *Hyperfine Interactions* 1986; **29:** 1271-1274.

267. Bao XH, Deng JF, Zhai RS, Wang DZ, Guo XX. *Catalysis Letters* 1990; **4:**(1), 25-36.

268. Holland BT, Blanford CF, Stein A. *Science* 1998; **281:**(5376), 538-540.

269. Jensen L, Schatz GC. *The Journal of Physical Chemistry Letters A* 2006; **110:**(18), 5973-5977.

270. Liu Y-C, Yang K-H, Hsu T-C. *Journal of Raman Spectroscopy* 2009; **40:** 903-907.

271. Shim S, Stuart CM, Mathies RA. *Journal of Chemical Physics Communications* 2008; **9:** 697-699.

272. Cao PG, Yao JL, Zheng JW, Gu RA, Tian ZQ. *Langmuir* 2002; **18:**(1), 100-104.

273. Metikos-Hukovie M, Furic K, Babic R, Marinovic A. *Surface and interface analysis* 1999; **27:** 1016-1025.

274. Gonnissen D, Langenaeker W, Hubin A, Geerlings P. *Journal of Raman Spectroscopy* 1998; **29:**(12), 1031-1039.

275. Berciaud S, Cognet L, Tamarat P, Lounis B. *Nano Letters* 2005; **5:**(3), 515-518.

276. Lei ZB, Li JM, Ke YX, Zhang YG, Wang H, He GF. *Journal of Materials Chemistry* 2001; **11:**(7), 1778-1780.